# Study on the Feasibility of Geosynchronous Satellites for Synthetic Aperture Radar Applications

Master MERIT Thesis
by
Josep Ruiz Rodon



**Universitat Politècnica de Catalunya**

European Master of Research on Information and Communication Technologies

Advisor: Antoni Broquetas Ibars

# ACKNOWLEDGMENTS

This thesis corresponds to the final project of the *European Master of Research on Information and Communication Technologies (MERIT)* given by the *Signal Theory and Communications* (TSC) department of the *Universitat Politècnica de Catalunya* (UPC). This document gathers the technical concepts acquired during the last years in the University in the field of remote sensing techniques. The project would not have been possible without the academic and moral support of a large number of people.

First of all, I would like to express my gratitude to my advisor Toni Broquetas to encourage me to start the Ph.D after an interesting final year project on SAR advanced techniques working jointly with EADS-CASA Espacio. After two years working together, his support has been really helpful to get through the difficulties of the project and to keep up the motivation of the first day in my work. I also want to thank to the other Ph.D students of TSC for their support and help in some parts of this thesis.

Thanks to my family for all the support during the years of degree and with this new Ph.D challenge. Special mention for all those colleagues that I met in Barcelona and also all the lifelong friends from Valls whose friendliness has been really helpful to switch off from the difficult moments in the thesis realization.

Finally, my sincere thanks to Andre Monti-Guarnieri and the people from Politecnico di Milano for giving me the opportunity to participate in the GeoSAR challenge. I appreciate all their experience provided in this project.

# TABLE OF CONTENTS

# LIST OF FIGURES

# LIST OF TABLES

# LIST OF SYMBOLS

| | |
|---|---|
| $T_0$ | Ambient temperature (290 $K$) |
| $\theta_{az}$ | Antenna azimuth beamwidth |
| $X_{az}$ | Antenna azimuth footprint width |
| $A_{eff}$ | Antenna effective area |
| $\theta_r$ | Antenna elevation beamwidth |
| $G_{2w}$ | Antenna gain 2-way |
| $G_r$ | Antenna gain in reception |
| $G_t$ | Antenna gain in transmission |
| $A_{geo}$ | Antenna geometric area |
| $\eta_{eff}$ | Antenna illumination efficiency |
| $L_a$ | Antenna length |
| $W$ | Antenna width |
| $\omega$ | Argument of the perigee |
| $\rho_{az}$ | Azimuth resolution |
| $\sigma_0$ | Backscattering coefficient |
| $k$ | Boltzmann constant ($1.38 \cdot 10^{-23}\, J/K$) |
| $f_{DC}$ | Central Doppler frequency |
| $\Delta\tau$ | Compressed pulse duration |
| $\delta(.)$ | Dirac's delta function |
| $f_d$ | Doppler frequency |
| $\Omega_E$ | Earth angular velocity |
| $M_E$ | Earth Mass ($M_E = 5.974 \cdot 10^{24}\, Kg$) |
| $\mu$ | Earth's gravitational constant |
| $E$ | Eccentric anomaly of the orbit |
| $E$ | Electric field |
| $\theta_{el}$ | Elevation angle |
| $Frac(.)$ | Fractional part of its argument |
| $\varphi_c$ | Geocentric latitude |
| $G$ | Gravitational constant ($G = 6.67 \cdot 10^{-11} m^3 Kg^{-1} s^{-2}$) |
| $\rho_{gr}$ | Ground range resolution |
| $\rho_{gr}$ | Ground range resolution |

| | |
|---|---|
| $S$ | Ground swath width |
| $\tau_{RP}$ | Guard time after and before pulse transmission |
| $\theta_{in}$ | Incidence angle |
| $Int(.)$ | Integer part of its argument |
| $T_i$ | Integration time |
| $\varphi_{SL}$ | Latitude of the satellite |
| $c$ | Light speed |
| $\Gamma_L$ | Load reflexion coefficient |
| $\lambda_{AN}$ | Longitude of the ascending node |
| $\lambda_{SL}$ | Longitude of the satellite |
| $\lambda_V$ | Longitude of the vertex (maximum latitude) |
| $\theta_{look}$ | Look angle |
| $L_{SA_{\max}}$ | Maximum achievable synthetic aperture length |
| $M$ | Mean anomaly |
| $n$ | Mean movement of the satellite |
| $R_m$ | Middle slant range |
| $u$ | Nodal angular elongation |
| $e$ | Orbit eccentricity |
| $i$ | Orbit inclination |
| $a$ | Orbit semi-major axis |
| $\upsilon$ | Orbit true anomally |
| $h$ | Platform height |
| $P_L$ | Power delivered to the load |
| $\wp$ | Power density [$W/m^2$] |
| $P_{ref}$ | Power reflected |
| $B_P$ | Processing bandwidth at the receiver |
| $\tau_0$ | Pulse duration |
| $T_P$ | Pulse repetition interval |
| $\sigma$ | Radar Cross section |
| $R_{ET}$ | Radius of the Earth at a given point $T$ |
| $R_{Pol}$ | Radius of the Earth at poles |
| $R_{Eq}$ | Radius of the Earth at the Equator |
| $\rho_{rg}$ | Range resolution |
| $F_n$ | Receiver noise factor |
| $A_r$ | Receiving antenna effective area |

| | |
|---|---|
| $L$ | Relative longitude between targets and satellite |
| $\Omega$ | Right ascension of the ascending node |
| $\Delta P$ | SAR processing improvement factor |
| $t_p$ | Satellite pass time through the perigee |
| $V_s$ | Satellite velocity |
| $f$ | Signal frequency |
| $R_r$ | Slant range reception link |
| $R_t$ | Slant range transmission link |
| $\sigma_0$ | Surface backscattering coefficient |
| $L_{SA}$ | Synthetic aperture length |
| $h_T$ | Target height over the reference Earth ellipsoid |
| $\eta_R$ | Target reflectivity |
| $\tau_R$ | Time delay of the received echo |
| $L_T$ | Total system losses |
| $B$ | Transmitted signal bandwidth |
| $\chi$ | Vernal equinox |
| $\lambda$ | Wavelength |
| $W_{ai}$ | Windowing in reception |

# LIST OF ACRONYMS

| | |
|---|---|
| ASR | Ambiguity to Signal Ratio |
| AN | Ascending node |
| APS | Atmospheric Phase Screen |
| AASR | Azimuth Ambiguity to Signal Ratio |
| AAP | Azimuth Antenna Pattern |
| DC | Duty Cycle |
| EM | Electro-Magnetic |
| EIRP | Equivalent Isotropic Radiated Power |
| GeoSAR | Geosynchronous SAR |
| GPS | Global Positioning System |
| JPL | Jet Propulsion Laboratory |
| LEO | Low Earth Orbit |
| NES0 | Noise Equivalent Sigma Zero |
| PIM | Passive Inter Modulation |
| PRF | Pulse repetition frequency |
| PRI | Pulse Repetition Interval |
| RCS | Radar cross section |
| RCS | Radar Cross Section |
| RASR | Range Ambiguity to Signal Ratio |
| RAR | Real Aperture Radar |
| R&D | Research and Development |
| RAAN | Right Ascension of the Ascending Node |
| SNR | Signal-to-noise ratio |
| SA | Synthetic Aperture |
| SAR | Synthetic Aperture Radar |
| TV | Television |
| TDBP | Time Domain Back-Projection |
| TWT | Travelling-Wave Tube |

# INTRODUCTION

In this document, a complete analysis on the feasibility of geosynchronous satellites to perform Synthetic Aperture Radar (SAR) acquisition is presented. SAR is an active radar technique used in remote sensing to get high resolution images which are not possible to obtain with conventional Real Aperture Radar (RAR) systems. In SAR, a single antenna collects information of the targets and the platform movement, where the antenna is fixed, is used to spread the Doppler history of received echoes improving the resolution of processed images. The transmitting antenna sends pulses periodically and receives the backscattered returns from the scene. The movement of the platform makes possible to illuminate the targets from different positions of the satellite trajectory, which is equivalent to have multiple antennas illuminating the scene at the same time (aperture antenna).

Therefore, SAR systems introduce some advantages with respect to other remote sensing techniques. The most significant are:

- Day/Night and all weather condition imaging since it does not depend on external power sources to detect the targets.

- Geometric resolution independent of altitude or wavelength.

- Signal features unique to the microwave region of EM spectrum which suffers less deterioration in atmospheric propagation (really important in space-borne acquisition).

Nowadays, SAR investigations are still improving the imaging features. These research activities provide better resolution images with more versatility of acquisition techniques. The increase of SAR popularity is due to the commercialization of SAR technology which in the first years only had military purposes. Among these new commercial possibilities, most notably could be sea surveillance and detection of boats, topographic mapping, forestry monitoring, natural disaster prevention and surveillance, etc. The increasing demand for SAR products is promoting the R&D of new SAR missions at international scale with better Earth coverage and spatial resolution.

However, the major drawback of the conventional SAR acquisition from Low Earth Orbits (LEO) is the revisit time. It corresponds to the period that the satellite takes to see the same part of the Earth from the same orbital position. This revisit time for LEO satellites typically goes from 3-4 days to 15-20 depending on the orbital parameters of the satellite. This intrinsic feature makes impossible to have continuous information of a determined zone of the Earth.

Here it is where the major improvement of SAR acquisition from Geosynchronous satellites (GeoSAR) can be found. Such systems have permanent monitoring of a determined zone of the Earth thanks to the nearly fixed orbital position. So, the GeoSAR

acquisition can be really helpful in fast evolving scenarios which require constant images to extract rapid information. This can be used in natural disaster prevention such in volcanic areas, consequences of urban terrain subsidence, earthquake prediction, oil slick or even atmospheric artefacts tracking. This last point can be really interesting for the Atmospheric Phase Screen (APS), an atmospheric propagation inhomogeneity that affects to the GPS signal acquisition which needs to be continuously monitored (each 10-20 minutes) due to its fast evolution. This could be achieved by a GeoSAR system considering its privileged orbital configuration. However, the long distances where the satellite is orbiting will be a problem due to the low power of the received echo. Long integration times (several minutes or hours) will be necessary to reach a minimum level of Signal to Noise Ratio (SNR) after the SAR processing.

Therefore, in this document the mission analysis of a GeoSAR system will be presented in order to determine the possibilities of such systems in SAR acquisition. First of all, an introduction to general SAR concepts is given to introduce the topic to inexpert readers. After that, a more concrete introduction to the GeoSAR concept is given. In this section, the GeoSAR technique is presented in the historical context and possible configurations and opportunities are presented.

Once the GeoSAR concept is introduced, a brief review on the orbital geosynchronous parameters is shown. After that, the SAR geometry of the geosynchronous satellite-target link is presented. This section is the starting point to understand the viability of these systems in SAR applications. Other SAR features of the GeoSAR acquisition such as the synthetic aperture formation, resolution, Doppler analysis or power link budged are presented after the orbital description.

Finally, a GeoSAR simulator is presented to reconstruct the raw data from a geosynchronous satellite. A time domain back-projection algorithm will be the processing scheme used to focus the received data. Several configuration and examples will be presented in this section to show the versatility of the GeoSAR acquisition.

# Chapter 1 SAR Basics

In this first chapter, the essential information about the basic concepts on the Synthetic Aperture Radar (SAR) techniques is presented in broad outline. It is intended for giving a brief refresh about the necessary concepts that will be used along this document. For further information about SAR concepts and performance, it is recommended to follow the references given in this first chapter.

## *1.1 Real Aperture Radar vs. Synthetic Aperture Radar*

The concept of Synthetic Aperture Radar (SAR) appeared as an alternative of Real Aperture Radar (RAR) which was extensively used in the beginnings of remote sensing science. The main goal of SAR techniques is to achieve better resolution images than RAR independent of the central frequency of the transmitted signal and the distance between the transmitting antenna and the illuminated surface.

The idea of an aperture radar is referred to the relative motion between the radar source (usually an antenna mounted on a satellite or an airplane) and the imaged surface. So, it is possible to create a kind of aperture antenna that can be used to image a wide area with a single small antenna. The way to receive and process the echoes coming from the surface distinguishes the Real and Synthetic Aperture Radars.

The RAR technique provides an azimuth resolution (along track direction, parallel to the relative motion target-source) which depends, basically, on the distance between the target and the illuminator and the beamwidth of the antenna. Then, this kind of techniques are not useful for spaceborne platforms neither airplane antennas if high resolution images are required.

The basic configuration of a Real Aperture Radar is presented in Fig. 1.1 (the geometrical concepts presented in Fig. 1.1 are also valid for SAR geometry). As it can be seen, the minimum distance at which two point targets can be distinguished in the along-track direction will be equal to the antenna footprint width. Knowing the azimuth or along-track antenna beamwidth ( $\theta_{az}$ ), the maximum achievable azimuth resolution ( $\rho_{az}$ ) will be obtained as:

$$\rho_{az} = \frac{h\theta_{az}}{\cos\theta_{look}} = \frac{h}{\cos\theta_{look}}\frac{\lambda}{L_a} \tag{1.1}$$

where the azimuth antenna beamwidth has been approximated by $\lambda / L_a$ being $L_a$ the antenna length. The terms $h / \cos\theta_{look}$ is the distance between the radar and the target (considering flat Earth approximation) where $\theta_{look}$ corresponds to the look angle presented in Fig. 1.1. As it has been previously commented, the azimuth resolution gets worse when the platform height and, consequently, the slant range to the target increases.

To avoid the azimuth resolution dependence with the sensor height, the Synthetic Aperture Radar technique was proposed. It takes advantage of the fact that the observed target is illuminated by the antenna beam for a long time. Then, recording and processing coherently the echoes received from this target, a better and non-distance dependant azimuth resolution is achieved.

This section is not intended to be an exhaustive description of the Synthetic Aperture Radar performance. Thus, only the final useful results are presented. In [1], [2] and [3], the Synthetic Aperture Radar technique is well described and most of the formulas of this chapter are derived and explained.

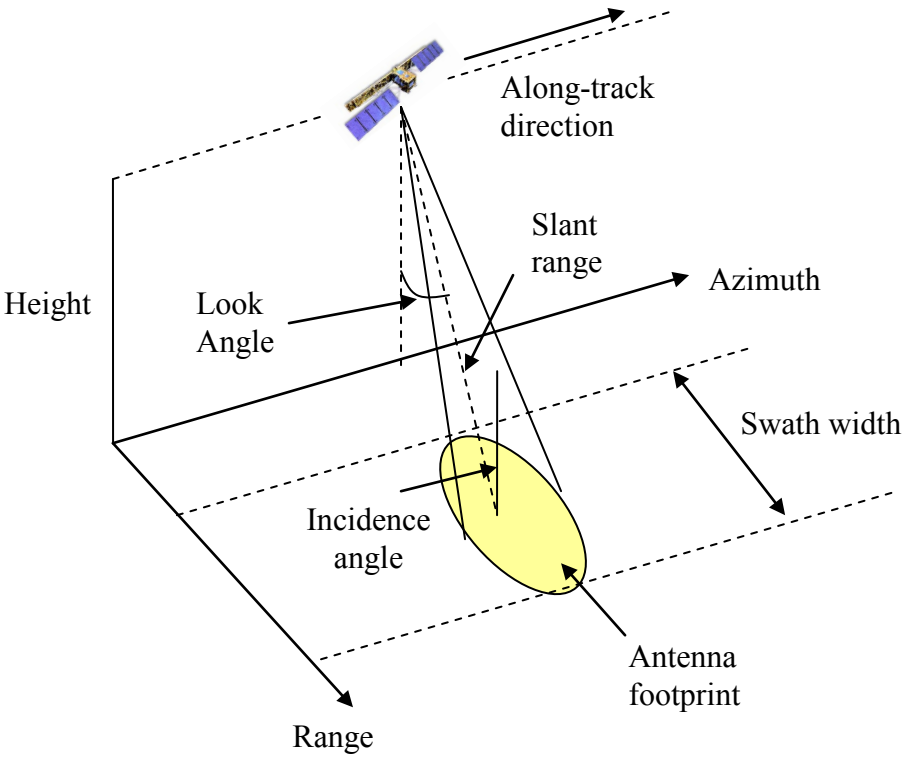


*Fig. 1.1 Basic geometry for RAR and SAR*

Therefore, considering the acquisition scheme of the Fig. 1.1, the finest azimuth resolution achievable by a SAR system is given by (1.2). As it can be seen, in a SAR system, the azimuth resolution does not depend on the distance neither the frequency. This feature makes SAR a strong and widely used technique for remote sensing applications.

$$\rho_{az} = \frac{L_a}{2} \tag{1.2}$$

## *1.2 SAR basic performance and parameters*

In this section, the principal SAR parameters that will appear in this document are introduced and the notation is presented. This can be useful to have a clear vision of the geometry of our problem and get in touch with the parameters that will be used later on the Geosynchronous SAR discussion. Most of the parameters used in the Geosynchronous SAR analysis are the same than in the conventional SAR, so it has been considered appropriate to present and clarify them previously.

### 1.2.1 SAR imaging coordinate system

Each positioning system has its own coordinate system to locate the targets in the scene univocally. So, while the real aperture radars have an angle-time delay format, in Synthetic Aperture Radar, a Doppler-time delay format is used. The Doppler shift is

produced by the relative movement between radar and the targets. So, a unique Doppler shift corresponds to each pointing direction. This can be observed in Fig. 1.2.

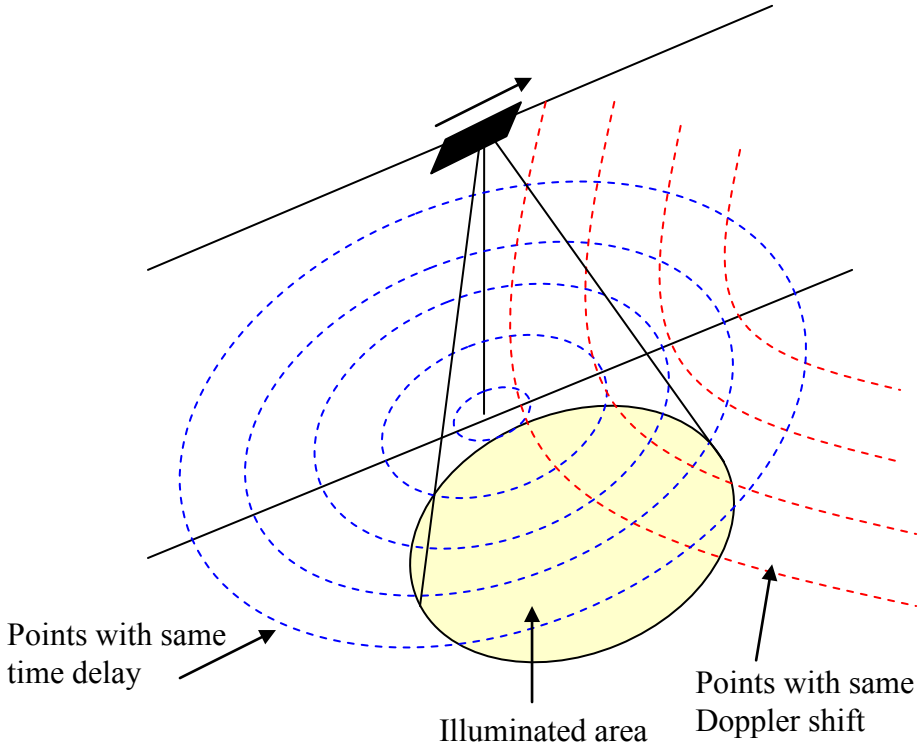


*Fig. 1.2 SAR image coordinate system for side-looking radar*

Considering this configuration, the echoes received from the points located on a sphere centred at the radar location will have the same delay. If these spheres are intersected with the surface plane where the targets are located, the result is a family of concentric circles, centred at the nadir point, defining lines of equidistance range to the sensor.

On the other hand, points located on coaxial cones with the flight line as the axis and the radar location as the apex will produce echoes with the same Doppler shift at the receiver. Once again, if these cones are intersected with the surface, a collection of hyperbolas with the same Doppler shift is obtained over the Earth's surface.

As it is shown in Fig. 1.2, for a given time delay and Doppler shift, there is an ambiguous point which has the same Doppler and time delay than the desired target. It can be easily discriminated pointing the antenna to the desired target (side-looking radar).

The brightness that is assigned to a specific pixel for imaging radar is proportional to the echo energy contained in the corresponding time delay Doppler shift bin which is unequivocally associated with a point on the scanned surface.

### 1.2.2 SAR parameters

In Fig. 1.1, Fig. 1.3 and Fig. 1.4, the most relevant parameters in a SAR system are presented. These figures show the geometry corresponding to a side looking imaging radar

(Fig. 1.1) and the range and the azimuth planes, Fig. 1.3 and Fig. 1.4 respectively. The parameters shown in these plots, valid for a conventional SAR in a spaceborne or an airplane, will be also useful for the Geosynchronous SAR proposed system.

In Fig. 1.1, the basic SAR geometry can be observed. The orbital parameters such as platform height ($h$) and velocity ($V_s$) will define other geometric parameters of the system as it will be explained next. The radar antenna footprint illuminates a surface spot on one side of the nadir track. As the platform moves in its orbit, a continuous strip is mapped along the flight direction (swath).

Two perpendicular directions can be defined in SAR geometry. The along-track direction, parallel to the flight path of the satellite, is usually called azimuth. On the other hand, the direction perpendicular to this one, cross-track direction, is called range.

An important parameter in SAR geometry that appears in Fig. 1.3 is the look angle ($\theta_{look}$). This corresponds to the angle between nadir and the direction where the antenna is pointing. Changing this angle, it is possible to switch between different swaths illuminating several zones of the Earth's surface. The combination of some swaths will provide higher range coverage for some scanning modes. Other important concepts in SAR geometry are the middle slant range ($R_m$), which is the distance between the platform and the middle of the swath. The ground range is the distance between the nadir point and the targets into the illuminated surface. The near and far ranges can be also defined as the distance between the radar and the nearest and furthest points in the swath respectively.The swath width for a fixed look angle obtained with the platform movement can be computed from the parameters in Fig. 1.1 as:

$$S \simeq h\theta_r / \cos^2 \theta_{look} = \lambda h / W \cos^2 \theta_{look} \tag{1.3}$$

where $\theta_r$ is the elevation beamwidth of the antenna, which can be approximated as $\theta_r = \lambda / W$, being $W$ the antenna width.

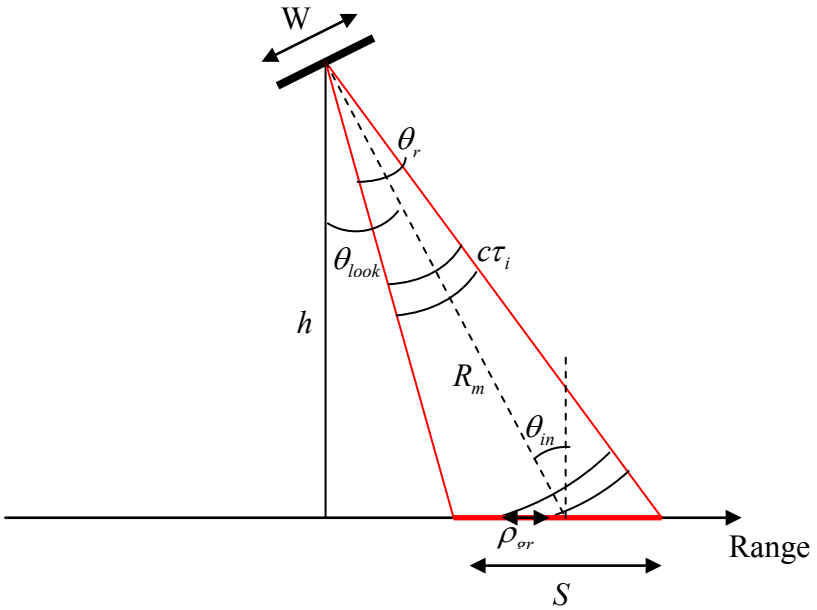


*Fig. 1.3 Elevation plane geometry for SAR systems*

The antenna footprint width in the azimuth direction, defined as $X_{az}$ in Fig. 1.4, will determine the observation time of the targets which is equal to the time while a point target is illuminated by the main beam of the antenna. So, it will be related with azimuth beamwidth ( $\theta_{az}$ ) of the antenna. The observation (or integration) time per target is calculated from the satellite parameters as:

$$T_i = \frac{X_{az}}{V_s} = \frac{\theta_{az} \cdot R_m}{V_s} = \frac{\lambda}{L_a} \frac{h / \cos\theta_{look}}{V_s} \tag{1.4}$$

Regarding the azimuth resolution presented in equation (1.2), it can be related with the integration time as in (1.5). As it can be seen, larger distance does not means worse resolution since it can be compensated by a larger integration time. Furthermore, as it was previously commented, the dependence of the azimuth resolution with the operation frequency is also eliminated in SAR acquisition.

$$\rho_{az} = \frac{\lambda}{2} \frac{R_m}{T_i \cdot V_s} = \frac{L_a}{2} \tag{1.5}$$

In the range plane (Fig. 1.3), the look angle ( $\theta_{look}$ ) and elevation beamwidth ( $\theta_r$ ) can be observed clearly. The impact of the pulse duration ( $\tau_i$ ) on the range resolution ( $\rho_{gr}$ ) can be also observed. The range resolution for a SAR acquisition is computed as [1] [2] [3]:

$$\rho_{ra} = c\tau_i / 2\sin\theta_{look} \tag{1.6}$$

As it can be seen, neither the azimuth nor the range resolutions depend on the frequency and the platform height.

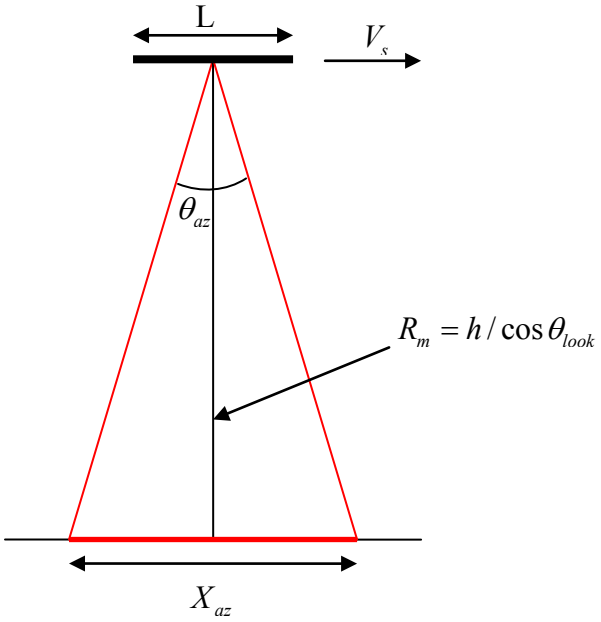


*Fig. 1.4 Azimuth plane geometry for SAR systems*

Another angle that can be observed in Fig. 1.3 and which will be used along this document is the incidence angle ($\theta_{in}$) which corresponds to the angle between the direction of arrival of the pulses into the surface and the normal vector perpendicular to the incidence plane. Most of the results of this document are given in function of this angle.

## *1.3 SAR achievable results and constraints*

When a SAR imaging system is designed, a large number of parameters have to be chosen in order to fulfil the desired input requirements. The end-to-end design involves tradeoffs between these parameters which are interrelated. The final design is the result of the system designers, the hardware engineers, the platform engineers and scientific users' interactions. Consequently, it is necessary to do a large number of iterations to obtain the final configuration for the SAR system.

For a Geosynchronous SAR system, the same constraints must be fulfilled in order to assure the correct performance of the radar. However, the most critical parameter will be the signal to noise ratio since the satellite is placed at a Geosynchronous orbit 42.164Km far away from the Earth's centre. Furthermore, another critical parameter will be the achievable resolution. Both of them will be related to the integration time considered.

Other features to be studied in this report for the Geosynchronous SAR that will define the system performance are the desired swath coverage which mostly determine our antenna geometry, the desired range and azimuth resolutions, integration time, the ambiguity suppression, the noise equivalent sigma zero (NES0), etc. In the following sections, all the geometric parameters for the Geosynchronous orbit will be accurately described and an analysis of the radiometric features of these kind of system for SAR observation purposes will be done.

# Chapter 2 Introduction to the Geosynchronous SAR concept

Once the basics on SAR have been introduced, now the concept of Geosynchronous SAR will be explained. The main purpose of a Geosynchronous SAR system is to obtain SAR images with continuous coverage by using the slightly perturbations on the orbit of a Geosynchronous satellite. The different possibilities, monostatic or bistatic systems, GeoSAR opportunities and constraints, as well as, a short review on the state of the art will be presented.

## *2.1 Geosynchronous satellites for SAR techniques*

The goal of a Geosynchronous SAR mission is to obtain SAR images using the relative motion of a geosynchronous satellite with respect to the Earth's surface. This motion, as it is explained in detail in Chapter 3, can be achieved by a slightly inclined orbital plane relative to the Equator which can be combined with small eccentricities on a satellite non-perfect geostationary orbit.

The potential advantage of using a geosynchronous satellite instead of a LEO, most widely extended in present SAR missions, is the possibility of having nearly continuous monitoring of a determined zone of the Earth. This can be really helpful in some kind of topography research, soil moisture determination, earth-quake prediction, terrain deformations and urban areas subsidence, natural disasters mapping as oil slicks and all the applications that have rapid evolution and where continuous information is required. The revisit time from several days to weeks limits the applicability of LEO satellites for those purposes.

As it has been explained in Chapter 1, any SAR system requires a relative motion between the illuminator and the imaged surface. This movement can be achieved by a Geosynchronous satellite, but with some peculiarities compared with the conventional LEO satellite tracks. The geosynchronous satellites are orbiting with an orbital period equals to the sidereal day of the Earth. Then, it could seem that the satellite position with respect to the rotating Earth reference system is fixed, but in practice, real orbits are always affected by slight perturbations. Those variations can be used to perform the required synthetic aperture.

The relative motion between the satellite and the Earth can be represented with the latitude and longitude histories of the satellite since the coordinates of a hypothetical fixed target would not vary. So, taking a rotating Earth system and considering a satellite with a perfectly circular orbit in the equatorial plane, it will have a fixed position on the sky. In a practical situation, the inclination of the orbit and the eccentricity as well, will modify the satellite fixed position. The shape and behaviour of the resultant Synthetic Aperture will be dependant of those parameters (see section 5.1). Just as a first approximation of what it is being explained without going on further details is shown in Fig. 2.1 to Fig. 2.4. For these examples, the nominal longitude of Hispasat-1D has been considered (30º-West). The relative motion changing the orbit inclination, eccentricity and argument of the perigee can be seen.

Fig. 2.1 shows the changes on the satellite track considering different orbit inclinations. An argument of the perigee of $\pi/2$ and an eccentricity of 0.05 have been considered for these plots. As it can bee seen, with a non-inclined orbit a line over the equator is described. On the other hand, when the inclination is increased the satellite has a higher excursion in latitude. But, as it has been explained, the eccentricity of the orbit can also modify the orbital behaviour described by the satellite.

In Fig. 2.2, the longitude variations produced by different orbit eccentricities can be seen. The amplitude of the East-West relative motion of the satellite is proportional to the orbit eccentricity. In that case, an inclination of 0.05 has been considered with the same argument of the perigee than in the previous example.

Finally, the orientation of the ellipse described by the satellite can be controlled with the argument of the perigee. In Fig. 2.3, this behaviour is shown. Then, playing with those parameters, the number of possibilities is really high which makes the Geosynchronous SAR a flexible system in terms of orbital configurations (Fig. 2.4).

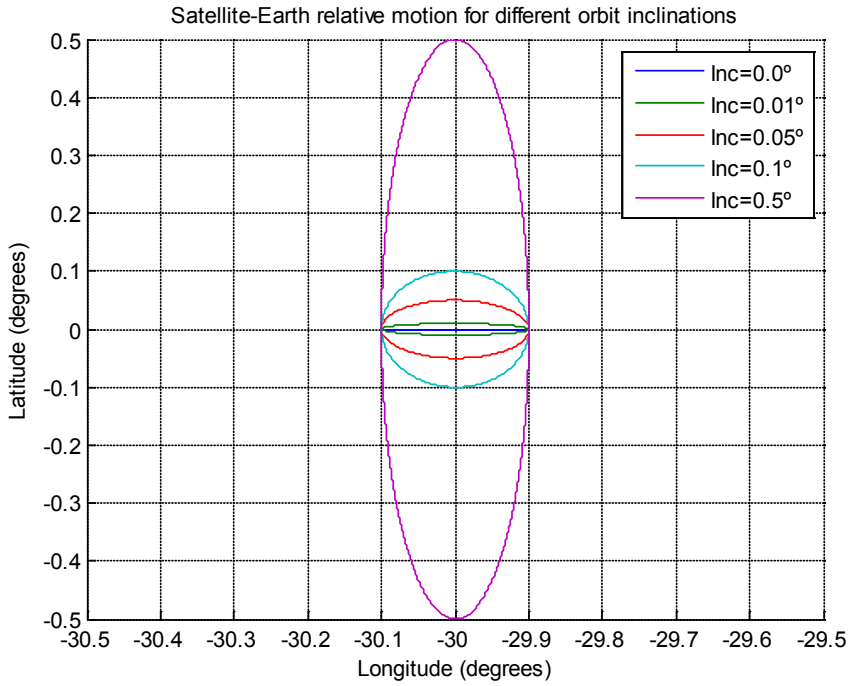


*Fig. 2.1 Latitudinal satellite motion considering several orbit inclinations*

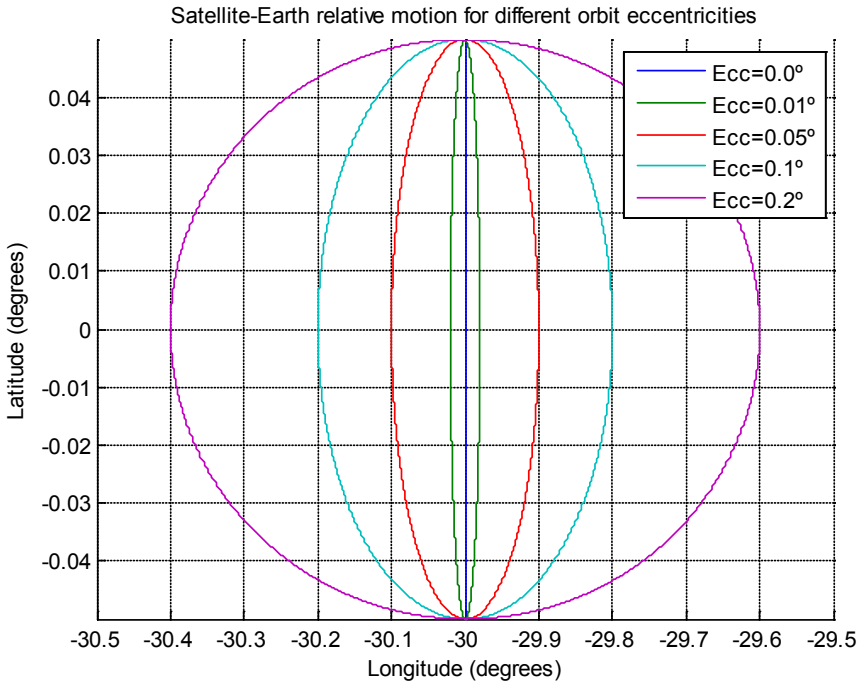


*Fig. 2.2 Longitudinal satellite motion considering several orbit eccentricities*

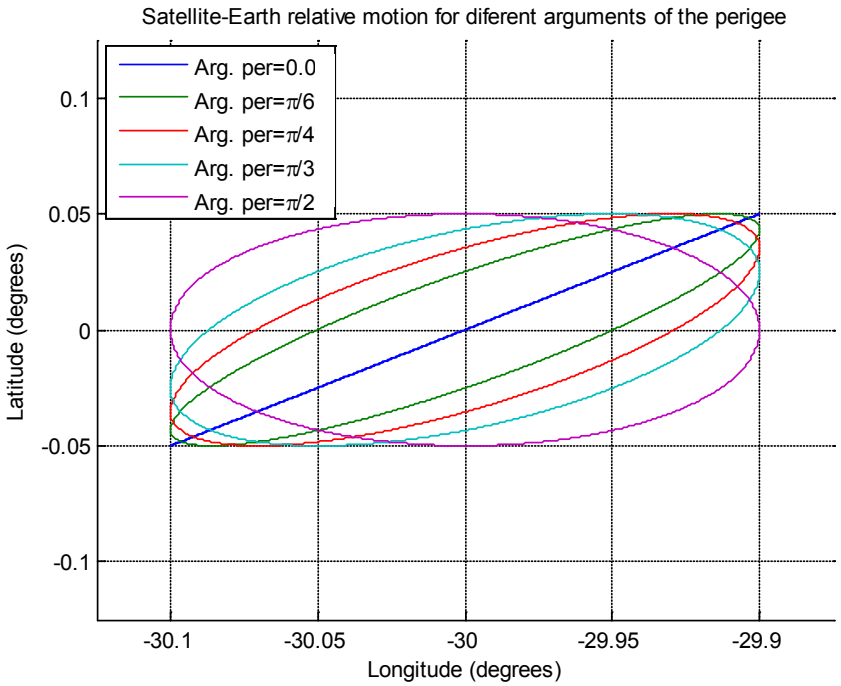


*Fig. 2.3 Satellite described motion modifying the argument of the perigee*

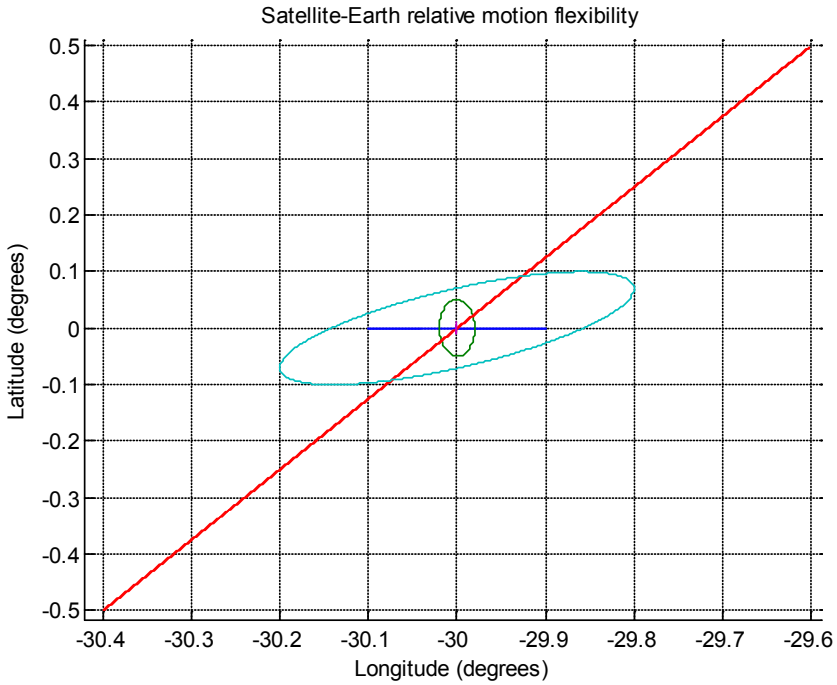


*Fig. 2.4 Satellite motion flexibility. Even the geosynchronous orbit, the possibilities are multiples*

But, why is Geosynchronous SAR an interesting alternative to the current LEO satellite missions? The question has been already introduced. First of all, and probably the most important reason is that a Geosynchronous satellite can provide daily coverage of one third of the Earth. Using these satellites for SAR purposes will give us the opportunity of having global images of a wide Earth area. Furthermore, it provides more flexibility since very high resolution can be achieved for some specific areas or it can provide a moderate resolution covering wider areas depending on the mission purposes. It is important not to forget the finer revisit time that can be obtained with respect to a LEO satellite and the several possibilities in the orbital relative motion shown in Fig. 2.4 playing with the orbit parameters.

## *2.2 Geosynchronous SAR opportunities*

The feasibility of a geosynchronous SAR system has been introduced in the previous section, showing that it is possible to get a kind of synthetic aperture using the relative motion of a satellite in a geosynchronous orbit. These deviations from an ideal geostationary orbit produced due to the orbit eccentricity and/or inclination will make possible the Geosynchronous SAR concept.

However, it is not the only constraint in a Geosynchronous SAR system. Considering that the satellite with a period of one sidereal day has to orbit at thousands of kilometres far away from the targets (35.000 to 40.000 Km), the low received power will be an important issue to take into account to achieve reasonable levels of Signal to Noise Ratio (SNR). One solution could be to increase the transmitted power in order to improve the received echo powers. But, in practice this is limited by on board available power and microwave transmitting technology. To simplify the SAR payload, the signal transmitted by the existing telecommunication satellites could be use as illumination of opportunity. In this case, the transmitted power dimensioned as a one-way downlink is limited in the order of 100 W.

Then, another possibility is to receive the strong echoes from high reflectivity targets. When the radar is pointing to the Earth's surface, the terrain illuminated will present different backscattering coefficients ($\sigma_0$) being impossible to assure a minimum level of SNR for small resolution cells. On that case, a possible solution to the low received power may be to increase the resolution cell, since the total RCS will be the $\sigma_0$ times the pixel area. However, the high incidence angles necessary to illuminate zones at medium latitudes in Europe can reduce the backscattered power even if shorts wavelengths are considered ($\sigma_0$ about -13 to -10 dB). Then, considering a resolution cell of 10 by 10 meters, the RCS would be 7 to 10 dB which will be easily below the receiver noise level.

However, another kind of target could be considered. Most of the geostationary satellites are TV broadcasting satellites pointing to determined zones of the Earth where a lot of parabolic antennas are steered to these satellites. This kind of metallic reflectors will have high reflectivity and their orientation towards the satellite will increase their RCS. Since these antennas need to have continuous direct link, it is expected that they always be in visibility of the satellite, well pointed and very stable mounted. Furthermore, the development of the satellite TV during the last years has increased the number of these parabolic antennas making them really interesting for Geosynchronous SAR purposes. In particular, such parabolic antennas could be useful to monitor urban areas where the

concentration of that kind of reflectors is very high. Fig. 2.5 shows the distribution of the parabolic antennas in the world. As it can be observed, the major concentration of these reflectors is in Europe. Furthermore, an increase of a 22% in the world during the period from 1999 to 2002 is observed. Then, they will be an interesting opportunity to monitor urban areas and assure at least in those zones (especially in Europe) a very dense coverage of stable and bright targets.

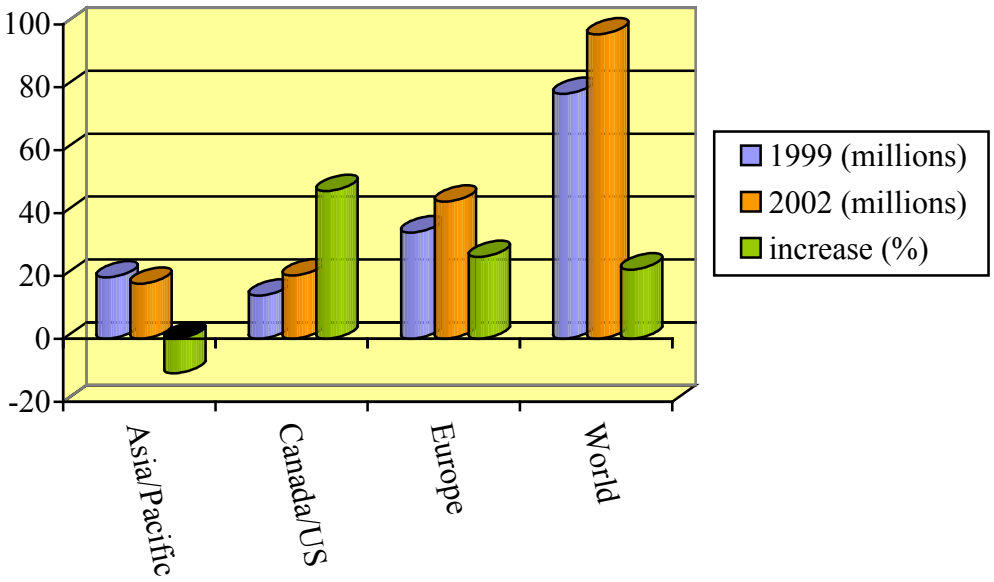


*Fig. 2.5 Number of user home parabolic antennas.*

However, the response of a parabolic antenna as a remote sensing scatterer has not been tested yet. It will depend on the reflector characteristics and the mismatch produced due to the feeder which will reflect the satellite signal back to the dish again. In the following lines, a detailed theoretical approach is presented taking the basic backscattering formulas of radar. The radar backscattering coefficient or RCS ( $\sigma$ ) can be defined as the coefficient between the electric field scattered by the target ( $E_s$ ) squared and the electric field incident to the target ( $E_i$ ) squared for far distances. Equivalently, it can be related to the scattered and incident power densities, $\wp_s$ and $\wp_i$ respectively, as in (2.1).

$$\sigma = \lim_{R\to\infty} 4\pi R^2 \frac{|E_s|^2}{|E_i|^2} = \left\{ \wp = \frac{|E|^2}{\eta_{wave}} \right\} = \lim_{R\to\infty} 4\pi R^2 \frac{\wp_s}{\wp_i} \qquad (2.1)$$

Then, the field or power density scattered by the parabolic antenna must be computed to determine the RCS. Two different contributions will influence to the total reflected signal. The former one corresponds to the non-guided reflected power due to the reflexions on the structure, supports, etc. The non-guided reflections will be a second order term and, consequently, they are neglected in this RCS analysis. The dominant term, and the one studied in this section, corresponds to the guided reflection in the output port of the feeder. The analyzed scheme is presented in Fig. 2.6 a). The incoming signal (red slashed lines) hits the parabolic dish which reflects the signal to the feeder (red lines). Considering an

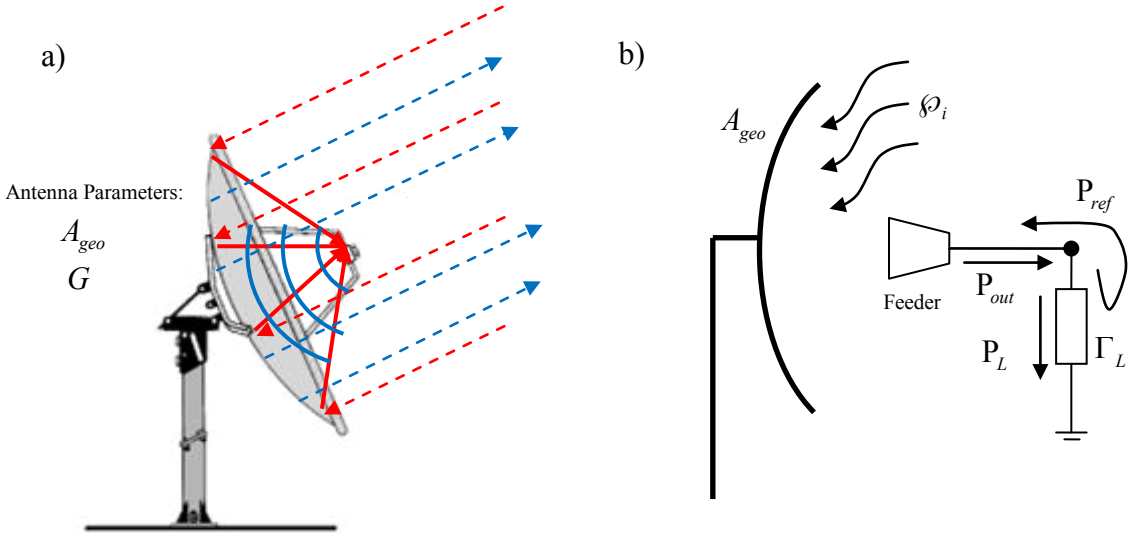


*Fig. 2.6 a) Parabolic antenna working as an scatterer. b) Feeder mismatch: power reflected and not delivered to the load.*

incidence power density $\wp_i$ and taking the parabolic antenna geometrical area ( $A_{geo}$ ), the power intercepted by the parabolic disc can be computed as:

$$P_i = \wp_i A_p = \wp_i A_{geo} \tag{2.2}$$

where $A_p$ corresponds to the projected area in the direction of illumination. In the case studied, the parabolic reflectors will be faced to the transmitting satellite to assure the correct reception of the signal. Then, the projected area can be approximated directly with the geometric area ( $A_{geo}$ ).

On the other hand, not all the intercepted power by the dish is reflected and transmitted to the feeder. Another important parameter of the parabolic antenna (dish + feeder) is the efficiency. So, the power delivered to the output port of the feeder will be:

$$P_{out} = P_i \eta_{eff} = \wp_i A_{geo} \eta_{eff} = \wp_i A_{eff} \tag{2.3}$$

The efficiency of the antenna ( $\eta_{eff}$ ) accounts for the ohmic losses and illumination efficiency of the whole antenna. It can be computed from the antenna gain as:

$$G = \frac{4\pi}{\lambda^2} A_{eff} = \frac{4\pi}{\lambda^2} A_{geo} \eta_{eff} \rightarrow \eta_{eff} \triangleq \frac{G}{A_{geo}} \frac{\lambda^2}{4\pi} \tag{2.4}$$

Once the signal is collected by the feeder, it is transmitted to a load which is not usually perfectly matched to the transmission line. Then, a fraction of the output port power ( $P_{out}$ ) is delivered to the load ( $P_L$ ) while the rest is reflected and sent back to the feeder. The delivered and reflected powers can be obtained as:

$$P_L = P_{out} \left(1 - \left|\Gamma_L\right|^2\right) \tag{2.5}$$

$$P_{ref} = P_{out} \left|\Gamma_L\right|^2 \tag{2.6}$$

The reflected power will be re-radiated by the antenna. So, the power density backscattered by the antenna is related with the incidence power density as follows:

$$\wp_s = \frac{P_{ref} G}{4\pi R^2} = \frac{P_{out} |\Gamma_L|^2 G}{4\pi R^2} = \frac{P_{out} |\Gamma_L|^2 A_{eff} \frac{4\pi}{\lambda^2}}{4\pi R^2} = \frac{\wp_i A_{eff} |\Gamma_L|^2 A_{eff} \frac{\cancel{4\pi}}{\lambda^2}}{\cancel{4\pi} R^2} = \tag{2.7}$$

$$= \wp_i |\Gamma_L|^2 \frac{A_{eff}^{\ 2}}{\lambda^2 R^2}$$

Finally, using (2.7) in the RCS equation (2.1), the backscattering coefficient for the parabolic antenna can be expressed as:

$$\sigma = \lim_{R\to\infty} 4\pi R^2 \frac{\wp_s}{\wp_i} = \lim_{R\to\infty} 4\pi \cancel{R^2} \cancel{\wp_i} |\Gamma_L|^2 \frac{A_{eff}^{\ 2}}{\lambda^2 \cancel{R^2}} \frac{1}{\cancel{\wp_i}} = \boxed{\frac{4\pi}{\lambda^2} A_{geo}^{\ 2} \eta_{eff}^{\ 2} |\Gamma_L|^2} \tag{2.8}$$

In Table 2.1, the RCS has been computed taking the parameters of some commercial parabolic antennas. The most used frequency bands (Ku and C) for Satellite TV broadcasting have been considered. The RCS is computed for different antenna diameters and gains. A typical low-noise reflexion coefficient of -10dB ( $20\log|\Gamma_L|$ ) has been considered for the feeder-load mismatch. Although values around the 30dBsm are obtained for larger antennas, the 60cm diameter dishes are the commonly used for user satellite TV receivers in Europe. Therefore, values of RCS around 20dBsm are expected in most of the cases.

| Brand | Model | Freq. | Band | Diameter | Area | Gain | $\eta_{eff}$ | RCS (dBsm) |
|---|---|---|---|---|---|---|---|---|
| TECATEL | 135+LNB | 12.6GHz | Ku | 135cm | 1.43m$^2$ | 43 dB | 0.63 | 32.55 |
| TECATEL | 80+LNB | 12.6GHz | Ku | 80cm | 0.50 m$^2$ | 38,3 dB | 0.61 | 23.14 |
| XINSHI | XS-KU-60-I | 12.5GHz | Ku | 60cm | 0.28m$^2$ | 36.67dB | 0.77 | 20.06 |
| FORTEC | FS6D | 4.0 GHz | C | 180 cm | 2.54m$^2$ | 35.89 dB | 0.68 | 28.23 |
| FORTEC | FC08 | 4.0 GHz | C | 240 cm | 4.52m$^2$ | 38.39 dB | 0.68 | 33.24 |

*Table 2.1 RCS of parabolic antennas depending on the geometric and frequency parameters*

## 2.3 Monostatic vs. Bistatic configurations

The Geosynchronous SAR basics have been introduced in the previous sections. Another important point is how to conceive the Geosynchronous system. In a first approximation, two main configurations can be taken into account: a monostatic or bistatic system. Both of them present some advantages and drawbacks that have to be considered and studied carefully to determine the best option for each acquisition. Here, the most significant features and critical problems are presented for both alternatives.

The monostatic configuration consists on a single satellite orbiting in a geosynchronous orbit. The first possibility is to re-use the signal sent by a telecommunications broadcast

satellite (broadcasting satellite TV) having on board a receiver tuned on the same frequency than one of the transmitters. The principal drawback of the monostatic Telecommunications Compatible SAR is the Passive Inter Modulation (PIM). Having several transmitters working at similar frequencies, the intermodulation products will interfere the reception of the desired band. As it is shown in Fig. 2.7, the most damaging interference will come from the third order intermodulation products ( $2f_{tx_i} - f_{tx_j}$ ). The combination of two adjacent channels ( $f_{tx_2}$ and $f_{tx_3}$ ) can produce harmonics which interfere to the desired receiving band ( $B_{Rx}$ ).

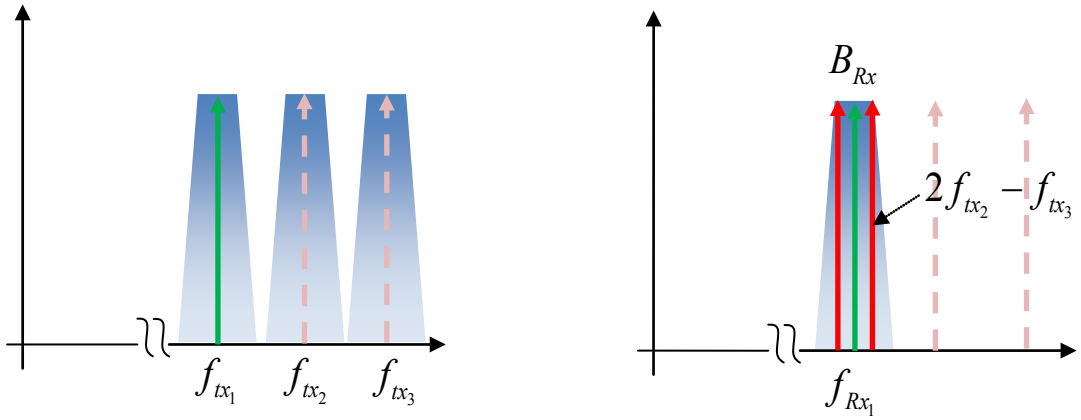


*Fig. 2.7 Passive Inter Modulation (PIM) in the receiver*

Furthermore, as all monostatic radar system, it is necessary to switch on and off the transmitter, dividing the time between transmission and reception. This requires more complex hardware and, at the same time, reduces the window for recording echoes. Furthermore, such use is not compatible with the current TWTs for telecommunications that are designed to operate continuously. Regarding the power budget, a penalization in the available peak power and a reduction of the duty cycle will be the most significant consequences of the monostatic configuration.

On the other hand, the monostatic configuration present a simpler way of operation since the transmitter and the receiver will travel on the same platform having the same motion. This will make easier the SAR processing data and all the post-processing work.

For this reason, the monostatic configuration is taken as an interesting alternative even the commented issues. So, the study on this field must be focused on the reduction of the PIM since that kind of system would be compatible with the future geostationary communication satellites launched in the following years. Another possibility in the monostatic case would be the utilization of a ad-hoc geosynchronous satellite for SAR purposes with a single transmitter and a single receiver. Obviously, the PIM problems will be avoided but the mission costs will raise considerably compared with the Telecommunications Compatible SAR where only a receiver in the payload of a broadcasting satellite would be necessary.

As an alternative to the monostatic proposed systems, the bistatic configuration can be also interesting for Geosynchronous SAR applications. It consists on a two geostationary sensors one of them working as illuminator whereas the receiver is placed in the other. This way, having both satellites separated hundreds of kilometres away, the PIM will not

be so problematic if no in-band transmitters are placed on the receiver satellite. Besides, all the time can be exploited for transmitting and receiving (a 100% of duty cycle). In this case, an illuminator of opportunity can be also used as a transmitter.

Nevertheless, the bistatic configuration presents other drawbacks. The presence of two satellites makes more complex the analysis of the receiver echoes, since the motion of the transmitter and the receiver is different. Another issue to take into account in the bistatic case is the scattered power loss due to the alignment of the parabolic reflectors towards the illuminator but not the receiver. This will cause an important deterioration in the received SNR that has to be carefully analysed.

Even so, the bistatic configuration seems to be the most adequate configuration for their flexibility in the receiver and the better performance against the transmitter interferences. All these qualitative problems here explained will be analysed in detail along these report to have a clearer evidences of the performances of both systems. In Fig. 2.8, examples of a monostatic and a bistatic configuration are presented.

As it can be seen, in the monostatic case the time is divided between transmission and reception with a 50% of duty cycle. On the other hand, in the bistatic configuration, the transmitter and the receiver are in operation during all the time with a 100% of duty cycle as it has been explained. It can be seen that in a bistatic system, the mismatch between the transmission and reception footprints can cause a reduction of the coverage of the system. Then, high precision in the satellite and antenna attitude are required in order to steer the receiver satellite footprint to the transmission one.

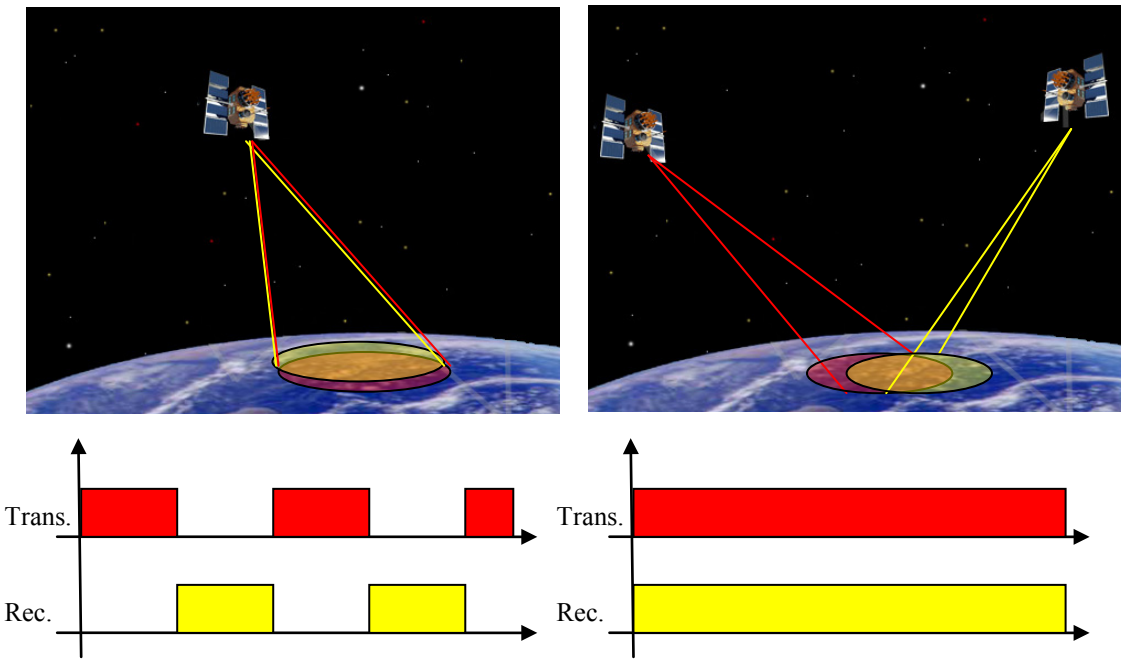


*Fig. 2.8 Monostatic vs. bistatic configurations*

In Table 2.2, the most significant features of both configurations are summarized and compared. The monostatic column corresponds to the dedicated SAR example previously presented. A reception dedicated satellite and illuminator of opportunity have been considered for the bistatic case. The green cells indicates an advantage with respect to the other case while the red ones a drawback.

| Features | Monostatic | Bistatic |
|---|---|---|
| **Configuration** | Single satellite | 1 satellite + 1 illuminator of opportunity |
| **Trans. Signal** | Radar Pulse / Downlink | Broadcasting |
| **Interferences** | PIM/co-channel | Low |
| **Duty cycle** | <50% | 100% |
| **# of channels** | 1 bidirectional | 1 download |
| **EIRP requirements** | 70 dBW (dedicated) | 70 dBW (re-used) |

*Table 2.2 RCS of parabolic antennas depending on the geometric and frequencial parameters*

As it has been introduced along this chapter, the concept of a Geosynchronous SAR system presents a lot of challenges to face up. Besides, it is an interesting system since it could allow a new range of applications that are not possible with the current LEO-SAR schemes. Then, after this brief introduction to the Geosynchronous SAR concept, in the following chapters the orbit and system features will be studied in more detail to obtain the first results about the feasibility of this new trend in SAR missions.

## *2.4 Geosynchronous SAR context. State of the art*

The Geosynchronous SAR concept was firstly proposed by Kiyo Tomiyasu in the early eighties [4]. Tomiyasu demonstrated the feasibility of a mission with a Geosynchronous satellite to obtain SAR images of the American continent with a resolution of 100 m by using the attitude of those satellites. This way, the whole continent could be monitored in about three hours of segmented operation. The power link budget obtained by Tomiyasu proved that a sufficient SNR level could be reached working at 2450MHz with a transmitted average power of 1312W.

The investigations on Geosynchronous SAR did not end up there. Some years later, several studies on the feasibility of those systems were done. In 1998, a passive geosynchronous SAR system was proposed by Prati *et al* [5]. In this proposal, a SAR system is conceived by using a receiver located on a geosynchronous satellite which is

illuminated by the backscattered energy of a broadcast digital audio or TV signals. Here, the concept of signal reusing and illuminators of opportunity appears for the first time. Other ground based experiments of bistatic SAR have been done after year 2000 [6]. All of them were based on previous studies presented by the Politecnico of Milano some years before [7] [8]. Furthermore, the JPL presented a study for Earth Mapping and disaster management by using high power GeoSAR system [9].

In this document, a detailed study on the feasibility of Geosynchronous SAR will be presented taking benefit of those previous analyses and assessing the unsolved issues.

# Chapter 3 Geosynchronous orbit considerations

In this chapter, a detailed analysis of Geosynchronous orbits is provided in order to determine the motion of the satellite with respect to the targets on the Earth. This study is necessary to understand and characterize the synthetic aperture that will define our SAR system.

## 3.1 Geosynchronous orbit parameters

The movement of a satellite in a geosynchronous orbit is governed, as well as all orbiting bodies, by the Kepler's laws. Kepler determined that the trajectories of planets around the Sun were elliptical. This concept can be applied to the satellite motion around the Earth as well. Then, a Keplerian system defines the relative motion between two point bodies (satellite-Earth system) under the sole influence of the gravitational attractions.

The Kepler laws were extended and mathematically characterized by the Newton's law [10]. From that formulation, the orbit described by any satellite around the Earth can be characterized by the ellipse defined in (3.1).

$$r = \frac{a\left(1-e^2\right)}{1+e\cos\upsilon} \tag{3.1}$$

$a$ is the semi-major axis of the ellipse described by the orbiting body, $e$ is the orbit eccentricity and $\upsilon$ is the true anomaly. As it can be seen, the radius of the orbit will be maximum when the true anomaly has a value of $\pi$. The maxim distance to the Earth is called apogee. On the other hand, when the true anomaly is zero, the radius will be minim which is called perigee. Then, the true anomaly is the angle between the direction of the perigee and the current position of the satellite. The basic parameters that will define the satellite orbit can be seen in Fig. 3.1.

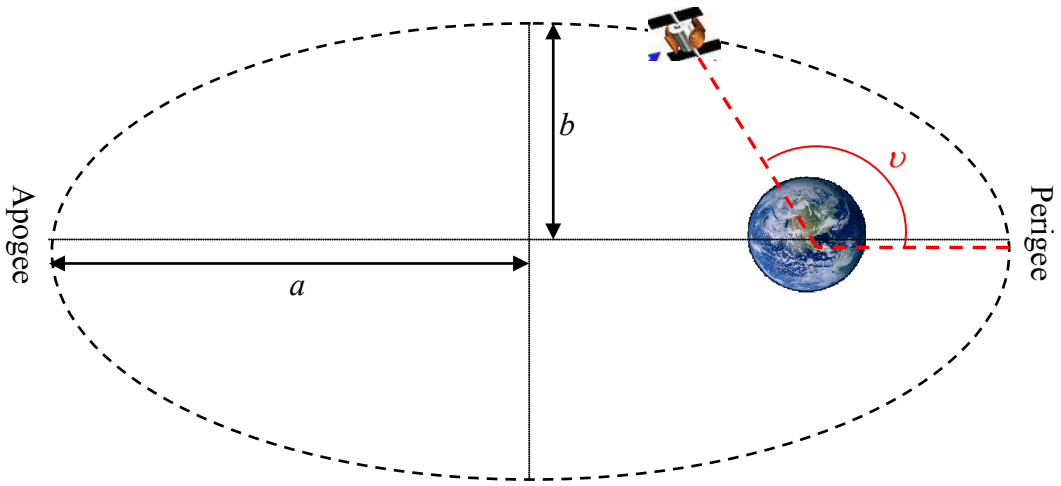


*Fig. 3.1 Satellite orbit basic parameters*

The orbit eccentricity is obtained as the ratio between the semi-major axis (a) and semi-minor axis (b) of the ellipse as follows:

$$e = \sqrt{1-\left(\frac{b}{a}\right)^2} \tag{3.2}$$

On the other hand, using the third Kepler's law, it is possible to relate the semi-major axis of the orbit with the orbital period as in (3.3). $\mu$ is the Earth gravitational constant ($GM_E = 3.986 \cdot 10^{14} m^3 / s^2$).

$$T = 2\pi \frac{a^{3/2}}{\mu^{1/2}} \tag{3.3}$$

Considering a Geosynchronous satellite with an orbital period equals to the sidereal day (T=86164 seconds), and a quasi-circular orbit with low eccentricity ($e = 10^{-4}$), the orbital behaviour shown in Fig. 3.2 is obtained. A semi-major axis of 42164Km will characterize these satellites. The distance in the perigee is about 42160Km while in the apogee is 42168Km. These slightly differences are produced due to the small eccentricity considered in this example.

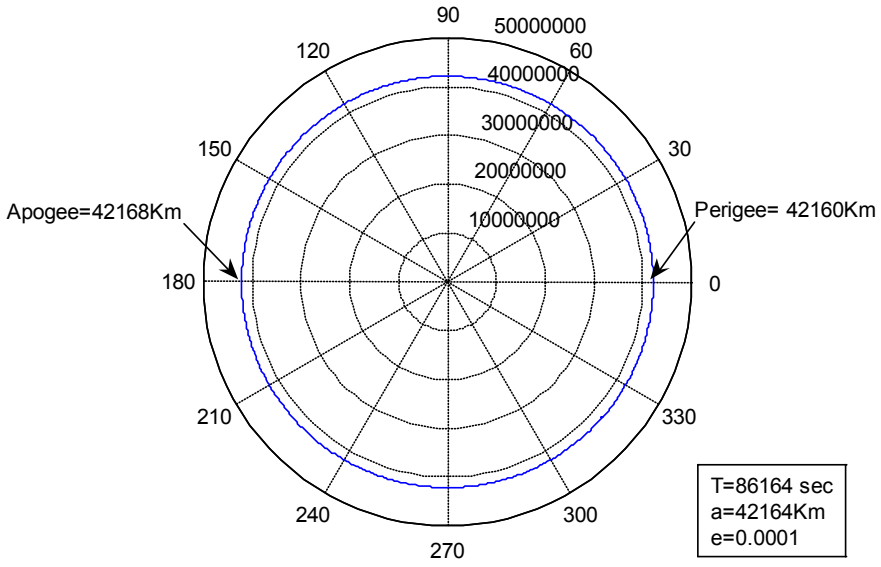


*Fig. 3.2 Geosynchronous satellite orbital behaviour and parameters*

From the radius of the orbit, the velocity of the satellite can be derived [10]:

$$V_s = \sqrt{\mu \left( \frac{2}{r} - \frac{1}{a} \right)} \quad [m/s] \tag{3.4}$$

Particularizing the expression (3.4) with the parameters of a geosynchronous satellite computed with (3.1) and (3.3), the relation between the satellite velocity and the orbital radius is shown in Fig. 3.3. The satellite velocity goes from 3074.35m/s to 3074.97m/s. Furthermore, regarding the second Kepler's law, the velocity is maxim when the satellite is in the perigee (closest point to the Earth) and minim in the apogee. The mean velocity of the satellite with respect to the Earth's centre can be computed as:

$$\bar{V}_s = \frac{2\pi a}{T} = 3074.66\, m/s \tag{3.5}$$

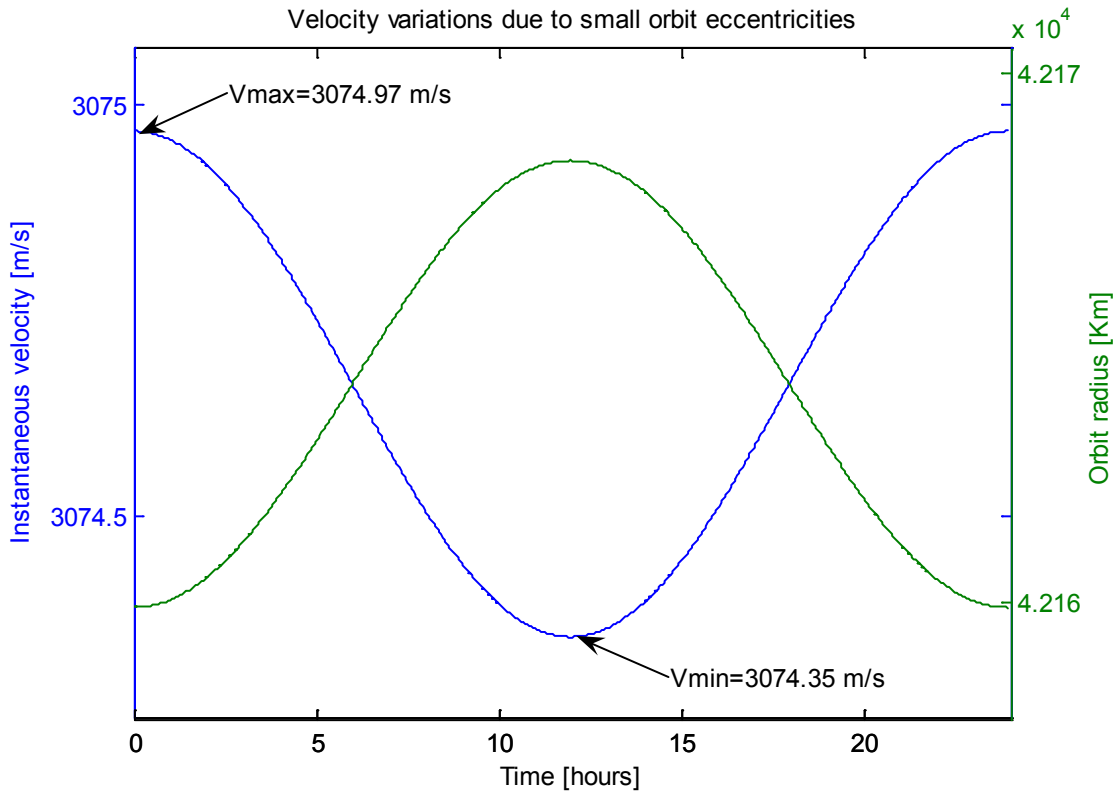


*Fig. 3.3 Geosynchronous satellite velocity range vs. orbital radius history*

## *3.2 Orbital parameters: determination of the orbit*

Once a first approximation to the orbit characteristics of a geosynchronous satellite has been presented, now the position of the orbital plane in space must be specified in order to have completely located the satellite trajectory around the Earth. In the previous section, the semi-major axis and the eccentricity of the ellipse have been introduced. The semi-major axis which was related to the orbital period by the third Kepler's law and the eccentricity determines the distance to the Earth and the satellite instantaneous velocity as well, but it does not give information about the orientation of the orbital plane with respect to the Earth.

Then, some extra parameters are necessary to completely define any kind of orbit. First of all, the *inclination* ($i$) and the *right ascension of the ascending node* ($\Omega$) will establish the position of the orbital plane in space. Besides, the orientation of the orbit in its plane will be given by the *argument of the perigee* ($\omega$). Let's see all these parameters with more details [12].

The *inclination* of the plane of the orbit is defined as the angle between the equatorial plane of the Earth and the orbital plane. This is counted positively between 0º and 180º at the ascending node. This parameter, already introduced in Chapter 2, will be really small, some tens of a degree in the case of geosynchronous satellites. Even so, the relative motion produced by this slightly variation from the equatorial plane will be enough to perform the synthetic aperture necessary for the system proposed.

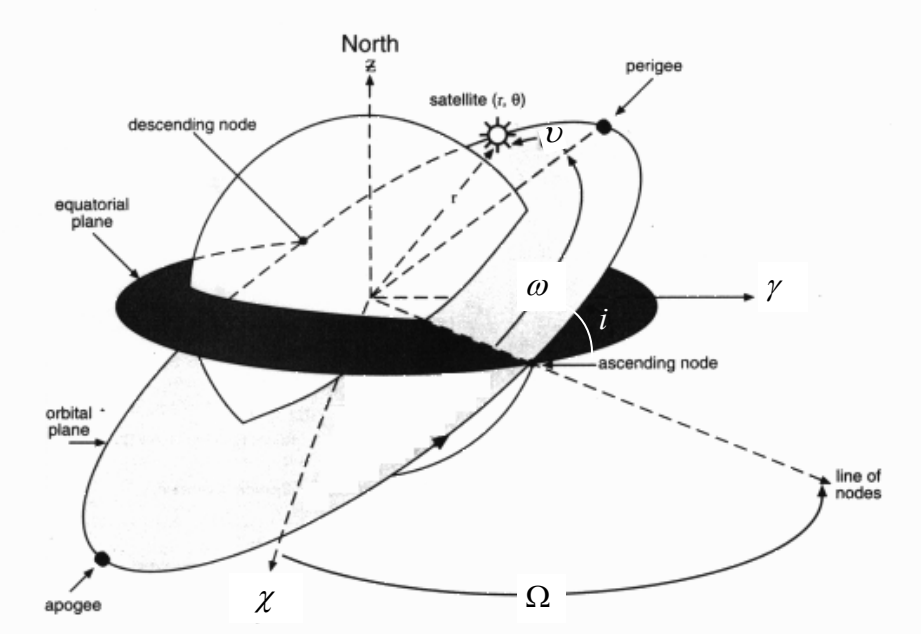


*Fig. 3.4 Satellite orbital parameters*

The other parameter that will define the position of the orbital plane was the *right ascension of the ascending node* (RAAN). It is the angle between the vernal equinox[1] ( $\gamma$ ) and the position of the ascending node. The orbital plane orientation is univocally determined by these two parameters.

Once the plane is located, a parameter fixing the orbit orientation in its plane is necessary. This parameter is known as the *argument of the perigee* ( $\omega$ ). This is the angle between the direction of the ascending node and the direction of the perigee taken positively from 0º to 360º.

Finally, the position of the satellite must be determined in the orbit at any time. Usually it is taken from the pass through the perigee ( $t_p$ ) which is considered as the reference initial time. Alternatively, the true anomaly ( $\upsilon$ ), described in Fig. 3.1, can be also used to identify the satellite position. All these parameters are represented in Fig. 3.4.

## *3.3 Geosynchronous SAR orbital parameters summary*

The basic parameters to determine any kind of orbit have been presented in the previous section. In this one, these parameters are summarized and the most relevant equations gathered in Table 3.1. The parameters with a value determined by the orbital configuration are marked in bold type. On the other hand, for those parameters that will be constantly changing along the satellite orbit, a range of reasonable values is provided in order to have an idea of which magnitudes have to be considered. The orbital parameters such as the RAAN or the argument of the perigee have not been included in Table 3.1 since they can be chosen depending on the zone of the Earth to be monitored.

[1] The time at which the sun crosses the plane of the equator towards the relevant hemisphere, making day and night of equal length. It occurs about March 21 in the N hemisphere (Sept. 23 in the S hemisphere).

| Parameter | Symbol | Formula | Typical values for geosynchronous satellites |
|---|---|---|---|
| Radius vector of the orbit | $r$ | $r = \frac{a\left(1-e^2\right)}{1+e\cos\upsilon}$ | 42100Km – 42200Km |
| Orbit semi-major axis | $a$ | $a = \left(\frac{T\mu^{1/2}}{2\pi}\right)^{2/3}$ | **42164Km** |
| Orbital period | $T$ | $T = T_{sidereal}$ | **86164sec** |
| Instantaneous velocity | $V_s$ | $V_s = \sqrt{\mu\left(\frac{2}{r}-\frac{1}{a}\right)}$ | 3070m/s-3080m/s |
| Mean velocity | $\overline{V}_s$ | $\overline{V}_s = \frac{2\pi a}{T}$ | **3074.66m/s** |
| Orbit inclination | $i$ | - | $< 1^{o}$ |
| Orbit eccentricity | $e$ | $e = \sqrt{1-\left(\frac{b}{a}\right)^2}$ | $< 0.01$ |

*Table 3.1 Geosynchronous orbital typical parameters and formulas summary*

# Chapter 4 Geosynchronous SAR Geometry

The basic orbital parameters for a geosynchronous satellite have been defined in the previous chapter. In this one, a geometric analysis of the satellite-target link is presented. The satellite track over the surface, the distance to Earth located targets, the most significant angles (elevation, azimuth, and incidence) and other geometrical important parameters for the SAR acquisition will be defined and computed. This analysis will be helpful to determine some geometric characteristics that will be used in the GeoSAR simulations and link budget calculations.

## *4.1 Review of basics on the geometry of the sphere*

Firstly, before the analysis of the geosynchronous geometric parameters, in this section a brief introduction to the essential concepts on spherical trigonometry will be presented since they will be used along this section to obtain the relations between the different geometric parameters that define a geosynchronous SAR system.

To understand the positions and motion of any celestial body, it is necessary to have a clear understanding of spherical geometry. This corresponds to the study of the geometry over the surface of a sphere. First of all, a great circle of a sphere is defined since all the formulas on spherical trigonometry are referred to this concept.

A great circle, as it can be seen in Fig. 4.1 in red, is defined by the intersection of the sphere with a plane which contains the centre of the sphere. Any other intersection with a plane that does not contain the centre is known as small circle and they will not be useful for this analysis. Any great circle divides the sphere in two identical parts.

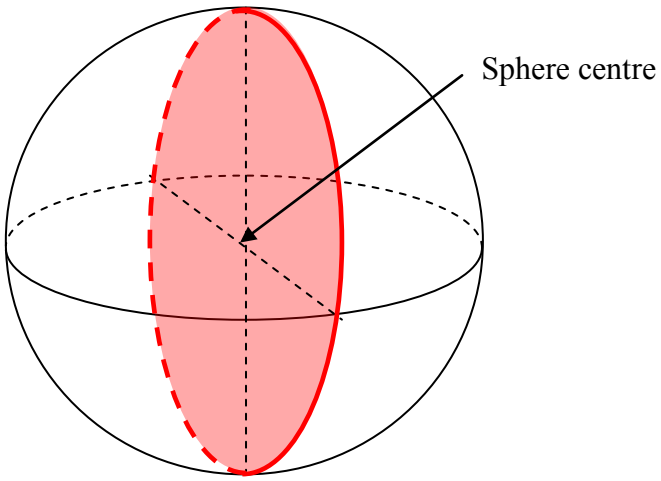


*Fig. 4.1 Geometry of the sphere. The great circles*

Once the great circles have been introduced, the spherical triangles are another concept necessary in the satellite motion analysis. A spherical triangle is a triangle drawn on the surface of a sphere whose sides are all arcs of great circles. Besides, any spherical triangle has to fulfil three additional properties:

a) Any two sides are together longer than the third one.

b) The addition of the three angles is greater than 180º.

c) Each individual spherical angle is less than 180º.

Some examples of what it is and what it is not a spherical triangle can be seen in Fig. 4.2. The triangle P-A-B is not a spherical triangle since the side AB is an arc of a small circle. On the other hand, the triangle P-C-D is a spherical triangle since all its sides are arcs of great circles.

It is important to see that the lengths of the sides of a spherical triangle are expressed in angular units. Considering that the length of an arc ( $s$ ) which subtends an angle ( $\theta$ ) at the centre of a circle of radius ( $r$ ) is given by $s = \theta r$ ; and knowing that all the arcs that compose the spherical triangle are segments of great circles with the same radius, it can be taken as unity; then the arc $s$ can be expressed directly as $s = \theta$ , with units of radians.

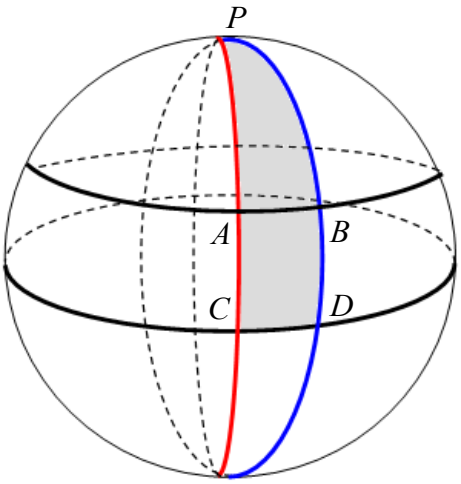


*Fig. 4.2 Spherical triangles over the sphere surface*

Similarly than working with triangles in planar trigonometry, it is necessary to use the formulation of spherical trigonometry to perform calculations with spherical triangles. The angle between two sides is defined as the angled formed between the tangents of the two crossing great circles at this point. In Fig. 4.4, the angle at vertex *B* is shown in more detail. Considering the spherical triangle of Fig. 4.3, formed by the arcs (*a, b, c*) and the vertex angles (*A, B, C*) some relations between them are given by the spherical trigonometric theorems.

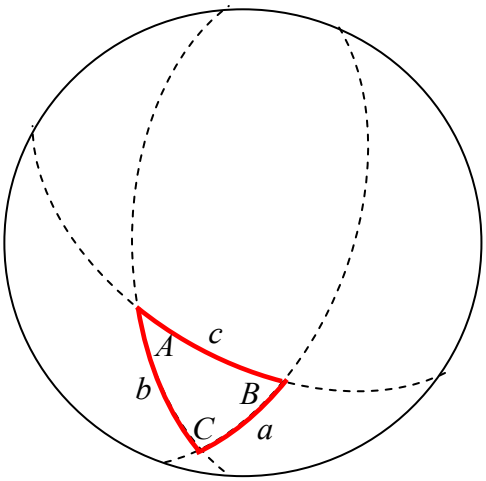


*Fig. 4.3 Spherical trigonometry over spherical triangles*

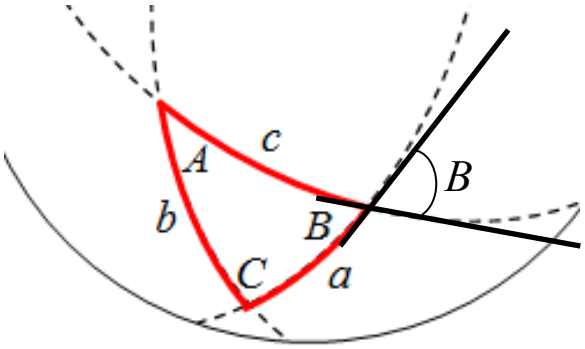


*Fig. 4.4 Vertex angle defined at point B between the tangents of the intersecting great circles at that point*

Then, the arc lengths (*a, b, c*) and the vertex angles (*A, B, C*) of any spherical triangle are related by the *Spherical Law of Sines* and the *Spherical Law of Cosines* [13]. These are the spherical analogues laws of the planar *Law of sines* and *Law of Cosines*. The formulas, not demonstrated in this document, are given in (4.1) and (4.2), respectively.

Spherical law of sines:

$$\frac{\sin a}{\sin A} = \frac{\sin b}{\sin B} = \frac{\sin c}{\sin C} \tag{4.1}$$

Spherical law of cosines:

$$\cos a = \cos b \cos c + \sin b \sin c \cos A \tag{4.2}$$

Other trigonometric properties of the spherical geometry that will be used in the following section are the polar cosine formula (4.3) and the cotangent formula (4.4) [13]:

$$\cos A = -\cos B \cos C + \sin B \sin C \cos a \tag{4.3}$$

$$\cos b \cos A = \sin b \cot c - \sin A \cot C \tag{4.4}$$

## *4.2 The geosynchronous satellite track*

The satellite track is defined as the locus of the points of intersection of the Earth's centre-satellite vector with the surface of the earth. This track has to take into account the earth rotation motion and the satellite movement. Then, it will give information about the relative motion between the satellite and a fixed point over the Earth's surface. Firstly, the formulation for a fixed earth will be presented and then the necessary modifications will be introduced to reproduce the actual situation with the rotating earth.

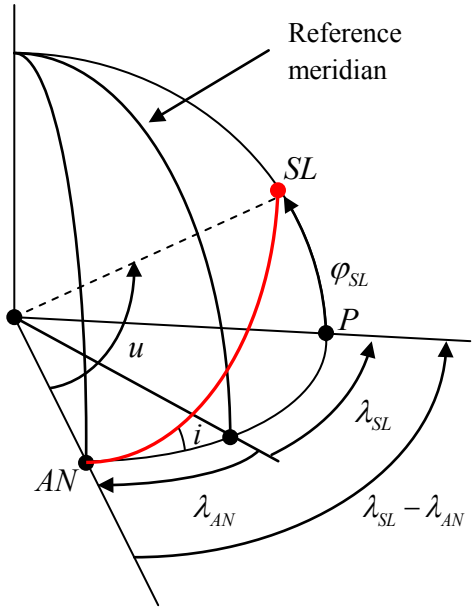


*Fig. 4.5 Satellite track fixed earth reference system*

The system considering a fixed earth is shown in Fig. 4.5. The coordinates of the satellite ($\lambda_{SL}$, $\varphi_{SL}$) defines the longitude and latitude at a given time with respect to a reference meridian and to the equator respectively. The longitude of the ascending node (AN) with respect to the reference meridian is called $\lambda_{AN}$ and it will be used to relate the longitudinal and latitudinal coordinates of the satellite. This can be obtained using the cotangent formula (4.4) in the spherical triangle AN-SL-P from Fig. 4.5. Equation (4.5) can be derived as follows:

$$\cos b \cos A = \sin b \cot c - \sin A \cot C$$

considering:

$$\begin{aligned} a &= u \\ b &= \lambda_{SL} - \lambda_{AN} \\ c &= \varphi_{SL} \end{aligned} \qquad \begin{aligned} A &= 90^{\circ} \\ C &= i \end{aligned}$$

where A, the angle at vertex P, is equal to 90º. Then:

$$\cos\left(\lambda_{SL} - \lambda_{AN}\right)\cos 90^{\circ} = \sin\left(\lambda_{SL} - \lambda_{AN}\right)\cot\varphi_{SL} - \sin 90^{\circ}\cot i$$

$$0 = \sin\left(\lambda_{SL} - \lambda_{AN}\right)\cot\varphi_{SL} - \cot i$$

$$\frac{1}{\tan i} = \sin\left(\lambda_{SL} - \lambda_{AN}\right)\frac{1}{\tan\varphi_{SL}}$$

and finally:

$$\tan\varphi_{SL} = \sin\left(\lambda_{SL} - \lambda_{AN}\right)\tan i \tag{4.5}$$

which relates the satellite relative longitude with the latitude considering the orbit inclination and the longitude of the ascending node.

Furthermore, other relation between the parameters of the geometry shown in Fig. 4.5 can be obtained. Considering the arc AN-SL that subtends an angle $u$ (known as the *nodal angular elongation*) and taking the spherical law of sines (4.1) in the same spherical triangle, the *nodal angular elongation* can be related with the satellite orbital parameters as:

$$\frac{\sin\varphi_{SL}}{\sin i} = \frac{\sin\left(\lambda_{SL} - \lambda_{AN}\right)}{\sin SL} = \frac{\sin u}{\sin 90^{\circ}}$$

$$\sin\varphi_{SL} = \sin i \sin u \tag{4.6}$$

Considering the spherical law of cosines (4.2):

$$\cos u = \cos\left(\lambda_{SL} - \lambda_{AN}\right)\cos\varphi_{SL} + \sin\left(\lambda_{SL} - \lambda_{AN}\right)\sin\varphi_{SL}\cos 90^{\circ}$$

where $a = u$, $b = \left(\lambda_{SL} - \lambda_{AN}\right)$, $c = \varphi_{SL}$ and $A = 90^{\circ}$ (angle at vertex $P$). This leads to:

$$\cos u = \cos\left(\lambda_{SL} - \lambda_{AN}\right)\cos\varphi_{SL} \tag{4.7}$$

Combining both (4.6) and (4.7), the following relation can be obtained:

$$\tan u = \frac{\sin u}{\cos u} = \frac{\sin\varphi_{SL} / \sin i}{\cos\left(\lambda_{SL} - \lambda_{AN}\right)\cos\varphi_{SL}} = \frac{\tan\varphi_{SL}}{\sin i\cos\left(\lambda_{SL} - \lambda_{AN}\right)} \cdot \frac{\sin\left(\lambda_{SL} - \lambda_{AN}\right)}{\sin\left(\lambda_{SL} - \lambda_{AN}\right)} =$$

$$= \frac{\tan\varphi_{SL}\tan\left(\lambda_{SL} - \lambda_{AN}\right)}{\sin i\sin\left(\lambda_{SL} - \lambda_{AN}\right)}$$

using (4.5) at the numerator:

$$\tan u = \frac{\sin\left(\lambda_{SL} - \lambda_{AN}\right)\tan i\tan\left(\lambda_{SL} - \lambda_{AN}\right)}{\sin i\sin\left(\lambda_{SL} - \lambda_{AN}\right)} = \frac{\tan\left(\lambda_{SL} - \lambda_{AN}\right)}{\cos i}$$

$$\tan\left(\lambda_{SL} - \lambda_{AN}\right) = \tan u\cos i \tag{4.8}$$

The point with highest latitude is called the vertex of the track. The longitude of this point is $\pi/2$ radians larger than the longitude of the ascending node: $\lambda_V = \lambda_{AN} + 90^{\circ}$.

Let's consider now a rotational earth reference system. To do that, a rotation of the reference meridian along time has to be taken into account. Being $\Delta t$ the time elapsed from the satellite pass through the reference meridian to the present time, the previous equations must be recomputed. The satellite cross through the perigee is usually taken as the reference time, so $\Delta t$ can be written as $\Delta t = t_p - t_0$, where $t_p$ is the time elapsed since the satellite passed the perigee and $t_0$ is the time of the initial position of the reference meridian computed from the passage through the perigee.

Then, the variation of the reference meridian position due to the earth rotation ($\Omega_E$) can be written as $\Delta\lambda = \Omega_E \Delta t = \Omega_E \left(t_p - t_0\right)$. This will change the relative longitude ($\lambda'$) of the satellite with respect this earth rotating reference system. Now, the satellite longitude with respect to the new reference will be $\lambda' = \lambda_{SL} - \Delta\lambda$. This new situation is shown in Fig. 4.6. So, it is possible to compute the satellite track in terms of the longitude and the latitude of the satellite.

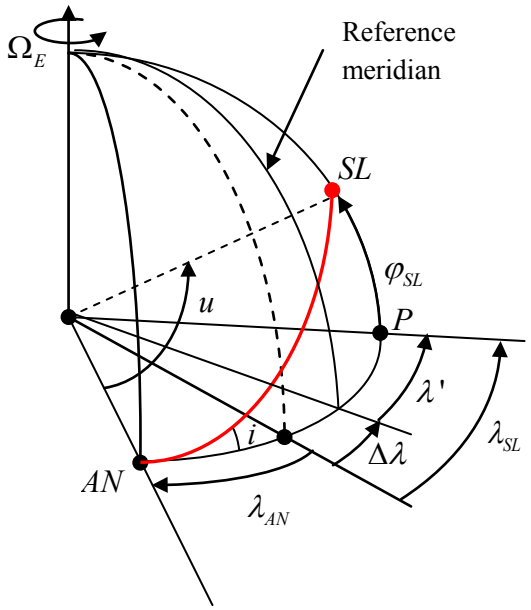


*Fig. 4.6 Satellite track in a rotating earth reference system*

### 4.2.1 Longitude of the satellite track

The longitude of the satellite track can be given with respect to the meridian of the ascending node. This is equivalent to consider the longitude of the ascending node ($\lambda_{AN}$) equals to zero. Considering that, equations (4.5), (4.7) and (4.8) will be:

$$\sin\lambda_{SL} = \frac{\tan\varphi_{SL}}{\tan i} \tag{4.9}$$

$$\cos\lambda_{SL} = \frac{\cos u}{\cos\varphi_{SL}} \tag{4.10}$$

$$\tan\lambda_{SL} = \tan u \cos i \tag{4.11}$$

So, the longitude of the satellite with respect to the meridian of the ascending node is obtained as follows:

$$\lambda' = \lambda_{SL} - \Delta\lambda = \arcsin\left(\frac{\tan\varphi_{SL}}{\tan i}\right) - \Delta\lambda \tag{4.12}$$

$$\lambda' = \lambda_{SL} - \Delta\lambda = \arccos\left(\frac{\cos u}{\cos\varphi_{SL}}\right) - \Delta\lambda \tag{4.13}$$

$$\lambda' = \lambda_{SL} - \Delta\lambda = \arctan\left(\tan u \cos i\right) - \Delta\lambda \tag{4.14}$$

Furthermore, the term $\Delta\lambda$ can be re-written considering the mean anomalies of the satellite and the ascending node. The mean anomaly ($M$) is defined as the true anomaly of a satellite in a circular orbit of the same period than the geosynchronous one in this analysis. This can be expressed as a function of the time with respect to the passage through the perigee as:

$$M = \frac{2\pi}{T}\left(t - t_p\right) = n\left(t - t_p\right) \tag{4.15}$$

being $n$ the mean movement or mean angular velocity of a satellite with period $T$. Then:

$$\Delta\lambda = \Omega_E\left(t_s - t_0\right) = \Omega_E\left(\frac{M_s}{n} - \frac{M_0}{n}\right) = \frac{\Omega_E}{n}\left(M_S - M_0\right) \tag{4.16}$$

For a geosynchronous satellite with the same period than the earth rotational period the mean movement ($n$) equals $\Omega_E$. Furthermore, the angle $u$ which is the angle between the ascending node and the position of the satellite can be computed as the addition of the argument of the perigee ($\omega$) and the true anomaly of the satellite ($\upsilon$). Another parameter that usually appears on the orbital analysis is the *eccentric anomaly* ($E$). This corresponds to the true anomaly of the satellite at the present time mapped to an equivalent circular orbit [10]. The *mean anomaly* is related with the *eccentric anomaly* by:

$$M = E - e\sin E \tag{4.17}$$

With the previous consideration and equations (4.16) and (4.17), the longitude of the satellite can be finally written as:

$$\lambda' = \arctan\left(\tan\left(\omega + \upsilon\right)\cos i\right) - \left(E - e\sin E\right) + \left(E_0 - e\sin E_0\right) \tag{4.18}$$

For quasi-circular ($e \ll 1$) and non-inclined ($i < 1^{\circ}$) orbits, the satellite relative longitude with respect the nominal satellite longitude can be approximated as in (4.19) [6]. The validity of the approximation can be checked in Fig. 4.7. In Fig. 4.7 a), the approximated and the exact longitude histories for an eccentricity of $10^{-4}$ are shown. In this case, the two functions have the same behaviour. Increasing the orbit eccentricity, as in Fig. 4.7 b), up to $e = 10^{-1}$, slightly differences can be observed. However, higher eccentricities are not

expected in the geosynchronous satellites orbits. Then, (4.19) can be taken as a reasonable approximation for the satellite longitude in the geosynchronous case.

$$\Delta\lambda = 2e\sin\left(\Omega_E\left(t-t_p\right)\right) \tag{4.19}$$

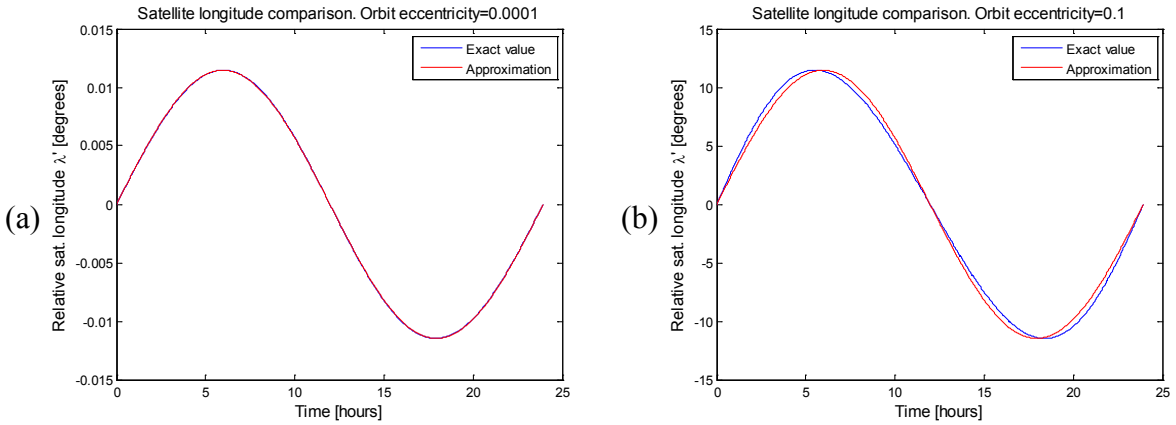


*Fig. 4.7 Satellite relative longitude evolution approximation. a) Considering an orbit eccentricity of 0.0001 and b) 0.1*

### 4.2.2 Latitude of the satellite track

From the previous equations, the latitude of the satellite at any time can be also computed. In this case, the latitude is not affected by the earth rotation and consequently, it does not depend on the choice of the origin position or reference meridian as in the longitude case. From (4.6), the satellite latitude can be written as:

$$\varphi_{SL} = \arcsin\left(\sin i \sin u\right) = \arcsin\left(\sin i \sin\left(\omega+\upsilon\right)\right) \tag{4.20}$$

Once again, considering the geosynchronous case with small inclinations of the orbit, the *arcsin* function can be approximated by its argument while the $\sin i \approx i$. Therefore, the satellite latitude can be approximated as:

$$\varphi_{SL} = i\sin\left(\omega+\Omega_E\left(t-t_p\right)\right) \tag{4.21}$$

where the time across the perigee has been taken as a time reference like in longitude computation in (4.19).

## *4.3 Satellite distance from a point over the Earth's surface*

One of the key parameters of any radar system is the distance to the illuminated targets. It will be important to identify the source of the received echoes as well as to compute the power budget of Chapter 7. The distance from the satellite to a target located at coordinates ( $\lambda_T$ , $\varphi_T$ ) over the earth will depend on the satellite coordinates ( $\lambda_{SL}$ , $\varphi_{SL}$ ) and

the geographical height ( $h_T$ ) of the point over the earth reference ellipsoid. The geometry for this analysis is shown in Fig. 4.8.

The satellite latitude in Fig. 4.8 is given by the centre angle $\widehat{NaOA}$, where *Na* is the sub-satellite point (or nadir) and the centre angle $\widehat{TOB}$ corresponds to the target latitude. Another important parameter to take into account in the distance computation is the relative longitude between the satellite and the target. This angle, called $L = \lambda_T - \lambda_{SL}$, is defined by $\widehat{AOB}$.

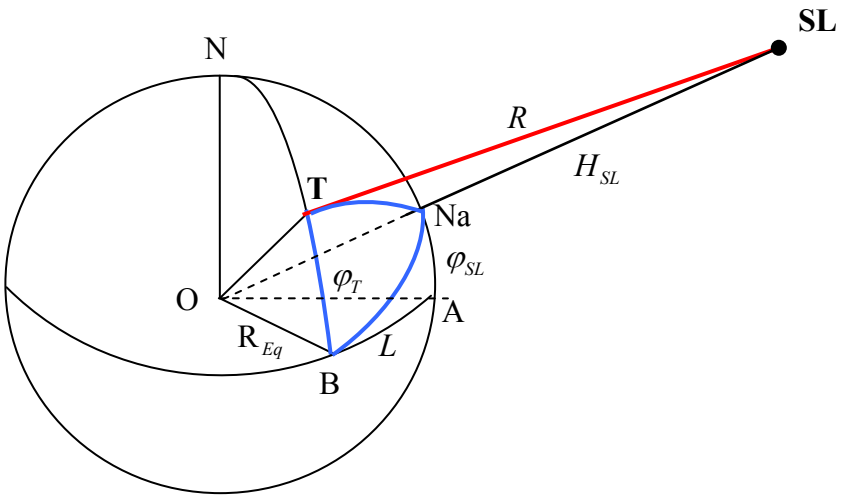


*Fig. 4.8 Earth-satellite geometry*

To compute the distance between the satellite and the target (known in radar as *range*), the triangle with vertexes O-T-SL is used. The side $\overline{OT}$ which corresponds to the position of the target over the Earth's surface can be taken as the result of the local Earth's radius at that latitude plus the ellipsoidal height ( $h_T$ ) of the considered target. The side $\overline{OSL}$ corresponds to the satellite distance from the Earth's centre. This can be obtained from the orbit analysis of the geosynchronous case with the two body problem (3.1) and corresponds to the addition of the local Earth's radius at the nadir point and the satellite height over the nadir. Finally, the side $\overline{TSL}$ is the distance between the satellite and the desired target which is the goal of this section.

In order to obtain more precise results, on this analysis an ellipsoidal reference earth model has been considered. The WGS84 [11] models the earth as an ellipsoid with a semi-major axis (equatorial radius) of 6378,137 Km and a semi-minor axis (polar radius) of 6356,752 Km, as in Fig. 4.9. Considering this model, the Earth's radius at arbitrary latitude $\varphi$ can be easily obtained from the ellipse's formula as:

$$R_{ET}(\varphi_C) = \left( \frac{\cos^2 \varphi_C}{R_{Eq}} + \frac{\sin^2 \varphi_C}{R_{Pol}} \right)^{-1/2} \tag{4.22}$$

where $\varphi_C$ is the geocentric latitude which is related with the geographical one ($\varphi$) by:

$$\tan\varphi_C = \frac{R_{Pol}^{\ 2}}{R_{Eq}^{\ 2}}\tan\varphi \tag{4.23}$$

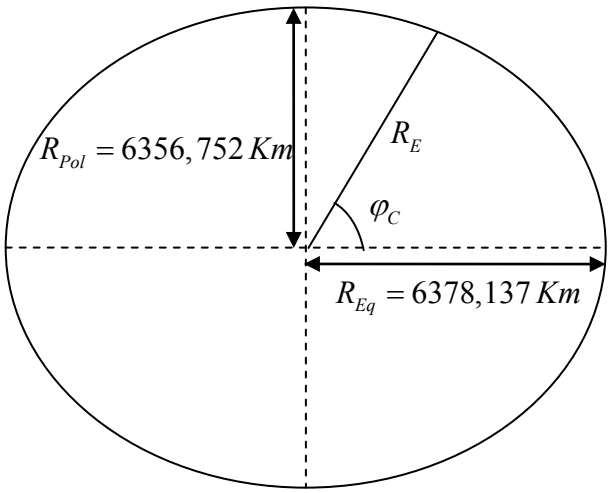


*Fig. 4.9 WGS84 reference earth model*

Taking this consideration into account, the distance between the satellite (SL) and the target (T) can be obtained using the linear cosine law on the O-T-SL triangle. Then, the following equation is obtained:

$$R_{SL-T} = \sqrt{\left(R_{ET} + h_T\right)^2 + r^2 - 2\left(R_{ET} + h_T\right) r\cos\phi} \tag{4.24}$$

where $R_{ET}$ is the local Earth's radius at the target latitude, $h_T$ is the target height over the reference ellipsoid, $r$ is the orbital radius of the satellite and $\phi$ is the angle $\widehat{TONa}$ in Fig. 4.8. This angle can be obtained from the spherical triangle Na-T-B highlighted in blue in Fig. 4.10 and Na-A-B by using the spherical sine (4.1) and cosine laws (4.2). From spherical cosine law, $\cos\phi$ can be written as:

$$\cos\phi = \cos\varphi_T\cos\xi + \sin\varphi_T\sin\xi\cos\widehat{TBNa} \tag{4.25}$$

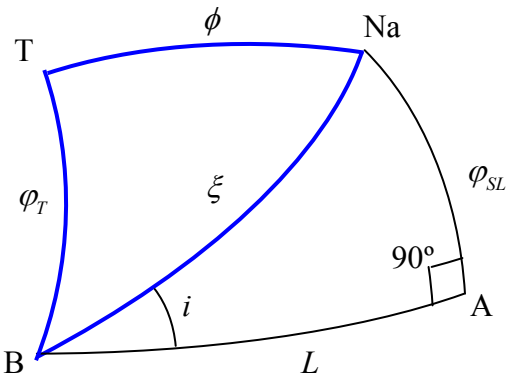


*Fig. 4.10 Slant range computation*

The $\sin\xi$ and $\cos\xi$ can be obtained from the sine and cosine spherical laws applied on the triangle B-A-Na as in (4.26) and (4.27). On the other hand, $\widehat{TBNa} = \pi/2 - i$ and, therefore, $\cos\widehat{TBNa} = \cos(\pi/2 - i) = \sin i$. Then, combining the results obtained in (4.26) and (4.27) with equation (4.25), the expression obtained for $\cos\phi$ is shown in (4.28).

$$\frac{\sin\widehat{NaAB}}{\sin\xi} = \frac{\sin i}{\sin\varphi_{SL}} \rightarrow \sin\xi = \frac{\sin 90^\circ \sin\varphi_{SL}}{\sin i} = \frac{\sin\varphi_{SL}}{\sin i} \tag{4.26}$$

$$\begin{aligned} \cos\xi &= \cos\varphi_{SL}\cos L + \sin\varphi_{SL}\sin L\cos\widehat{NaAB} = \\ &= \cos\varphi_{SL}\cos L + \sin\varphi_{SL}\sin L\cancelto{0}{\cos 90^\circ} = \cos\varphi_{SL}\cos L \end{aligned} \tag{4.27}$$

$$\begin{aligned} \cos\phi &= \cos\varphi_T\cos\varphi_{SL}\cos L + \sin\varphi_T\frac{\sin\varphi_{SL}}{\cancel{\sin i}}\cancel{\sin i} = \\ &= \cos\varphi_T\cos\varphi_{SL}\cos L + \sin\varphi_T\sin\varphi_{SL} \end{aligned} \tag{4.28}$$

Using this result in (4.24), the target-satellite range can be computed as:

$$R_{SL-T} = \sqrt{(R_{ET}+h_T)^2 + r^2 - 2(R_{ET}+h_T)r(\cos\varphi_T\cos\varphi_{SL}\cos L + \sin\varphi_T\sin\varphi_{SL})} \tag{4.29}$$

In the geosynchronous satellite case, considering the slight variations in the longitude and latitude of the satellite due to the orbit small inclinations and eccentricities, the slant range will change along the orbit accordingly to the satellite coordinates evolution presented in (4.19) and (4.21). Besides, the small eccentricity of the orbit will cause variations on the orbit radius $r$ (3.1) which will increase the fluctuations in the satellite-target distance. The parameters referred to the point target ($\varphi_T$, $\lambda_T$, $h_T$) are fixed since a still point over the Earth's surface is considered.

This phenomenon has been simulated and the results can be observed in Fig. 4.11. For this simulation a satellite placed on a geosynchronous orbit with coordinates 0º N and 30º W has been chosen (HISPASAT-1D). The orbit eccentricity has set up to $4\cdot10^{-4}$ and an orbit

inclination to 0.05º. As a target, a point situated in Barcelona (41.23º N, 2.11º E) is considered. A target height of 450 meters (approximately the geographical height of Collserola communication tower) has been considered. This points has been taken since it is expected to be always visible for the satellite without shadowing and/or multipath propagation interferences.

The slant range obtained varies from 38442,6 Km to 38400,9 Km as it is plotted in Fig. 4.11 a). Furthermore, in Fig. 4.11 b), the hodograph is presented. It corresponds to the range variations relative to the closest distance. As it can be seen, a variation of 42 Km is obtained so a precise estimation of the satellite-target range considering all the features presented in this section has to be performed in order to get reliable results and process correctly the received echoes to focus the image.

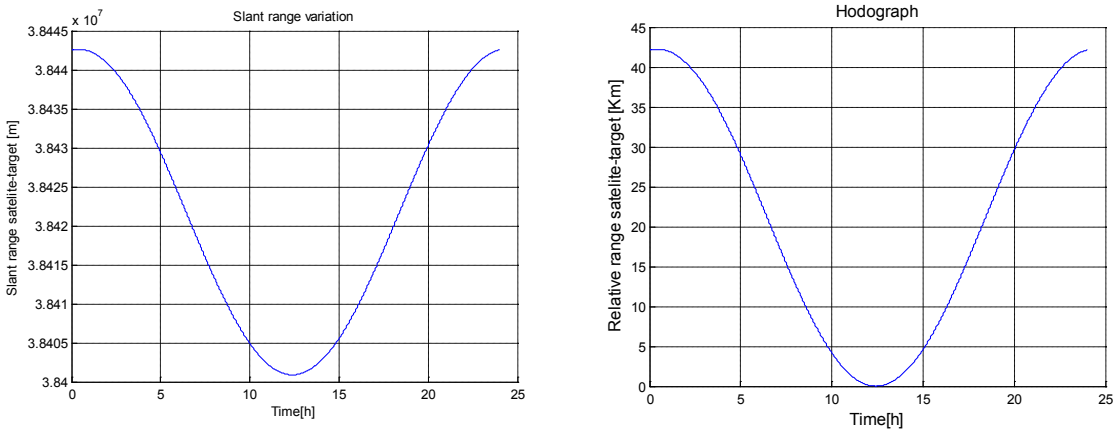


*Fig. 4.11 Slant range variations due to orbit perturbations. a) Absolute satellite-target range. b) Hodograph relative to the minimum slant range*

## *4.4 Satellite location. Elevation and azimuth angles*

From a point of view of a target situated at a point T, the satellite is seen on the sky in a fixed zone with slightly variations produced due to the relative motion of the non-prefect geostationary orbit of the satellite. In order to define the location of the satellite two angles are necessary and the most widely used are the elevation and azimuth angles. The satellite motion in the sky is usually called *analema* of the satellite.

### 4.4.1 Elevation angle

The elevation angle is defined as the angle between the horizon at the point where the target is placed and the direction of the satellite measured in the plane that contains the satellite, the centre of the earth and the considered target. In Fig. 4.12, the triangle O-T-SL of Fig. 4.8 is represented in the corresponding plane of interest. The elevation angle, called $\theta_{el}$, can be computed using the right triangle O-T'-SL shown in Fig. 4.12.

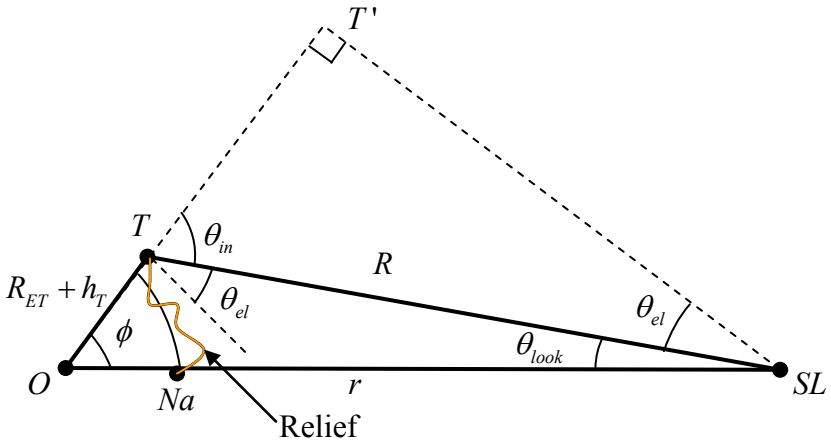


*Fig. 4.12 Satellite location in the sky. Elevation angle computation*

The angle $\widehat{T'TSL}$ in Fig. 4.12 is equal to $\pi/2-\theta_{el}$. Since the angles of the triangle T-T'-SL must add up to $\pi$ radians, the angle $\widehat{TSLT'}=\pi-(\pi/2-\theta_{el})-\pi/2=\theta_{el}$. Then, using planar trigonometry, the elevation angle can be obtained as:

$$\cos\theta_{el}=\frac{\overline{T'SL}}{R} \tag{4.30}$$

where the segment $\overline{T'SL}$ can be obtained from the triangle O-T'-SL as:

$$\sin\phi=\frac{\overline{T'SL}}{r} \tag{4.31}$$

Therefore, the elevation angle is computed with (4.32). The $\sin\phi$ can be easily found from (4.28) knowing that $\sin\phi=\sqrt{1-\cos^2\phi}$.

$$\theta_{el}=\arccos\left(\sin\phi\frac{r}{R}\right) \tag{4.32}$$

Similarly, the elevation angle can also be calculated considering the sinus of the angle $\widehat{TSLT'}$. The analysis is presented next:

$$\sin\theta_{el}=\frac{\overline{T'T}}{R} \tag{4.33}$$

and

$$\cos\phi=\frac{(R_{ET}+h_T)+\overline{T'T}}{r}\rightarrow\overline{T'T}=r\cos\phi-(R_{ET}+h_T) \tag{4.34}$$

Using (4.34) in (4.33), another way to obtain the elevation angle is the following:

$$\theta_{el} = \arcsin\left(\frac{\cos\phi - \left(R_{ET} + h_T\right)/r}{R/r}\right) \tag{4.35}$$

Finally, taking the results of equations (4.32) and (4.35), the elevation angle is given in terms of the tangent as:

$$\tan\theta_{el} = \frac{\sin\theta_{el}}{\cos\theta_{el}} = \frac{\dfrac{\cos\phi - \left(R_{ET} + h_T\right)/r}{\cancel{R/r}}}{\dfrac{\sin\phi}{\cancel{R/r}}} = \frac{\cos\phi - \left(R_{ET} + h_T\right)/r}{\sin\phi}$$

$$\theta_{el} = \arctan\left(\frac{\cos\phi - \left(R_{ET} + h_T\right)/r}{\sin\phi}\right) \tag{4.36}$$

### 4.4.2 Azimuth angle

The other angle necessary to univocally locate the satellite is the azimuth angle. This angle is measured in the horizontal plane of the target between the direction of the geographic north and the direction to the nadir point over the Earth's surface. It corresponds to the spherical angle $\widehat{NTNa}$ in Fig. 4.8. The azimuth angle takes values from 0 to 360 degrees depending on the orientation of the satellite with respect to the target considered. Using the spherical law of sinus in the spherical triangle N-Na-T, (4.37) is obtained.

$$\frac{\sin\widehat{NTNa}}{\sin\left(\pi/2 - \varphi_{SL}\right)} = \frac{\sin\widehat{TNNa}}{\sin\phi} \tag{4.37}$$

As it can be seen in Fig. 4.8, the angle $\widehat{TNNa}$ is equal to $\widehat{BNA}$. This angle can be obtained from the spherical triangle N-B-A as:

$$\frac{\sin\widehat{BNA}}{\sin L} = \frac{\sin\widehat{BAN}}{\sin\widehat{BON}} = 1 \tag{4.38}$$

since $\widehat{BAN} = \widehat{BON} = 90º$. Then, the angle $\widehat{NTNa}$ which will be called $a$ from now on for simplicity, can be re-written as:

$$a = \arcsin\left(\frac{\sin\widehat{TNNa}}{\sin\phi}\sin\left(\pi/2 - \varphi_{SL}\right)\right) = \arcsin\left(\frac{\sin L}{\sin\phi}\cos\left(\varphi_{SL}\right)\right) \tag{4.39}$$

The angle $a$ computed with (4.39) always gives an angle between 0 and 90 degrees. Since the azimuth angle can be up to 360 degrees, a transformation will be necessary to obtain the final value of the azimuth angle. So, after computing the angle $a$, the azimuth angle ($\theta_{az}$) will be obtained taking into account the relative position of the nadir point with respect to the target location.

The four possible situations are represented in Fig. 4.13. The black dot represents the location of the target while the red one marks the position of the sub-satellite point or nadir. As it can be seen, depending on the position of the nadir point with respect to the target, the azimuth angle ($\theta_{az}$) is computed in one way or another from $a$. The formulas required to obtained the azimuth angle are summarized in Table 4.1.

| **Sub-satellite point (*Na*) with respect to the target (*T*)** | **Relation between $\theta_{az}$ and $a$ (radians)** | **Relation between $\theta_{az}$ and $a$ (degrees)** |
|---|---|---|
| North-West | $\theta_{az} = 2\pi - a$ | $\theta_{az} = 360^{o} - a$ |
| North-East | $\theta_{az} = a$ | $\theta_{az} = a$ |
| South-West | $\theta_{az} = \pi + a$ | $\theta_{az} = 180^{o} + a$ |
| South-East | $\theta_{az} = \pi - a$ | $\theta_{az} = 180^{o} - a$ |

*Table 4.1 Azimuth angle computation depending on the satellite-target position*

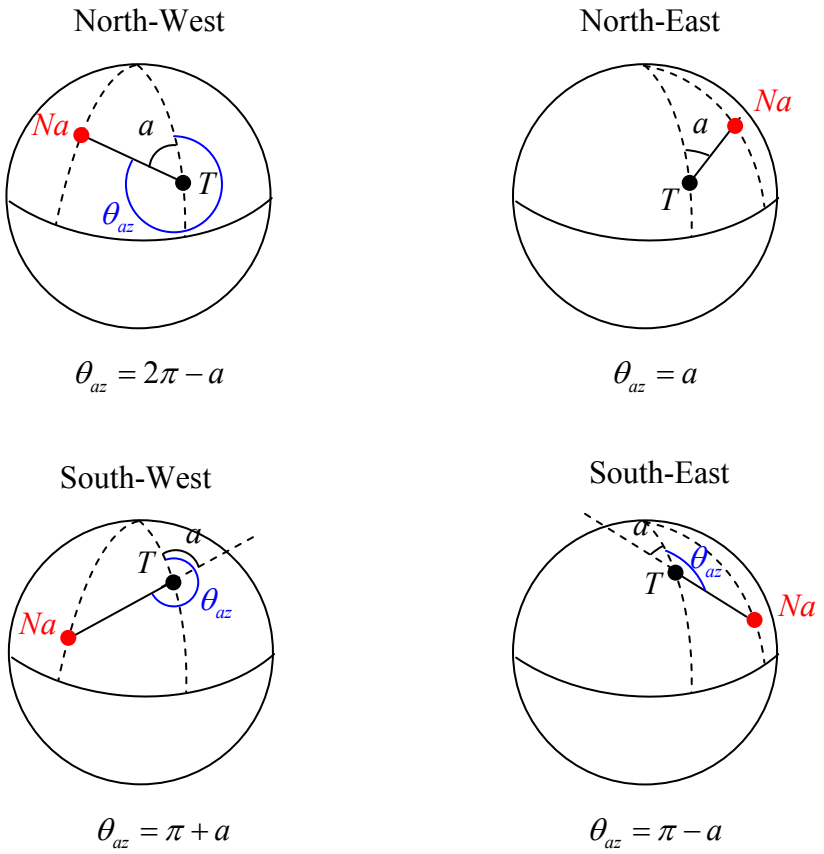


*Fig. 4.13 Determination of the azimuth angle*

The behaviour of the relative motion of the satellite has been introduced in section 2.1, where the satellite longitude and latitude variations have been compared for different orbit configurations. Now that the satellite location has been characterized, the motion seen from the point of view of the targets in the Earth's surface can be better understood with the azimuth and elevation angles. Just as an example, continuing with the scenario presented in the previous section where a satellite with co-ordinates 0ºN and 30ºW and a point target near to Barcelona (41.23ºN, 2.11ºE) with a height of 450 meters were considered, the satellite *analemma* (or the figure described in the sky by the satellite) has been simulated.

In Fig. 4.14, the situation is presented. As it is shown in Fig. 4.14 a), the satellite describes an ellipse if a target-centred reference system is considered. It means that the satellites movement on the sky is seen as an ellipse from the target point of view. The azimuth and elevation angles change all along the satellite orbital evolution. These variations are plotted in Fig. 4.14 b) for the parameters presented in the previous paragraph. This figure on the sky is periodically repeated every day given the daily periodicity of the geosynchronous satellites.

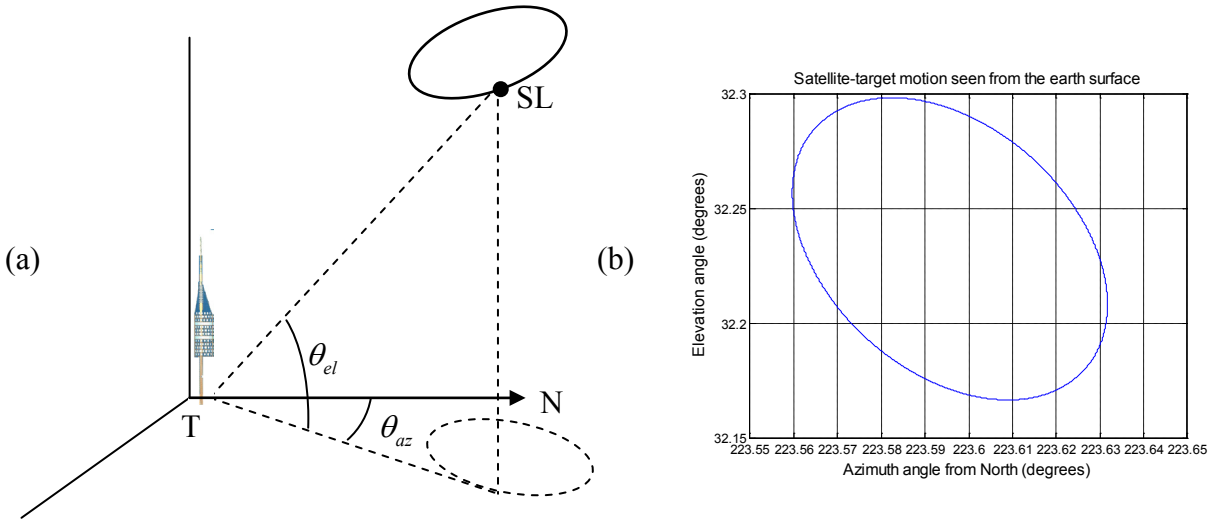


*Fig. 4.14 Elevation and azimuth angles evolution. a) Changes seen from a target-centred reference system. b) Satellite (0ºN, 30W) and target (41.23N, 2.11E) example.*

## *4.5 Target location. Look and incidence angles*

Equivalently, the situation can be discussed from a point of view of the satellite. Then, a target over the surface is seen by the satellite in a determined position. The relative location of the target seen from the satellite will be defined by the look angle. Usually, the results are given in function of the incidence angle which will be defined in this section as well.

### 4.5.1 Look Angle

The look angle is defined as the angle between the nadir direction, perpendicular to the Earth's surface, and the direction of the illuminated target. This angle, called $\theta_{look}$, corresponds to the angle $\widehat{TSLO}$ in Fig. 4.12. The look angle is also known as the nadir angle. From the cosine law in the triangle T-SL-O:

$$\left(R_{ET}+h_T\right)^2 = r^2 + R^2 - 2rR\cos\theta_{look} \tag{4.40}$$

where the look angle can be computed as:

$$\theta_{look} = \arccos\left(\frac{r^2 + R^2 - \left(R_{ET}+h_T\right)^2}{2rR}\right) \tag{4.41}$$

In the geosynchronous case, the range of possible look angles will be really low, since the earth is so far away from the antenna. Then, it only takes up a little area in the whole visible space by the satellite. The maximum look angle is presented in Fig. 4.15. As it can be seen, the maximum look angle is obtained when the incoming beam from the satellite is tangent to the Earth's surface. It means that the angle between the incoming beam and the Earth's radius at this point is a right angle. Then, from the law of sinus, the maximum look angle can be obtained easily as:

$$\frac{\sin\theta_{look\max}}{R_{Pol}+h_T} = \frac{\sin 90^\circ}{r} \rightarrow \theta_{look\max} = \arcsin\left(\frac{R_{Pol}+h_T}{r}\right) \tag{4.42}$$

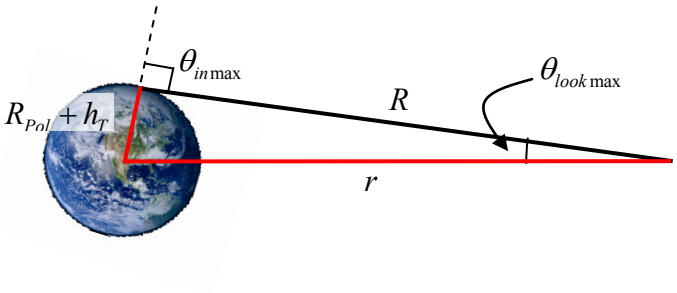


*Fig. 4.15 Maximum look angle. In the geosynchronous case, only a small range of look angles are allowed*

Using the typical values of a geosynchronous satellite with a orbit radius of 42164 Km and considering an Earth's radius approximately at the poles with a target at 0 meters height, a maximum look angle of 8.7 degrees is obtained. So, the range of possible look angles will go from 0 to 8.7 degrees, a small range in the whole space seen by the satellite. However, it would not be a problem for target location since targets are located according to range/Doppler history which do not depend on the antenna pointing misalignments. The antenna pointing determines the swath accessed and Doppler centroid which are important for SAR processing.

### 4.5.2 Incidence angle

Another way to express the position of the target with respect to the satellite is the incidence angle. This angle is related with the look angle so it does not provide any further information, but it is widely used in most of the SAR analysis and most of the results are given in terms of this angle.

The incidence angle is the angle between the direction of the incoming satellite illumination and the direction perpendicular to the incidence plane which is the plane tangent to the Earth's sphere at the target location. It corresponds to the angle $\widehat{T'TSL}$ in Fig. 4.12 where is indicated by $\theta_{in}$. The incidence angle can be obtained directly from the elevation angle as:

$$\theta_{in} = \frac{\pi}{2} - \theta_{el} \tag{4.43}$$

However, it will only be valid for a flat surface. The actual incidence angle should take into account the slopes or local topography of the imaged scene. On the other hand, it can also be obtained from the look angle. Using the law of sinus in triangle O-T-SL in Fig. 4.12:

$$\frac{\sin\theta_{look}}{R_{ET}+h_T} = \frac{\sin(\pi-\theta_{in})}{r} = \frac{\sin\theta_{in}}{r} \rightarrow \theta_{in} = \arcsin\left(\sin\theta_{look}\frac{r}{R_{ET}+h_T}\right) \tag{4.44}$$

In this case, the range of possible incidence angles for the geosynchronous case will vary from 0 degrees, corresponding to the nadir direction, to 90 degrees when the illumination is tangent to the Earth's surface. This maximum value can be seen in Fig. 4.15 corresponding to the maximum look angle. Other way to compute this value is using directly the expression (4.44) with the maximum look angle (4.42). The result in (4.45) is obtained.

$$\theta_{in\_\max} = \arcsin\left(\frac{R_{Pol}+h_T}{r}\frac{r}{R_{Pol}+h_T}\right) = \arcsin(1) = 90^{\circ} \tag{4.45}$$

## *4.6 Satellite coverage*

Another important parameter to take into account in the SAR design is the desired ground coverage or swath. This parameter is the ground patch that the radar is illuminating for a given look angle. Then, the swath will depend on the look angle at which the antenna is pointing and the antenna beamwidth considered. The analysed situation for a generic case is presented in Fig. 4.16.

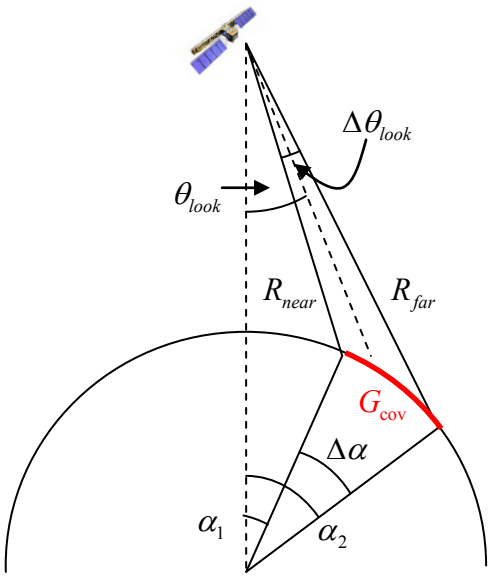


*Fig. 4.16 Ground coverage of the satellite*

Looking at the geometric parameters in Fig. 4.16, the ground coverage ($G_{cov}$) can be obtained from the inner angles $\alpha_1$ and $\alpha_2$ as:

$$G_{cov} = \Delta\alpha \cdot R_{ET} = (\alpha_2 - \alpha_1) R_{ET} \tag{4.46}$$

being $R_{ET}$ the local Earth's radius for the illuminated area. The inner angles $\alpha_1$ and $\alpha_2$ are obtained using the law of sinus:

$$\alpha_1 = \arcsin\left(\sin\theta_{look\_near}\frac{R_{near}}{R_{ET}}\right) \tag{4.47}$$

$$\alpha_2 = \arcsin\left(\sin\theta_{look\_far}\frac{R_{far}}{R_{ET}}\right) \tag{4.48}$$

where $R_{near}$ stands for the range to the nearest point illuminated by the satellite while $R_{far}$ corresponds to the furthest one. Similarly, the $\theta_{look\_near}$ and $\theta_{look\_far}$ are the look angle at which the nearest target is seen and the furthest one respectively. These angles can be easily obtained from the middle look angle and the beamwidth ($\Delta\theta_{look}$):

$$\theta_{look\_near} = \theta_{look} - \frac{\Delta\theta_{look}}{2} \tag{4.49}$$

$$\theta_{look\_far} = \theta_{look} + \frac{\Delta\theta_{look}}{2} \tag{4.50}$$

Finally, the near and far slant range can be computed from the look angles solving the second degree equations derived from the law of cosines (4.51) and (4.52). In those equations, $r$ is the orbit radius while the look angles near and far corresponds to the ones computed in (4.49) and (4.50). Thus, the ground coverage can be computed from the look angle and the antenna beamwidth since all the necessary parameters are given in terms of them.

$$R_{near}{}^2 - 2r\cos\theta_{look\_near}R_{near} = R_{ET}{}^2 - r^2 \tag{4.51}$$

$$R_{far}{}^2 - 2r\cos\theta_{look\_far}R_{far} = R_{ET}{}^2 - r^2 \tag{4.52}$$

As an example to see which values will be obtained in the geosynchronous case, a look angle of 5 degrees has been considered and different antenna beamwidth have been tried. The results are shown in Table 4.2. As it can be seen, slight variation of the antenna beamwidth will provide a wide range of ground coverage or swath widths which can be really interesting depending on the acquisition purposes and applications of the system.

| $\Delta\theta_{look}$ [degrees] | $\theta_{look\ near}$ [degrees] | $\theta_{look\ far}$ [degrees] | $R_{near}$ [Km] | $R_{far}$ [Km] | $\Delta\alpha$ [degrees] | $G_{\text{cov}}$ [Km] |
|---|---|---|---|---|---|---|
| 0.15 | 4.925 | 5.075 | 36772 | 36840 | 0.0185 | 118.01 |
| 0.3 | 4.85 | 5.15 | 36739 | 36875 | 0.0371 | 236.05 |
| 0.5 | 4.75 | 5.25 | 36696 | 36923 | 0.0618 | 393.57 |
| 1.0 | 4 | 6 | 36595 | 37051 | 0.1239 | 788.53 |

*Table 4.2 Ground coverage considering several antenna beamwidth at 5 degrees of look angle*

On the other way around, sometimes it can be useful to obtain the necessary antenna beamwidth to reach a desired swath width or coverage at a given middle look angle. Looking at the previous equation, the isolation of the antenna beamwidth is really complicated and it can not be solved by linear algebra. Thus, a reasonable approximation must be taken in order to obtain the required beamwidth. To do that, the Earth's surface in Fig. 4.16 can be considered locally flat. The new geometry is presented in Fig. 4.17. As it can be seen, the ground coverage can be approximated as:

$$\overline{G_{\text{cov}}} = \frac{\Delta\theta_{look}R}{\cos\theta_{in}} \tag{4.53}$$

where $R$ is the slant range at the middle look angle and $\theta_{in}$ corresponds to the incidence angle at this look angle, obtained from (4.44). So, the necessary look angle beamwidth can be obtained from the desired swath as:

$$\Delta\theta_{look} = \frac{\overline{G_{\text{cov}}}\cos\theta_{in}}{R} \tag{4.54}$$

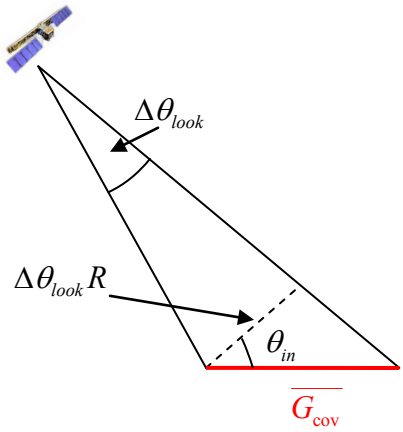


*Fig. 4.17 Ground coverage of the satellite*

To check the validity of the approximation presented in (4.54), some numbers are shown in Table 4.3 considering several swath widths. The values presented have been computed taking a middle look angle of 5 degrees. This corresponds to an incidence angle of 35.26 degrees and a middle slant range of 36805 Km.

As it can be seen, the values calculated with the approximation are close to the required values. The error increases with the width of the swath but, even in the worst case considered, it is not greater than a one per cent. In SAR application, swaths of some hundred kilometres are usually considered, but never larger than the values considered in Table 4.3 since problems of timing and PRF selection could appear.

| **Desired** $G_{cov}$ [Km] | **Required** $\Delta\theta_{look}$ [degrees] | **Actual** $G_{cov}$ [Km] | **Swath width relative error (%)** |
|---|---|---|---|
| 100 | 0.1271 | 100.00 | 0.0038 |
| 200 | 0.2542 | 200.03 | 0.0151 |
| 300 | 0.3814 | 300.10 | 0.0339 |
| 500 | 0.6356 | 500.47 | 0.0943 |
| 1000 | 1.2712 | 1003.81 | 0.3810 |
| 1500 | 1.9067 | 1513.07 | 0.8716 |

*Table 4.3 Antenna beamwidth required considering several ground coverage at 5 degrees of look angle*

# Chapter 5 The Synthetic Aperture, timing and SAR features

A critical feature of the Geosynchronous geometry to determine the feasibility of the system into SAR applications is the formation of the Synthetic Aperture. As it has been introduced in Chapter 2 and Chapter 3, the non-perfect geostationary orbit due to non-zero inclinations and small eccentricities can be used to perform a kind of Synthetic Aperture. In this section, the relative motion between the target and the satellite will be used to characterize the synthetic aperture for these systems. Furthermore, the timing restrictions will be also explained and particularised to geostationary case. The PRF selection with the corresponding diamond and dartboard diagrams will also be presented. Integration time requirements, azimuth resolution achieved, ambiguity computation and other SAR merit figures are given in this section as well.

## *5.1 The Synthetic Aperture on a Geosynchronous system*

The length of the Synthetic Aperture achieved with a geosynchronous satellite will be determined by the relative motion between the platform and the scene considered. As it has been explained in section 4.2.1 and 4.2.2, the satellite longitude and latitude with respect to a rotating Earth coordinate system can be described by (4.19) and (4.21), respectively. The combination of both will determine the length of the Synthetic Aperture.

In the geosynchronous case, the definition of azimuth and range direction is not as obvious as in a LEO system, where the along track and cross-track direction are well defined. In a geosynchronous satellite with a nearly fixed position of the satellite, the along and cross-track direction will depend on the time of the day considered. This phenomenon is shown in Fig. 5.1. The red square stands for the zone of interest illuminated by the radar (Europe in this example).

The slashed green line represents the common LEO quasi-polar satellite track. Only some tracks have been plotted in Fig. 5.1 for simplicity, but the behaviour is periodically repeated all over the Earth's surface. Furthermore, the ascending and descending tracks should be considered as well, but a similar behaviour should be obtained. However, the zone of interest will be only visible for the satellite for a short time during all the satellite orbit. As it can be seen, for those satellites, the along-track (azimuth) and cross-track (range) directions are well defined in the scene. They do not depend on the time considered. On the other hand, the slashed blue line represents the typical behaviour of a satellite track in a Geosynchronous orbit. The satellite track is periodically repeated every day. Consequently, continuous monitoring of the zone of interest is achieved. The longitude and latitude history described in (4.19) and (4.21) will have a similar behaviour than in Fig. 5.1 in the GEO track ( $\Delta\lambda_{SL}$ and $\varphi_{SL}$, respectively). In this case, depending on the acquisition time considered to form the Synthetic Aperture, the along track direction will change. It is shown in Fig. 5.1 with the orange and white arrows which define the along-track direction at two different acquisition times. The cross-track directions have not been plotted in order not to hinder the understanding of the rest of the picture.

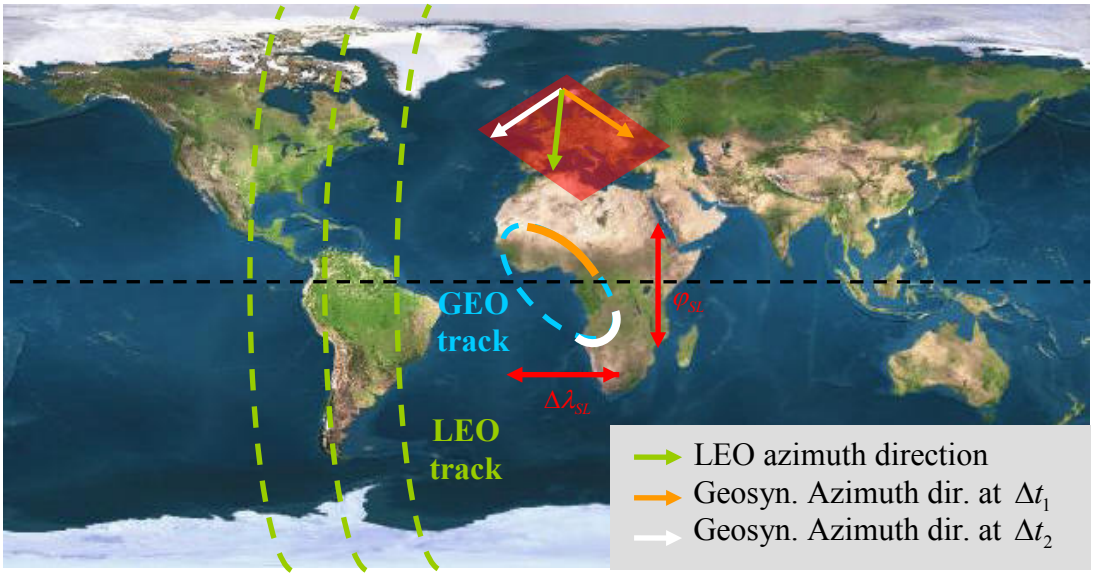


*Fig. 5.1 Along-track (azimuth) direction in Geosynchronous vs. LEO satellites*

Then, several lengths and directions of the synthetic aperture can be achieved by playing with the duration of the acquisition and the instant when it is started. The maximum synthetic aperture length will be given by the semi-major axis of the ellipsoidal track described by the satellite and the relative position between the satellite and the zone of interest. Let's consider some basic situations to see some preliminary results achieved with the Geosynchronous SAR configuration.

As a first approximation, let's take a simple case with a Geosynchronous satellite with only slightly perturbations in the eccentricity and zero-inclination. In Fig. 5.2, the satellite track is plotted as a red line. As it can be seen, some variations from the satellite reference meridian are observed while the latitude is kept constant over the Equator. A swath over south Europe (yellow strip) at the same longitude than the satellite is considered. In Fig. 5.2, the unique north-south illumination typical of those satellites can be appreciated. It is a new feature of the Geosynchronous SAR systems complementary to the LEO satellites which have East-West illumination.

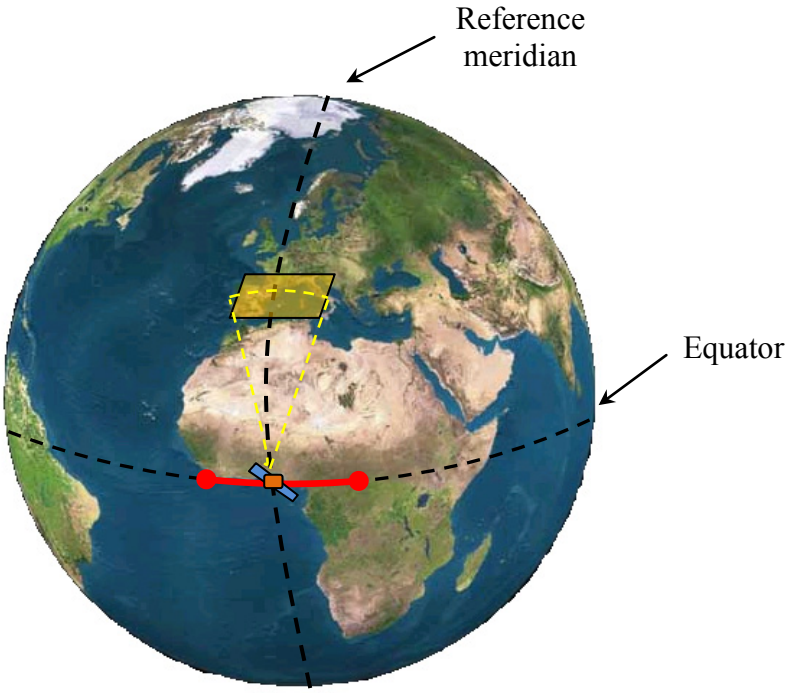


*Fig. 5.2 Geosynchronous satellite track considering small eccentricity in the orbit and zero-inclination*

So, taking the expression obtained in (4.19), the length of the synthetic aperture is computed as the angle variation (longitude in this case) multiplied by the distance of the satellite from the Earth's centre (mean orbit radius). Considering the maximum longitude variation (4e), the maximum length of the synthetic aperture can be approximately obtained as:

$$L_{SA_{\max}} = r \cdot \Delta\lambda_{\max} = 4\, r \cdot e \tag{5.1}$$

Taking a zero-inclined orbit with low eccentricity (0.0004) and the mean radius of a geosynchronous satellite (42.164,17 Km) a synthetic aperture length of 67.5 Km can be achieved. This example has been simulated using the GeoSAR Simulator presented in section 8.3 of this report. This tool has been implemented in Matlab and will be used in the following section to present graphical information and corroborate the theoretical results computed with the common SAR formulas. Then, considering the satellite ephemerides presented above (inclination 0º, eccentricity 0.0004, nominal longitude of 0 degrees), the orbital behaviour obtained is presented in Fig. 5.3 and Fig. 5.4.

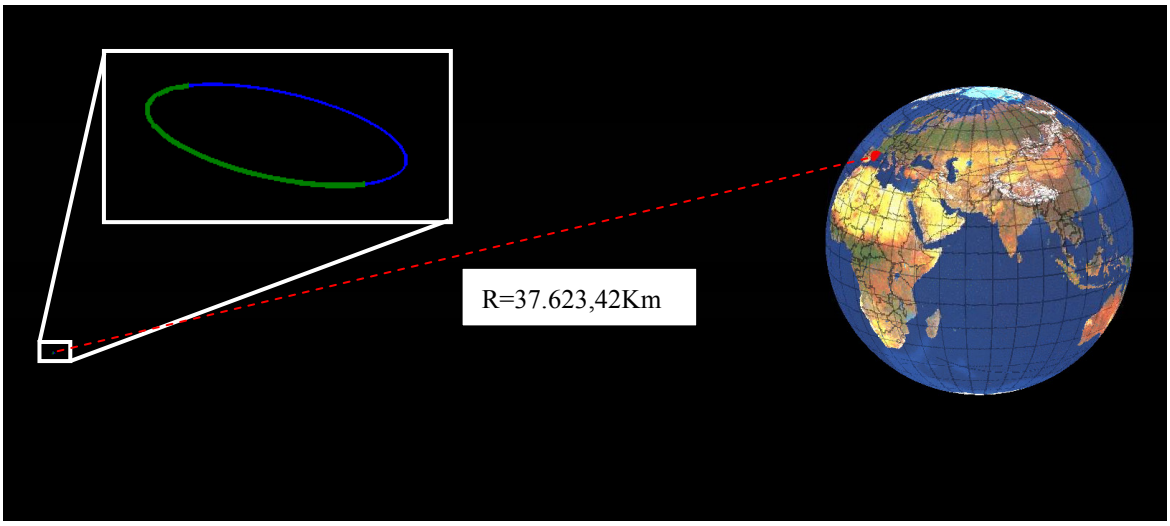


*Fig. 5.3 3D satellite orbit representation considering a non-inclined orbit with eccentricity of 0.0004 and nominal longitude of 0 degrees with respect to an Earth centred rotating coordinate system.*

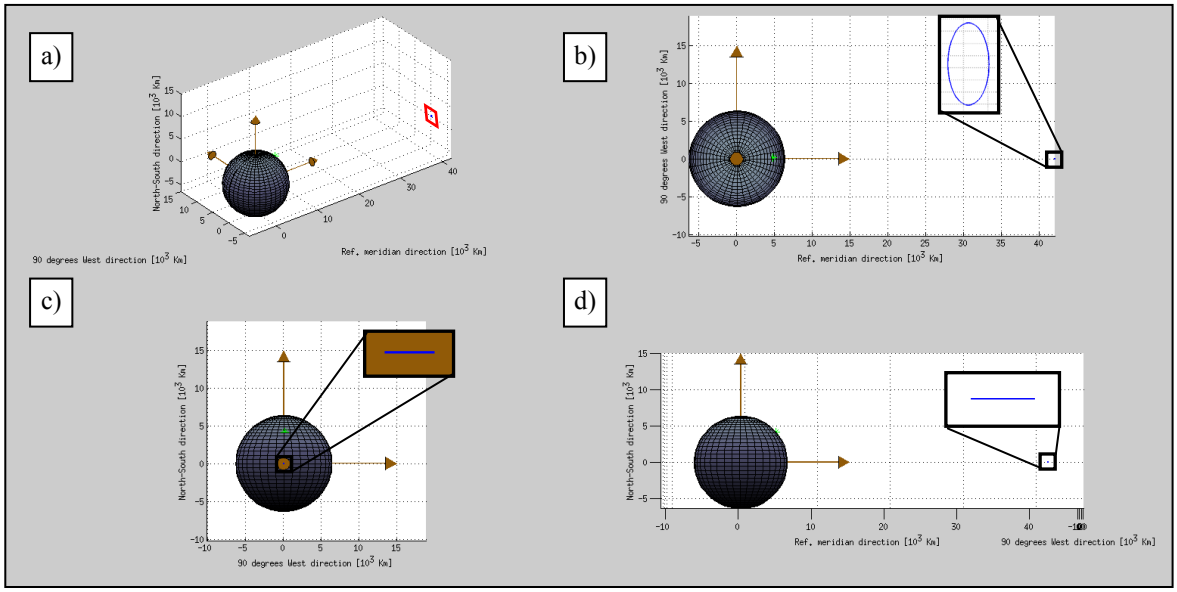


*Fig. 5.4 a) 3D orbital representation. b) Top view representation (reference meridian-90º West cut). c) Satellite nadir plane (North-90ºWest cut). d) Side view (North-Reference meridian cut).*

In Fig. 5.3, a 3D representation of the satellite motion is plotted during a whole period (1 sidereal day: 86164 sec). As it can be seen, the maximum length of the synthetic aperture is achieved in 12 hours (half of the period) which is plotted as a green line in Fig. 5.3 and

correspond to the East-West maximum displacement of the platform. The rest of the orbit is plotted in blue and during this time the satellite moves from West to East reaching the initial position after the whole period. So in this case, two identical maximum synthetic apertures lengths can be achieved with a geosynchronous satellite in one day.

In the example presented in Fig. 5.3 and Fig. 5.4, the satellite motion computed during the 12 hours corresponding to the green line is equal to 81.7 Km much larger than the theoretical synthetic aperture length. This difference arises from the non-constant radius of the orbit, which produces an approaching-moving away motion that does not contribute to the actual synthetic aperture seen from the point of view of the target. This behaviour can be checked in Fig. 5.4 b) and d) where the non-constant radius of the orbit can be appreciated. Therefore, the synthetic aperture length computation should only take into account the along track variations between the satellite and the targets which correspond to the relative motion seen in Fig. 5.4 c). Then, in the actual synthetic aperture length computation, the radius variation must be subtracted to the satellite motion to obtain the along track movement of the satellite. Equation (5.2) is used to compute the actual length of the synthetic aperture.

$$L_{SA} = \int_{t_{ac}} \sqrt{\left(\frac{dx_{sat}(t)}{dt}\right)^2 + \left(\frac{dy_{sat}(t)}{dt}\right)^2 + \left(\frac{dz_{sat}(t)}{dt}\right)^2 - \left(\frac{d\,r_{orbit}(t)}{dt}\right)^2}\, dt \qquad (5.2)$$

With this consideration, the synthetic aperture length is calculated for the example in the Fig. 5.3 obtaining values of 67.47 Km for both, the blue and green paths. These results are consistent with the theoretical ones obtained with (5.1).

Alternatively, a GeoSAR system may be conceived with a perfect circular (zero eccentricity) but slightly inclined orbit. So, a North-South relative motion similar to the typical LEO SAR systems can be achieved. This situation is complementary to the previous one so, once again, the versatility of a GeoSAR is demonstrated. Let's us consider a similar situation than in the previous case but taking an scene over the equator and a nominal longitude of the satellite shifted with respect to the longitude of the scene. The new scenario is presented in Fig. 5.5.

As it is shown, in this case the relative motion will be achieved with the latitude variation of the satellite since the longitude is fixed due to the zero eccentricity and the perfect circular orbit. This latitude variation is computed with (4.21) whose maximum value depends basically on the orbit inclination ($i$). Similarly than in the previous case, the maximum length of the synthetic aperture in this case is computed as the angle variation of the satellite (latitude history) multiplied by the orbital radius:

$$L_{SA_{\max}} = r \cdot \Delta\varphi_{\max} = 2\,i \cdot r \qquad (5.3)$$

So, considering (5.3) and the synthetic aperture length obtained in the precious example (67.5 Km), an orbit inclination of 0.046 degrees should be enough to get similar values. Once again the situation has been simulated with the GeoSAR Simulator and the results are presented next.

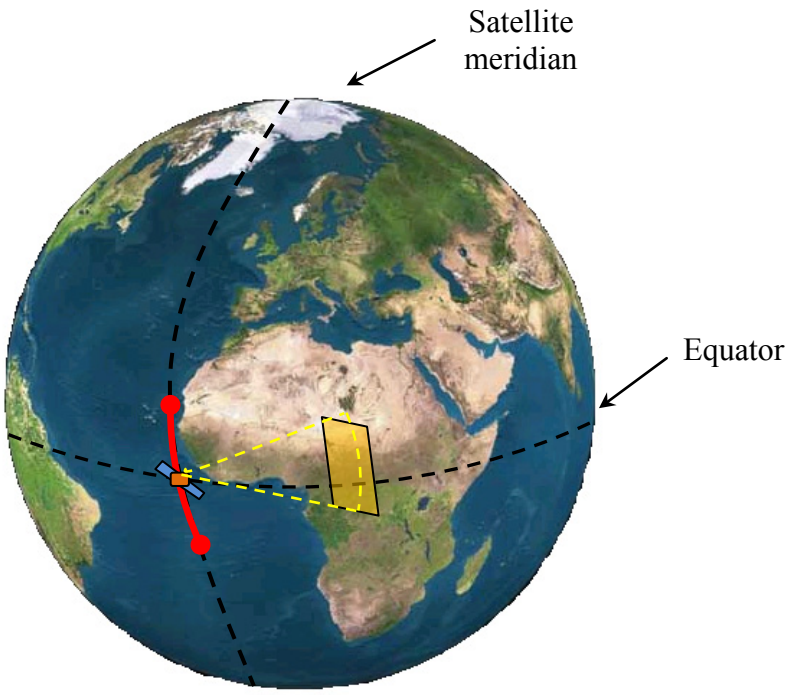


*Fig. 5.5 Geosynchronous satellite track considering zero eccentricity in the orbit and small inclination*

In this case, the orbit eccentricity has been set to 0 while the inclination to 0.045862 degrees to obtain similar lengths than in the previous case. A nominal longitude of the satellite equal to -30 degrees has been chosen. The orbital plots are presented in Fig. 5.6 and Fig. 5.7.

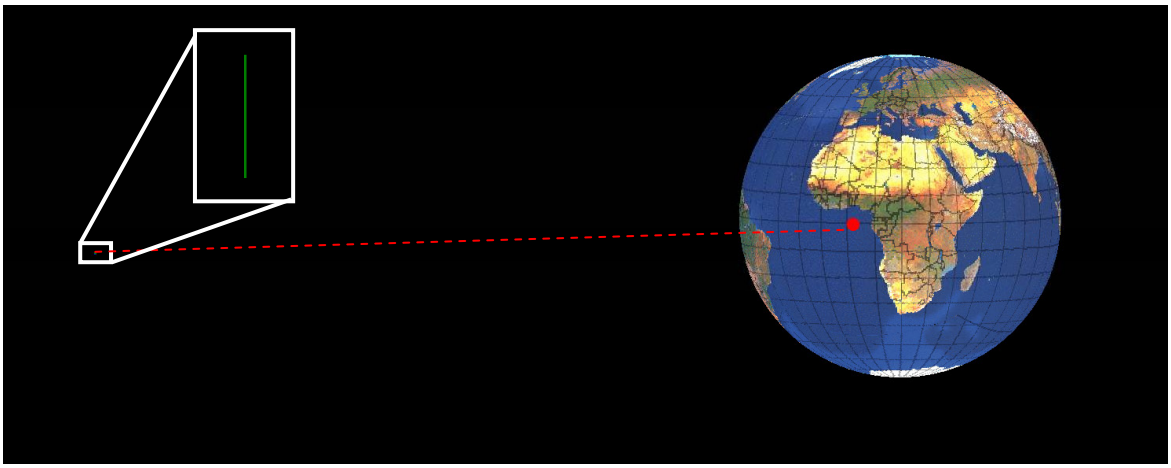

*Fig. 5.6 3D satellite orbit representation considering a 0.046 degrees inclined orbit with zero eccentricity and nominal longitude of -30 degrees with respect to an Earth centred rotating coordinate system.*

In this situation, as it can be seen in Fig. 5.6, the satellite describes a vertical line with only latitude variations as it was expected. Furthermore, the orbital radius is constant since a perfect circular orbit is considered. The constant orbit radius can be appreciated in Fig. 5.7 b) where the top view shows only a point with no rapprochement of the satellite towards the Earth's centre. So, (5.2) also applies in this situation but the last term, corresponding to the orbital radius variation, will be zero. The simulated results obtained with the GeoSAR Simulator gives a length of the synthetic aperture of 67.49 Km, really close to the theoretical value.

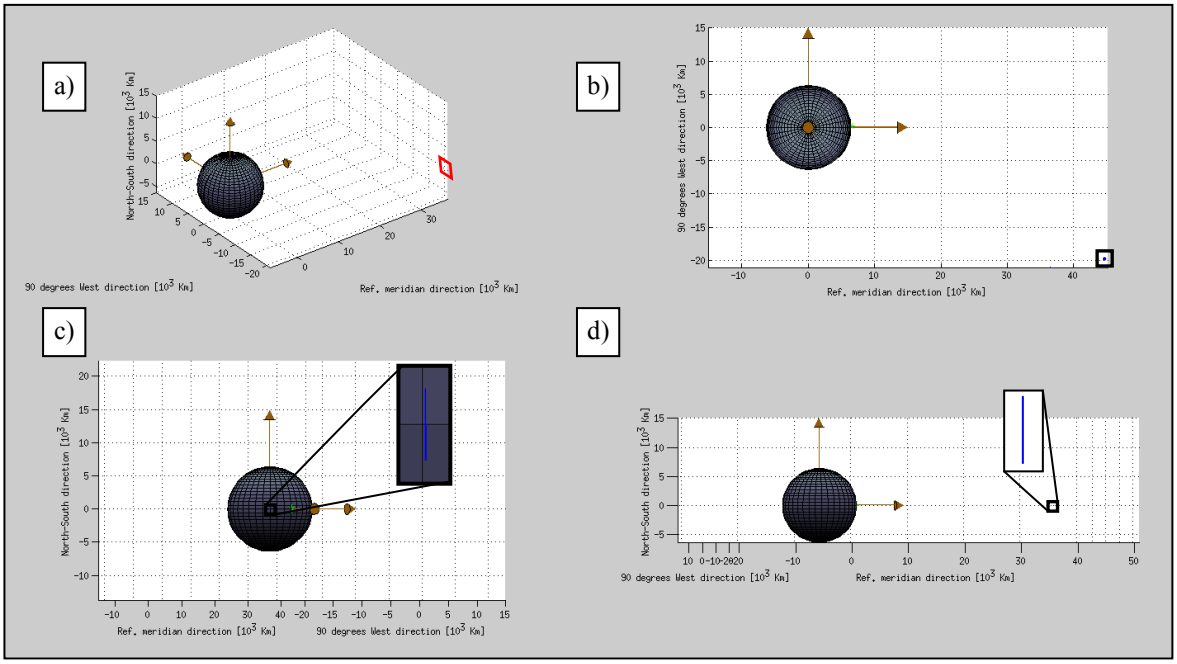


*Fig. 5.7 a) 3D orbital representation. b) Top view representation (reference meridian-90º West cut). c) Satellite nadir plane. d) Side view (North-Reference meridian cut).*

After these two basic examples, let's consider a more complex and generic situation with a satellite with small perturbation in the eccentricity and inclination of the orbital plane. In this case, the satellite track (section 4.2) will no longer be a vertical or horizontal line. The combination of eccentricity and inclination variations will result in inclined lines or ellipses depending on the argument shift between the satellite longitude and latitude history governed by the argument of the perigee ( $\omega$ ) in (4.19) and (4.21).

In order to analytically compute the length of the synthetic aperture for an elliptical track, the basics on the ellipse geometry will be necessary. The purpose of this section is to give just the necessary concepts and justify their applicability to our problem to understand the calculations. So now, deviations on the nominal longitude and latitude of the satellite have to be jointly considered. As it was previously explained, the satellite movement is described by the combination of (4.19) and (4.21) for the longitude and latitude variation. These two equations will describe an ellipse that will be inscribed in a *4e* by *2i* rectangle, as it is shown in Fig. 5.8.

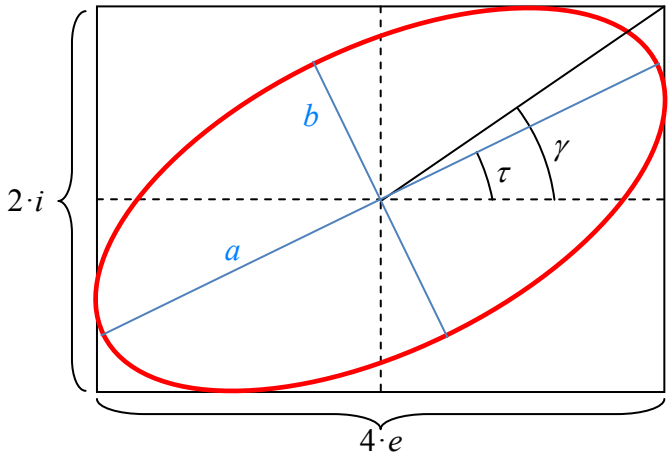


*Fig. 5.8 Elliptical satellite track inscribed in a rectangle of side 4e by 2i given by the satellite motion described in section 4.2*

To compute the maximum achievable synthetic aperture length, the semi-major axis ($a$) of the angular variation given by the ellipse in Fig. 5.8 must be found and multiplied by the mean radius of the orbit, similarly than in the previous examples. The maximum length of the synthetic aperture will be related with the maximum longitude and latitude shift and with the tilt angle ( $\tau$ ) as well. In order to obtain the relation between the different angles that define the ellipse, the longitude and latitude histories will be written as:

$$x = \Delta\lambda = A_x \sin\left(\Omega_E \left(t - t_p\right)\right) \quad where \ A_x = 2e \tag{5.4}$$

$$y = \varphi_{SL} = A_y \sin\left(\omega + \Omega_E \left(t - t_p\right)\right) \ where \ A_y = i \tag{5.5}$$

where $\omega$ is the argument of the perigee and it is called the phase shift between the two components ( $\delta$ ) while $\Omega_E$ stand for the Earth's rotation angular velocity. The other parameter that can be computed directly is $\gamma$ :

$$\gamma = \tan^{-1} \frac{A_y}{A_x} \tag{5.6}$$

From $\delta$ and $\gamma$, the tilt angle can be found by using (5.7). Another important parameter of an ellipse is the ratio between the major and minor axis. This is given by the ellipticity ( $\varepsilon$ ) provided by (5.8).

$$\tan\left(2\tau\right) = \tan\left(2\gamma\right) \cdot \cos\left(\delta\right) \tag{5.7}$$

$$\sin\left(2\varepsilon\right) = \sin\left(2\gamma\right) \cdot \sin\left(\delta\right) \tag{5.8}$$

The axial ratio ( $AR = a / b$ ) is obtained from the ellipticity as:

$$\varepsilon = \cot^{-1}\left(\mp AR\right) \tag{5.9}$$

All these parameters will give us information about the shape and orientation of the ellipse. Finally, the major axis of the ellipse must be determined from (5.4) and (5.5). It corresponds to the maximum angular variation of the satellite and can be found by computing the points of the ellipse at furthest distance from the centre (x=0,y=0). So, the derivative of this distance must be computed and equalled to 0. The development is presented next. The anglular shift of the points of the ellipse with respect to the nominal position of the satellite can be obtained as:

$$\phi = \sqrt{x^2 + y^2} \tag{5.10}$$

where $x$ and $y$ correspond to (5.4) and (5.5), respectively; and $\phi$ corresponds to the angle at the centre of the earth between the nominal position and a point of the orbit. However, maximize (5.10) is equivalent to maximize the distance squared whose derivative is easier to compute. So, the derivative of $\phi^2$ is computed as:

$$\frac{\delta\phi^2}{\delta t}=\frac{\delta\left(x^2+y^2\right)}{\delta t}=\frac{\delta\left(\left[A_x\sin\left(\Omega_E\left(t-t_p\right)\right)\right]^2+\left[A_y\sin\left(\omega+\Omega_E\left(t-t_p\right)\right)\right]^2\right)}{\delta t} \tag{5.11}$$

To obtain the instants where the maximums and minimums of the angular shift occur (5.11) is equalled to 0:

$$\frac{\delta\left(\left[A_x\sin\left(\Omega_E\left(t-t_p\right)\right)\right]^2+\left[A_y\sin\left(\omega+\Omega_E\left(t-t_p\right)\right)\right]^2\right)}{\delta t}=0 \tag{5.12}$$

$$A_x{}^2\cdot 2\sin\left(\Omega_E\left(t-t_p\right)\right)\cos\left(\Omega_E\left(t-t_p\right)\right)\cancel{\Omega_E}+\ldots$$

$$+A_y{}^2\cdot 2\sin\left(\omega+\Omega_E\left(t-t_p\right)\right)\cos\left(\omega+\Omega_E\left(t-t_p\right)\right)\cancel{\Omega_E}=0$$

Using the trigonometric property (5.13) in the previous equation, (5.14) is obtained.

$$\sin\alpha\cdot\cos\alpha=\frac{1}{2}\sin 2\alpha \tag{5.13}$$

$$A_x{}^2\cdot\cancel{2}\frac{\gamma}{\cancel{2}}\sin\left(2\Omega_E\left(t-t_p\right)\right)+A_y{}^2\cdot\cancel{2}\frac{\gamma}{\cancel{2}}\sin\left(2\left(\omega+\Omega_E\left(t-t_p\right)\right)\right)=0 \tag{5.14}$$

And using $\cos(\alpha+\beta)=\cos\alpha\sin\beta+\sin\beta\cos\alpha$, (5.14) can be rearranged as:

$$A_x{}^2\sin\left(2\Omega_E\left(t-t_p\right)\right)+A_y{}^2\left[\sin(2\omega)\cos\left(2\Omega_E\left(t-t_p\right)\right)+\cos(2\omega)\sin\left(2\Omega_E\left(t-t_p\right)\right)\right]=0$$

$$A_x{}^2\cancel{\sin\left(2\Omega_E\left(t-t_p\right)\right)}+A_y{}^2\cancel{\sin\left(2\Omega_E\left(t-t_p\right)\right)}\left[\sin(2\omega)\frac{\cos\left(2\Omega_E\left(t-t_p\right)\right)}{\sin\left(2\Omega_E\left(t-t_p\right)\right)}+\cos(2\omega)\right]=0$$

$$A_x{}^2+A_y{}^2\left[\frac{\sin(2\omega)}{\tan\left(2\Omega_E\left(t-t_p\right)\right)}+\cos(2\omega)\right]=0 \tag{5.15}$$

Finally, isolating the $t$ and substituting $A_x$ and $A_y$, the times with maxim (5.16) and minim (5.17) angular shift are obtained as:

$$t_{\max}=\frac{\arctan\left(\dfrac{\sin(2\omega)}{-\left(\dfrac{2e}{i}\right)^2-\cos(2\omega)}\right)+(2n-1)\pi}{2\Omega_E}+t_p \qquad with \qquad n\in\left[-\infty\ldots\infty\right] \tag{5.16}$$

$$t_{\min} = \frac{\arctan\left(\dfrac{\sin(2\omega)}{-\left(\dfrac{2e}{i}\right)^2 - \cos(2\omega)}\right) + 2n\pi}{2\Omega_E} + t_p \qquad with \qquad n \in [-\infty \ldots \infty] \tag{5.17}$$

As it can be seen, the periodicity of the arctangent function gives infinite results which correspond to the daily periodicity of the geosynchronous satellite but in one period only two minimums and maximums are obtained. Therefore, to determine the maximum length of the synthetic aperture, the angular aperture between the two consecutive maximum positions, which corresponds to the major axis of the ellipse in Fig. 5.8, has to be computed and multiplied by the mean radius of the geosynchronous satellite:

$$L_{SA_{\max}} = r \cdot \Delta\phi_{\max} = r \cdot \left(\phi\left(t_{\max_1}\right) + \phi\left(t_{\max_2}\right)\right) \tag{5.18}$$

Let's put some numbers and compare the results obtained in this case with the previous ones where the variations in longitude and latitude were considered separately. In this example, an inclination of 0.046 degrees and eccentricity of 0.0004 will be taken as a input parameters. The argument of the perigee will be set to 30 degrees in this first example. Later on, different values of $\omega$ will be tried in order to characterize its influence to the achievable synthetic aperture length. The time over the perigee ($t_p$) has been set to 0 since it is only a time reference. The resultant ellipse is plotted in Fig. 5.9. The longitude and latitude variations correspond to the expected ones (*4e* for longitude and *2i* for latitude). The tilt angle, computed with (5.7), is equal to 45 degrees. The angle ($\phi$) evolution from the nominal position of the satellite is shown in Fig. 5.10. As it can be seen, the two maximum angles occur at $t_{\max_1} = 17925\,\text{sec}$ and $t_{\max_2} = 61038\,\text{sec}$ with an angular variation of 0.0011 radians each one.

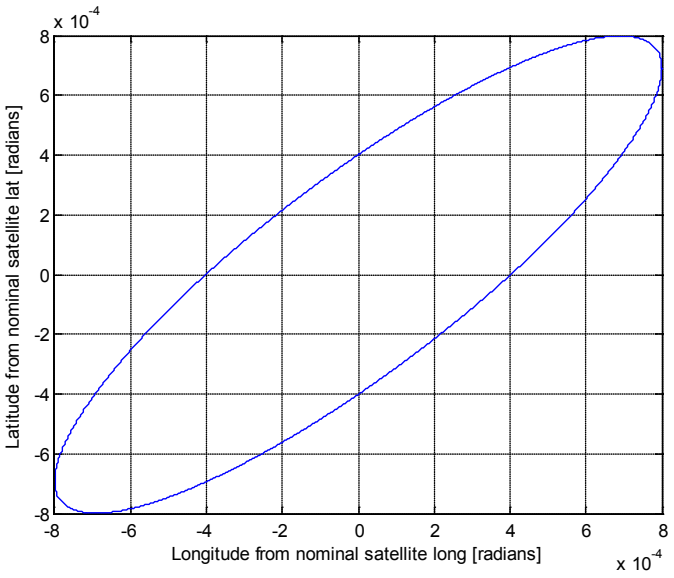


*Fig. 5.9 Satellite track simulation considering an orbit eccentricity of 0.0004 and inclination of 0.046 degrees*

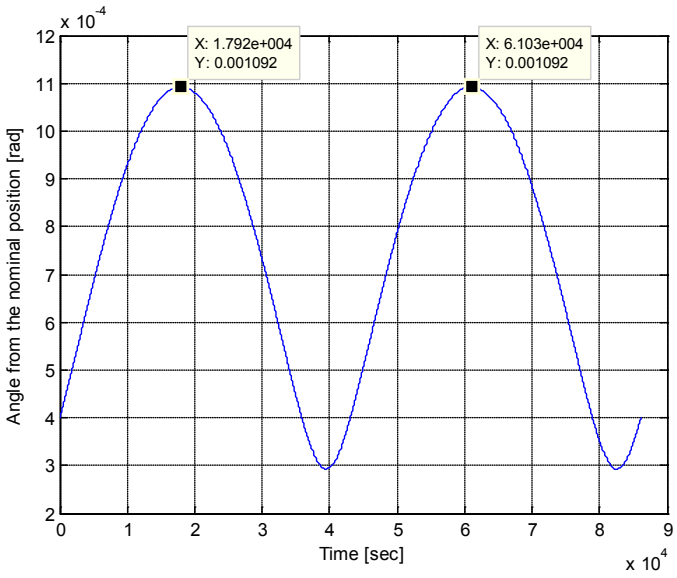


*Fig. 5.10 Satellite angle from nominal satellite position simulation considering an orbit eccentricity of 0.0004 and inclination of 0.046 degrees*

To corroborate the formulation previously derived, (5.16) is used to compute the $t_{\max_1}$ and $t_{\max_2}$ obtaining values of 17953 and 61036 seconds respectively, really close to the simulated values. The small variations observed between the theoretical and simulated results arise from the approximations considered in the theoretical analysis of the longitude and latitude histories. Computing $\phi\left(t_{\max_1}\right)$ and $\phi\left(t_{\max_2}\right)$ with (5.10) a value of 1.09 miliradians for both cases. So, the resultant synthetic aperture will have a theoretical length of:

$$L_{SA_{\max}} = r \cdot \Delta\phi_{\max} = 42164\,Km \cdot \left(2 \cdot 1.09 \cdot 10^{-3}\right) = 92.12\,Km \qquad (5.19)$$

which is larger than the ones obtained in the previous example. It means that combining perturbations in eccentricity and inclination, larger synthetic aperture lengths and better image resolution can be achieved.

As in the previous cases, let's compare the theoretical analysis with the ones computed with our GeoSAR simulator. It must be pointed out that the theoretical analysis uses equations (4.19) and (4.21) which come from an approximation (see section 4.2 for the complete derivation of them). So, it is expected to obtain more accurate results with the simulation which take the actual motion of the satellite without approximations.

So, in Fig. 5.11 and Fig. 5.12, the resultant orbit with the above parameters is presented. It is interesting to take special attention to Fig. 5.12 c) where the satellite track is shown. In this case the elliptical behaviour predicted with the analytical study in Fig. 5.9 can be appreciated. The points used in the maximum synthetic aperture length computation are marked in Fig. 5.12 c). In this case, the simulated maximum length is equal to 92.66 Km, really close to the result obtained in (5.19). Therefore, the validity of the previous analysis to obtain the achievable synthetic aperture with a generic geosynchronous satellite considering longitude and latitude variation from the nominal position has been checked.

*Fig. 5.11 3D satellite orbit representation considering a 0.046 degrees inclined orbit with 0.0004 eccentricity and nominal longitude of -30 degrees with respect to an Earth's centred rotating coordinate system.*

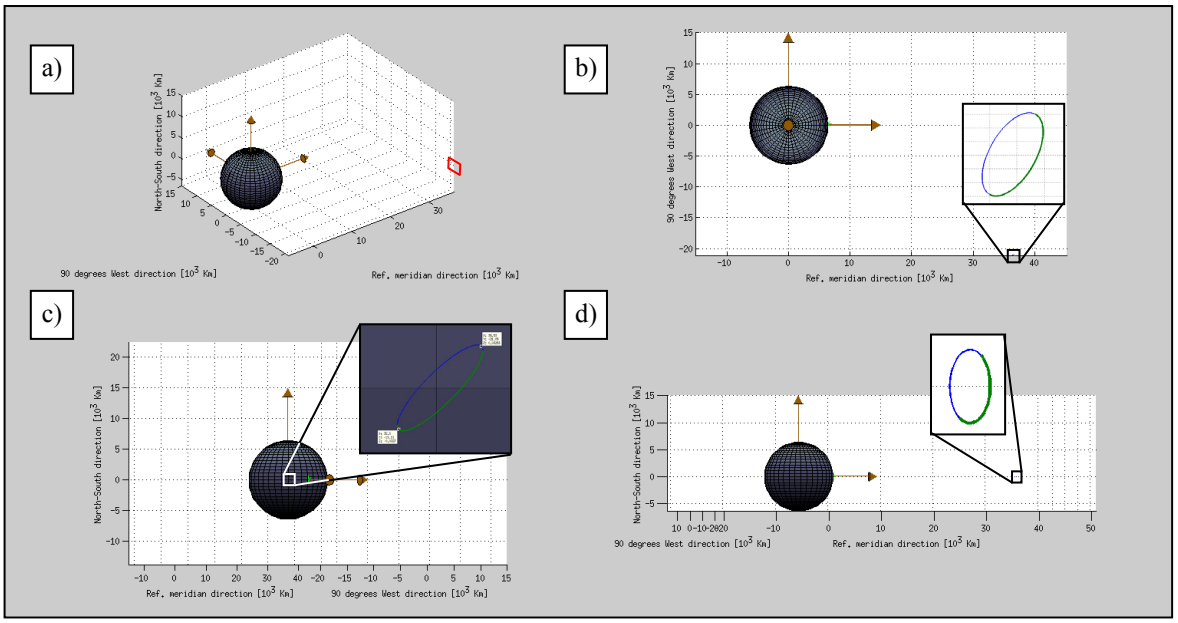


*Fig. 5.12 a) 3D orbital representation. b) Top view representation (reference meridian-90º West cut). c) Satellite nadir plane. d) Side view (North-Reference meridian cut).*

Therefore, the previous analysis offers a fast and really accurate way to compute the synthetic aperture length achievable with a geosynchronous satellite. However, if we look careful to a real situation, this synthetic aperture length is valid for a scene situated perpendicularly to the direction of the computed synthetic aperture. In Fig. 5.13, the situation is graphically presented.

As it can be seen in Fig. 5.13, for the first example presented, all the zones situated at the same longitude than the nominal longitude of the satellite will see the largest along-track satellite movement and consequently will have the best azimuth resolution. On the other hand, in the second example, the zones with the best resolution will be the ones over the Equator. For a generic geosynchronous satellite, this strip will be situated perpendicularly to the direction of the major axis of the ellipse described by the satellite track.

*Fig. 5.13 Earth zones (yellow slashed lines) which will see the largest along-track satellite motion for different orbital configurations.*

Consequently, the effective synthetic aperture length for a scene placed at a random position has to be re-computed as the projection of the aperture length over the perpendicular direction to the illumination. To do that, the spherical angle (see section 4.1) of the target situation from the Equator computed at the nominal position of the satellite nadir point, angle $\beta$ in Fig. 5.14, must be computed. It is found from the spherical cotangent formula (4.4) as:

$$\begin{aligned} b &= \varphi_T - \varphi_{SL_0} \qquad A = 90^\circ \\ c &= \lambda_T - \lambda_{SL_0} \qquad C = \beta \end{aligned}$$

$$\cancel{\cos\left(\varphi_T - \varphi_{SL_0}\right)\cos 90^\circ} = \sin\left(\varphi_T - \varphi_{SL_0}\right)\cot\left(\lambda_T - \lambda_{SL_0}\right) - \sin 90^\circ \cot\beta$$

$$\beta = \arctan\left(\frac{\tan\left(\lambda_T - \lambda_{SL_0}\right)}{\sin\left(\varphi_T - \varphi_{SL_0}\right)}\right) \tag{5.20}$$

Once the angle between the scene and nadir point is computed, it must be contrasted with the orientation of the ground track ellipse of the satellite. If we take the tilt angle ( $\tau$ ) of the ellipse from the equator, shown in Fig. 5.14, the relative angle between the major axis of the ellipse and the direction of the scene will be:

$$\alpha = \left|\pi + \beta - \tau\right| \tag{5.21}$$

The geometric interpretation of the problem is presented in Fig. 5.15. As it can be seen, the actual length obtained for a determined orientation of the scene with respect to the satellite track ellipse is smaller than the maximum achievable length. This length is determined by the angle $\alpha$ , computed as in (5.21), which can be obtained approximately as:

$$L_{SA} = L_{SA_{\max}} \left|\sin\alpha\right| = r \cdot \Delta\phi_{\max} \left|\sin\alpha\right| \tag{5.22}$$

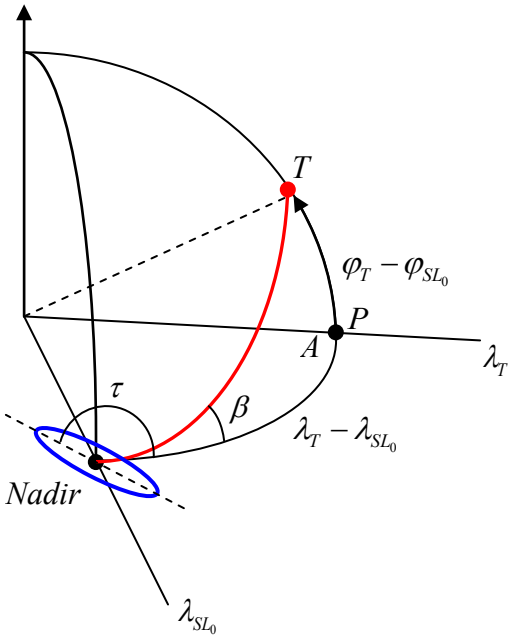


*Fig. 5.14 Target angle from the Equator at the satellite nadir point*

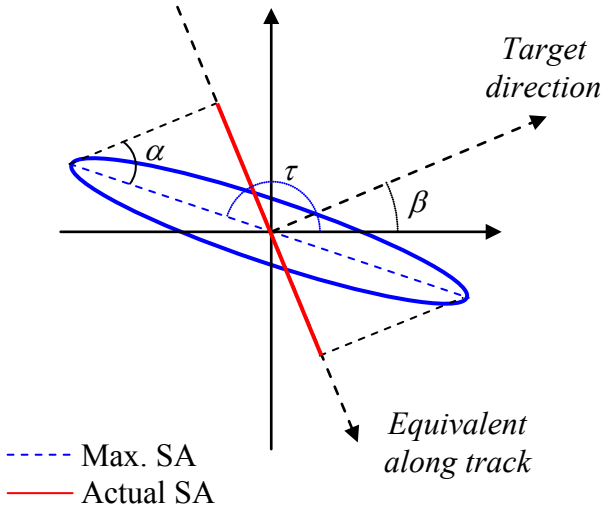


*Fig. 5.15 Maximum synthetic aperture length vs. acutal aperture length for a randomly positioned target*

As it has been shown in this section, the length of the synthetic aperture of a geosynchronous SAR will depend on a large number of factors, i.e. eccentricity of the orbit, inclination of the orbital plane, argument of the perigee, orientation of the ground track ellipse with respect to the scene location, etc. Furthermore, the integration time is also crucial to determine the actual length of the synthetic aperture. In this section, the whole satellite motion has been considered to compute the maximum synthetic aperture length achievable. In the next section, the influence of the integration time is analysed.

## 5.2 Integration time and achieved resolution

In the previous section, the satellite-ground relative motion has been studied. The dependence with the orbital parameters and orientation of the scene with respect to the satellite motion has been analysed and the basic formulation proposed. However, in all the calculations, the integration time has not been taken into account, computing all the parameters with the whole satellite orbital motion.

In a real acquisition, the integration time in the image acquisition will be limited and, sometime, it will be shorter than half of the satellite period. Therefore, only a part of the satellite trajectory will be taken during this time, reducing the length of the synthetic aperture and, consequently, the achievable azimuth resolution. The dependence with the acquisition length is clear but the time when the acquisition starts is important in the determination of the synthetic aperture length as well.

In any SAR system, the azimuth or along-track resolution is related with the synthetic aperture length as follows [2]:

$$\rho_{az} = \frac{1}{2}\frac{\lambda}{L_{SA}}R \tag{5.23}$$

where $\lambda$ is the wavelength of radar operation, $L_{SA}$ the synthetic aperture length of each acquisition and $R$ the slant range to the scene considered. The large number of possibilities in the synthetic aperture formation makes difficult to consider all the cases in this analysis. Therefore, in the following lines, some particular situations will be analysed and discussed to see the integration time requirements to fulfil an azimuth resolution criteria or the other way around.

Let's start with a simple case, considering a geosynchronous satellite with small eccentricity in its orbit and no inclination of the orbital plane. As it has been studied in the previous section, the maximum synthetic aperture length in this case is obtained from (5.1). Then, the best azimuth resolution achievable with this system considering the whole satellite motion can be computed as:

$$\rho_{az_{\max}} = \frac{1}{2}\frac{\lambda}{4\cdot e\cdot r}R = \frac{\lambda}{8\cdot e}\frac{R}{r} \tag{5.24}$$

On the other hand, the problem can be set out in the other way. Given a desired azimuth resolution, one can be interested in obtain the orbital configuration necessary to satisfy the input requirements. For the previous example, if the signal and swath parameters are fixed, the only parameter available to be modified in the satellite orbital design is the orbit eccentricity. Then, this parameter must be tuned to fulfil the following equation:

$$e_{\min} = \frac{\lambda}{8\cdot\rho_{az_{req}}}\frac{R}{r} \tag{5.25}$$

In Table 5.1, a summary of the range of expected azimuth resolutions for different frequency bands is presented. In this case a mean range to the scene of 36950 Km and an

typical orbit eccentricity of 0.0004 have been considered. As it can be seen, fine resolution can be achieved working at high frequencies. However, the frequency can not be increased arbitrary since other SAR aspects and technological limitations have to be taken into account. Furthermore, these values have been computed considering the whole synthetic aperture of the satellite which only can be achieved by integrating at least 12 hours. Such integration time can be too long for some applications which need rapid acquisition in scenes with short temporal coherence.

| Frequency band | Frequency Range | $\lambda$ | Achievable resolution |
|---|---|---|---|
| C band | 4 to 8 GHz | 7.5 to 3.75 cm | 20.5 to 10.3 m |
| X band | 8 to 12 GHz | 3.75 to 2.5 cm | 10.3 to 6.85 m |
| Ku band | 12 to 18 GHz | 2.5 to 1.67 cm | 6.85 to 4.57 m |
| K band | 18 to 26.5 GHz | 1.67 to 1.13 cm | 4.57 to 3.09 m |
| Ka band | 26.5 to 40 GHz | 1.13 to 0.75 cm | 3.09 to 2.05 m |

*Table 5.1 Range of achievable azimuth resolutions at different frequency bands*

To see how the acquisition duration affects to the synthetic aperture and the resolution in the previous example, let's take the equation (4.19) considering a time of perigee equal to zero. Depending on the time interval considered, the longitude variation of the satellite will be different as it shown in Fig. 5.16 considering the parameters above. As the plot shows, the longitude variation during the 5 hours considered in the red line is higher than the variation considering the same acquisition lengths at green zones. The red line corresponds to the sinus, in (4.19), cross to zero and is where the sinus presents the highest slope.

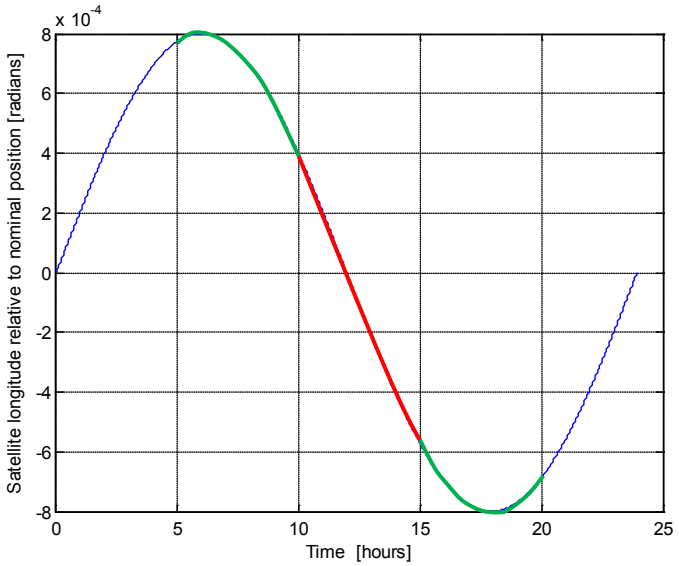


*Fig. 5.16 Satellite longitude variation. Red zone presents higher variation than green ones in the same integration time*

Therefore, it is in the red zone where the best trade-off between integration time and resolution will be obtained since for the same integration time a larger synthetic aperture will be obtained than in other regions. Let's define the integration time ($T_i$) between $t=[-T_i/2, T_i/2]$. Using this time interval directly on equation (4.19), the acquisition corresponds to an interval equivalent to the one plotted in red in Fig. 5.16 since it will be centred at the nominal longitude of the satellite ($\lambda(t=0)=\lambda_{SL}$). The extreme values of the satellite longitude in function of the integration time will be:

$$\lambda_1 = \lambda_{SL} + 2e\sin\left(-\Omega_E \frac{T_i}{2}\right) \tag{5.26}$$

$$\lambda_2 = \lambda_{SL} + 2e\sin\left(\Omega_E \frac{T_i}{2}\right) \tag{5.27}$$

Knowing that $\sin(-\beta) = -\sin(\beta)$, the longitude variation during *Ti* can be re-written as:

$$\begin{aligned}\Delta\lambda = \lambda_2 - \lambda_1 &= \cancel{\lambda_{SL}} + 2e\sin\left(\Omega_E \frac{T_i}{2}\right) - \left[\cancel{\lambda_{SL}} - 2e\sin\left(\Omega_E \frac{T_i}{2}\right)\right] = \ldots \\ &= 4e\sin\left(\Omega_E \frac{T_i}{2}\right)\end{aligned} \tag{5.28}$$

And that corresponds to a length of the synthetic aperture of:

$$L_{SA} = r\cdot\Delta\lambda = r\cdot 4e\sin\left(\Omega_E \frac{T_i}{2}\right) \tag{5.29}$$

From (5.23), the azimuth resolution of the scene can be related with the integration time with the following equation for this particular example:

$$\rho_{az} = \frac{\lambda}{r\cdot 8e\sin\left(\Omega_E \frac{T_i}{2}\right)} R \tag{5.30}$$

Now, with (5.30), it is possible to obtain a relation between the minimum integration time required to get a desired resolution for a fixed parameters of the satellite orbit and the scene location. The integration time required will be:

$$T_{i_{req}} = \arcsin\left(\frac{\lambda}{r\cdot 8e\cdot\rho_{az}} R\right)\frac{2}{\Omega_E} \tag{5.31}$$

In Table 5.2, the required integration times at different bands to obtain a medium azimuth resolution image of 25 meters are presented. The satellite parameters are the same that the ones considered in the previous example: orbit eccentricity of 0.0004 and a distance to the scene of 36950 Km. The mean radius of the orbit is 42164 Km while the angular Earth's

rotation velocity is $7.3 \cdot 10^{-5}$ rad/sec. The results show that, in few hours, it is possible to obtain a medium resolution SAR image at X-, Ku-, K- and Ka-bands.

| Frequency band | Frequency Range | $\lambda$ | Integration time required |
|---|---|---|---|
| C band | 4 to 8 GHz | 7.5 to 3.75 cm | 7.35 to 3.22 hours |
| X band | 8 to 12 GHz | 3.75 to 2.5 cm | 3.22 to 2.11 hours |
| Ku band | 12 to 18 GHz | 2.5 to 1.67 cm | 2.11 to 1.40 hours |
| K band | 18 to 26.5 GHz | 1.67 to 1.13 cm | 1.40 to 0.95 hours |
| Ka band | 26.5 to 40 GHz | 1.13 to 0.75 cm | 0.95 to 0.63 hours |

*Table 5.2 Integration time required to obtain an azimuth resolution of 25 meters*

Equivalently to this example, the case with a non-eccentric orbit and only small perturbations on the inclination can be considered. The procedure is exactly the same only changing the longitude perturbations for the latitude history of the satellite. The final results obtained in this case are summarized in equations (5.32) to (5.35). As it can be seen, only the term *2e* is changed by *i*.

$$\rho_{az_{\max}} = \frac{1}{2}\frac{\lambda}{2 \cdot i \cdot r} R = \frac{\lambda}{4 \cdot i}\frac{R}{r} \tag{5.32}$$

$$i_{\min} = \frac{\lambda}{4 \cdot \rho_{az_{req}}}\frac{R}{r} \tag{5.33}$$

$$L_{SA} = r \cdot \Delta\varphi = r \cdot 2i \sin\left(\Omega_E \frac{T_i}{2}\right) \tag{5.34}$$

$$T_{i_{req}} = \arcsin\left(\frac{\lambda}{r \cdot 4i \cdot \rho_{az}} R\right)\frac{2}{\Omega_E} \tag{5.35}$$

For more complex satellite motion is not feasible to obtain a closed formula for the relation between integration time and resolution and it must be derived by simulations.

The range resolution will depend on the pulse bandwidth and incidence angle as in the case of a typical LEO SAR. So, the ground range resolution for the geosynchronous SAR case will be given by [2]:

$$\rho_{gr} = \frac{c}{2B \sin\theta_{in}} \tag{5.36}$$

where $c$ is the speed of light, $B$ is the transmitted pulse bandwidth and $\theta_{in}$ is the incidence angle at the considered point.

## 5.3 Timing and PRF selection. The diamond and dartboard diagram

The choice of the Pulse Repetition Frequency (PRF), which is the inverse of the period between two consecutive pulses sent by the radar, is constrained by a large number of factors. As it will be shown in the next section, the ambiguity level, azimuth and range, is highly dependent on the PRF but, at the same time, it has other constraints that has to be taken into account in the PRF selection.

In this section, the PRF restrictions related to the SAR interferences will be analyzed [2]. SAR systems use the same antenna for both transmit and receive. Therefore, the time must be divided between transmission and reception intervals periodically. The received echoes must be interspersed between two transmitted pulses in order not to lose any part of the received information. Furthermore, the values of the PRF must be selected such that the strong nadir echo from succeeding pulses do not arrive at the same time that the data reception window since it could mask the useful returns.

The transmit interference can be modelled with the next equations [2]:

$$Frac\left(2R_1 PRF/c\right)/PRF > \tau_0 + \tau_{RP} \tag{5.37}$$

$$Frac\left(2R_N PRF/c\right)/PRF > \frac{1}{PRF} - \tau_{RP} \tag{5.38}$$

and

$$Int\left(2R_N PRF/c\right) = Int\left(2R_1 PRF/c\right) \tag{5.39}$$

In these equations, $R_1$ is the slant range to the nearest point of the scene, $R_N$ is the slant range to the latest data sample in the recording window, $\tau_0$ is the duration of the transmitted pulse, and $\tau_{RP}$ is a guard time used in reception to avoid emitted-received pulse interferences. This value is, in most systems, about $\tau_0$. Finally, the function *Frac* extracts the fractional part of its argument, while the function *Int* takes the integer part of the value. In order to illustrate the meaning of these equations, Fig. 5.17a) shows the timing diagram of the radar transmission-reception events.

The reception burst, as we can see in Fig. 5.17a), has to be in between two consecutive pulse transmission events. This is imposed by equation (5.39) where the first and last data of the received burst are in the same inter-pulse period. Furthermore, equation (5.37) guarantees that the first data arrives after the guard time, while (5.38) adjusts the PRF such that the last data taken arrives before the guard interval of next emitted pulse.

On the other hand, we must be sure that the nadir return does not interfere to the reception windows. For this reason, as it can be observed in Fig. 5.17 b), PRF has to fulfil equations (5.40) and (5.41) [2].

$$2h/c + j/PRF > 2R_N/c \qquad j = 0, \pm 1, \pm 2, ...\pm n_h \tag{5.40}$$

$$2h/c + 2\tau_0 + j/PRF < 2R_1/c \qquad j = 0, \pm 1, \pm 2, ...\pm n_h \tag{5.41}$$

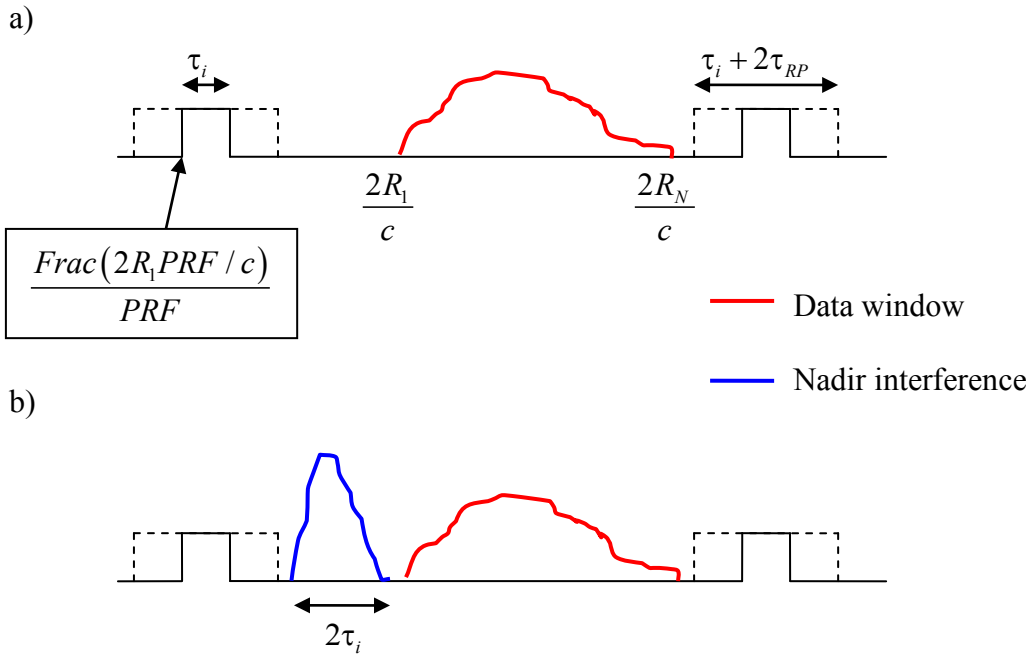


*Fig. 5.17 Timing diagram for PRF constraints: a) transmit interference and b) nadir interference*

where *h* is the platform height over the nadir point. In this equation, the duration of nadir return is considered $2\tau_0$. Actually, the duration of nadir return depends on the terrain illuminated, but it can be taken as a good approximation for a generic SAR system. Equation (5.40) adjusts the PRF such all the nadir returns of succeeding and preceding pulses (j index) arrive after the last data of the recording window. On the other hand, we must assure that these returns do not extend further than the next data reception window beginning. This constraint is given by equation (5.41).

Equation (5.41) is valid for SAR systems working at LEO orbits because the high power received from the nadir return saturates the receiver during all the echo duration being impossible to compress neither the nadir nor the desired echoes. On the other hand, in a GeoSAR configuration, it is expected that the nadir return will mask the desired echo (it will be more powerful than the echoes from the scene) but it will not be powerful enough to saturate the receiving chain due to the far distances where the satellite is orbiting. For this reason, the nadir return could be range compressed and the duration of that return after the range filtering will be $2\Delta\tau$, where $\Delta\tau$ is the inverse of the signal bandwidth, instead of $2\tau_0$. Then, equation (5.42) will be used in GeoSAR case:

$$2h/c + 2\Delta\tau + j/PRF < 2R_1/c \qquad j = 0, \pm 1, \pm 2, ...\pm n_h \qquad (5.42)$$

In SAR systems, it is common to use the diamond diagram to identify the zones with high transmission interference and/or nadir eclipses in function of the PRF. This diagram shows the useless combination of incidence angles and PRFs for a determined SAR configuration. In Fig. 5.18, the typical diamond diagram obtained with the geometrical parameters of a LEO SAR system is presented. As it can be seen, the red lines denote the zones where the transmission interferences equations are not fulfilled. On the other hand, green zones accounts for the nadir eclipses. In the SAR design procedure, a PRF in one of the white

holes has to be taken for the range of swath incidence angles of each acquisition. Let's take as an example a swath with incidence angles from 30 to 33 degrees. Looking at the diamond diagram of Fig. 5.18, a PRF around 3200 Hz (yellow squared limited by the free interference zones) should be considered in order to avoid the transmission interference and fulfil the nadir free eclipse equation.

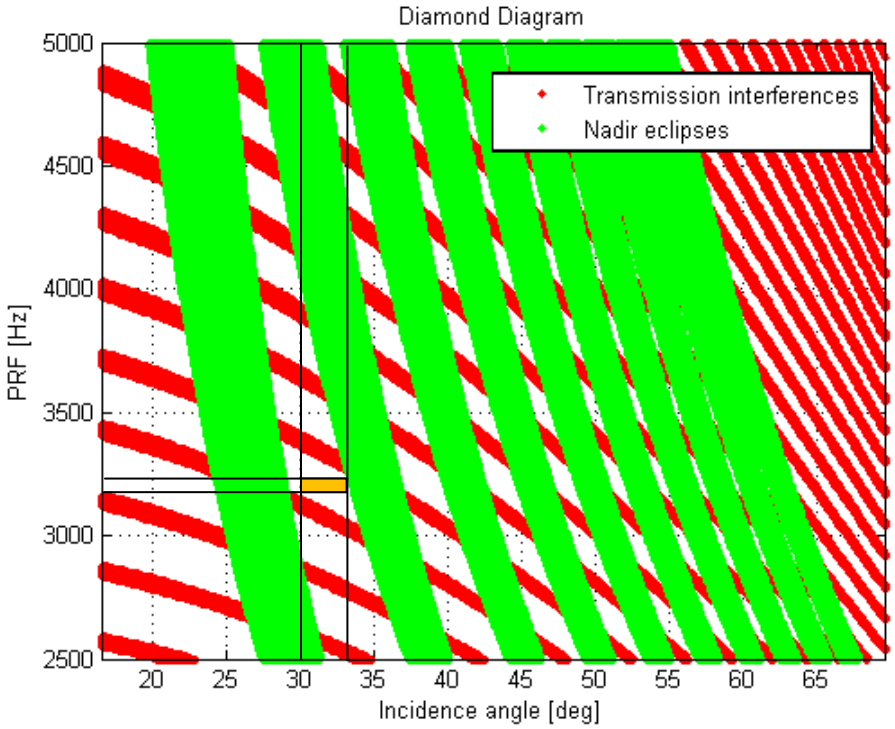


*Fig. 5.18 Typical diamond diagram for a LEO SAR system*

Similarly than in the LEO SAR, in GeoSAR system the diamond diagram can be also computed. In GeoSAR, the range of selectable PRFs will be lower in order to avoid range ambiguities and due to the larger scenes that are planned to cover. The diamond diagram for the GeoSAR case is presented in Fig. 5.19. As it can be seen, as the PRF is increased the nadir interference becomes more important making impossible the acquisition for high incidence angles.

The case of a GeoSAR, where the orbital position of the satellite is nearly fixed, makes possible to represent the forbidden zones in a novel way. This new diagram, never presented before in the geosynchronous satellites analysis for SAR applications, has been called dartboard diagram and it can be used to represent the transmission interferences and nadir eclipses for a fixed PRF over the Earth map. So, it will be easier to interpret the diamond diagram and see which will be the free-interference zones over the Earth's surface.

Let's explain how to obtain and interpret a Dartboard diagram from the typical diamond diagram for a GeoSAR system. As an example, a geosynchronous satellite placed at nominal longitude of 10º West and over the Equator is considered. The orbital perturbations of the satellite are considered small enough to take the nominal position of the satellite as a reference. In the case of high elliptical or well-inclined orbits, the

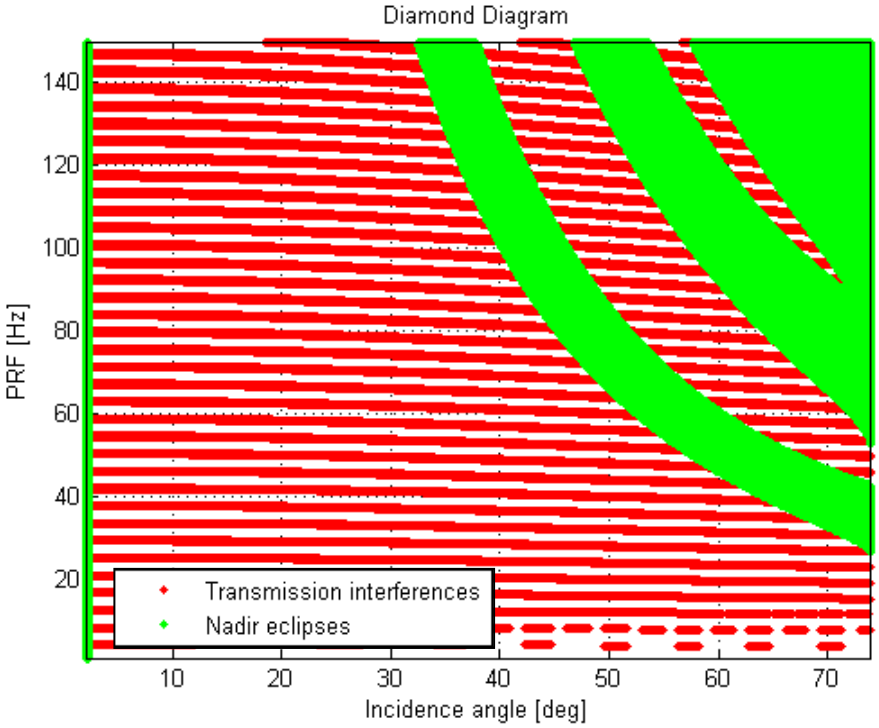


*Fig. 5.19 Diamond diagram for a GeoSAR system*

Dartboard diagram would not be useful, as in the LEO SAR, since this diagram is intended for a fixed or nearly fixed position of the satellite with respect to the Earth's surface, which is the case of the most of the GeoSAR missions considered in this report. Central and Western Europe, which covers the range of incidence angles from 40 to 60 degrees approximately, will be considered as the zone of interest of this example.

In this case, and considering the Diamond diagram obtained in Fig. 5.19, the PRFs over the 50 Hz should not be considered in order to avoid the nadir interference. Then, taking the PRFs of interest from 0 to 50 Hz and considering the range of incidence angle of the desired scene, in Fig. 5.20 a zoom-in of Fig. 5.19 is presented. As it can be seen, several PRFs can be chosen to avoid interferences.

After the PRF choice, 33 Hz in the example of Fig. 5.20 marked as a blue line, the forbidden incidence angles (nadir and transmission interferences) for this PRF can be plotted in a 2D or 3D Earth map to check the free interference zones in the Dartboard diagram. The 2D and 3D Dartboard diagrams for the previous example considering the PRF of 33 Hz are shown in Fig. 5.21 and Fig. 5.22, respectively.

Fig. 5.21 and Fig. 5.22 show that the zone of interest of this example is free from nadir and transmission interferences. Furthermore, the Dartboard diagram gives information about other possible zones that could be imaged using this configuration without interferences, i.e. South America or Eastern Africa, which is impossible to see directly with the typical diamond diagram. This feature makes the novel Dartboard diagram an interesting tool to determine the free interference regions for the radar operation PRF in a single plot.

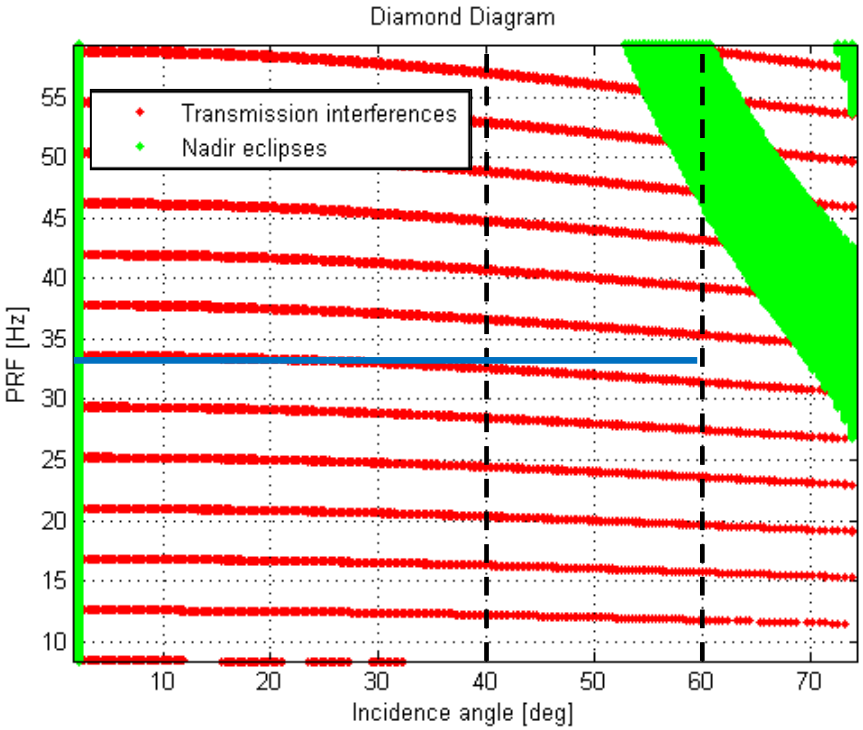


*Fig. 5.20 Diamond diagram for a GeoSAR system. PRF selection to cover the Central and Western Europe*

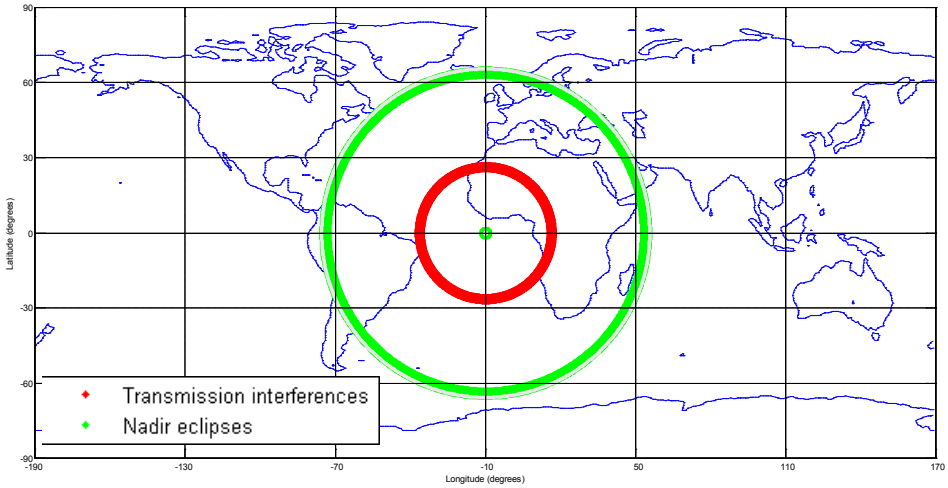


*Fig. 5.21 2D-Dartboard diagram for Geosynchronous satellite placed at 10° West. No interferences looking at Central and Western Europe*

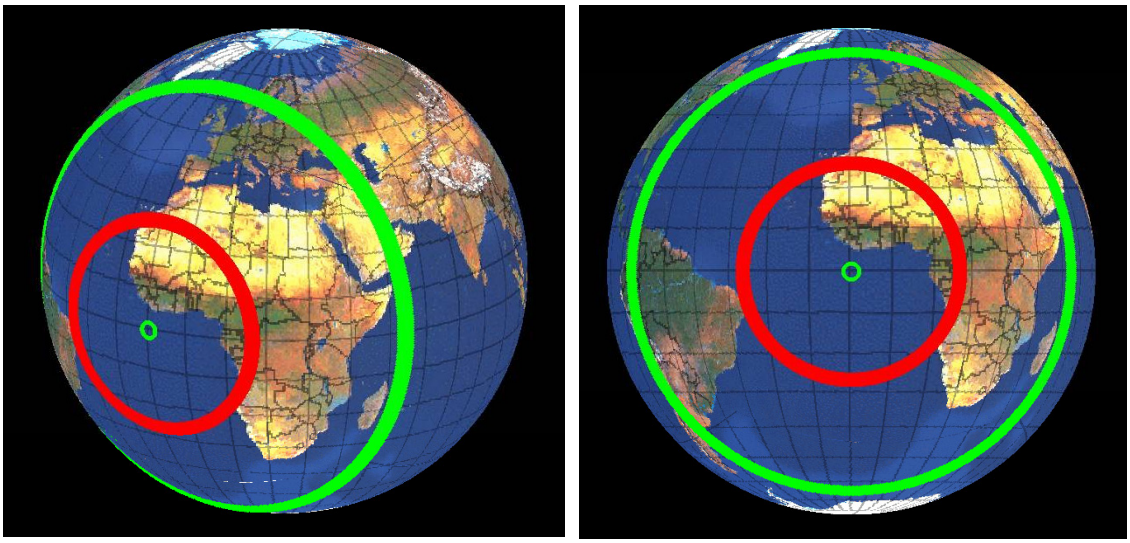

*Fig. 5.22 3D-Dartboard diagram for Geosynchronous satellite placed at 10º West. No interferences looking at Central and Western Europe*

So, as it has been explained in this section, the choice of the PRF is crucial for the right performance of the radar. For instance, taking the previous example but using a PRF of 104 Hz, the Dartboard diagram of Fig. 5.23 is obtained. As it can be seen, it is completely useless to scan a zone over Europe since it would be interfered by transmission events and the nadir eclipses.

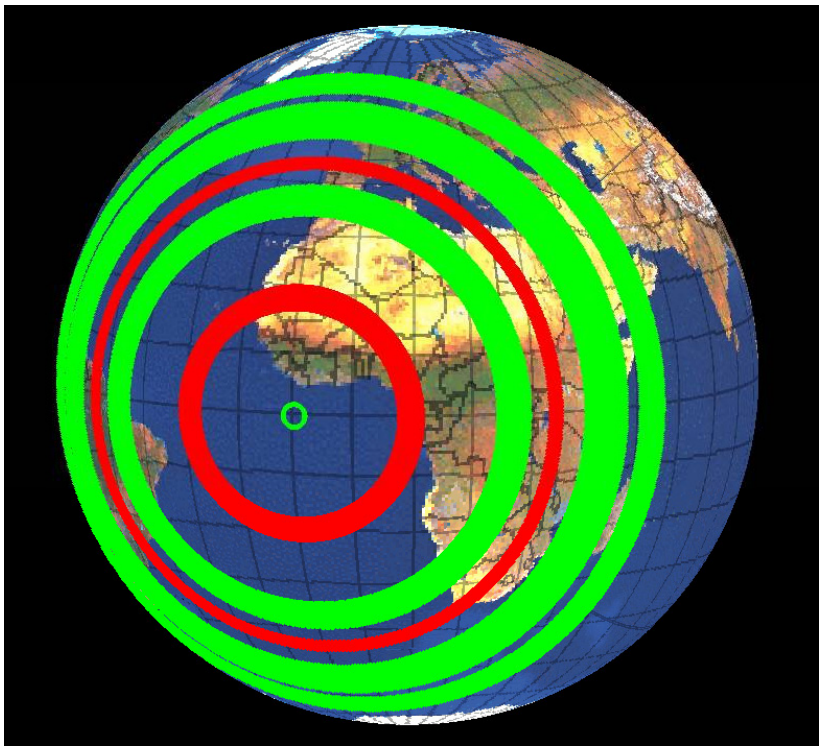

*Fig. 5.23 3D-Dartboard diagram considering a PRF of 104Hz*

## 5.4 Ambiguity analysis for a GeoSAR system

Ambiguity analysis will be another of the key elements to assure the correct performance of any radar system [2]. The ambiguities in range and azimuth axis are related to the antenna shape and dimensions, the processed Doppler bandwidth and other design parameters of the radar such as the PRF.

The ambiguities are originated by echoes that do not correspond to the desired area illuminated by the antenna footprint. The ambiguous echoes can cause image artefacts and misplaced replicas of bright targets. These ambiguities are classified in two categories depending on their origin. On one hand, azimuth ambiguities arise from aliasing caused by the finite sampling of the Doppler spectrum at intervals of the PRF. On the other hand, range ambiguities appear when the echoes from preceding and succeeding pulses arrive at the same time as the desired return. The total power of these ambiguous returns will determine the azimuth ambiguity to signal ratio (AASR) and the range ambiguity to signal ratio (RASR) of the SAR system.

Then, in order to improve the ambiguity to desired signal ratio, the antenna pattern, as well as the PRF, must be adjusted to fulfil the system requirements. So, for a given range and azimuth antenna pattern, it is necessary to select the right PRFs such that the power of the desired signal would be higher enough than the total ambiguous power. On the other way around, for a given range of PRFs, the dimensions and weighting of the antenna must be accurately selected in order to get an antenna pattern that minimizes the ambiguity to signal ratio for the illuminated area. In a first approximation the received ambiguous power can be computed as [2]:

$$P_{amb} = \sum_{\substack{m,n=-\infty \\ m,n\neq 0}}^{\infty} G_{2w}\left( f_{DC} + mPRF, \tau_R + \frac{n}{PRF} \right) \cdot \sigma^0 \left( f_{DC} + mPRF, \tau_R + \frac{n}{PRF} \right) \quad (5.43)$$

From (5.43), the dependency of the ambiguous returns with the PRF is clearly demonstrated. The desired power received from one point, determined by its Doppler frequency shift ( $f_{DC}$ ) and the time delay of the received echo ( $\tau_R$ ), is calculated multiplying the two way power antenna pattern ( $G_{2w}$ ) by the surface reflectivity ( $\sigma^0$ ) [14] of the desired target. On the other hand, the total ambiguous power received for a given Doppler frequency and a time delay point will be calculated as the summation of the echoes from preceding and succeeding pulses, represented in (5.43) with the *n*-index ( $n / PRF$ ); and the power of the replicas of the Doppler spectrum, which correspond to the *m*-index of the summation ( $m \cdot PRF$ ). This power will mask the desired part of the spectrum. Obviously, the summation index *m=n=0* must be ignored in the ambiguous power computation because it corresponds to the desired return. So, using (5.43), the integrated ambiguity to signal ratio (ASR) for a given processed Doppler bandwidth ($B_p$) can be computed as [2]:

$$ASR(\tau) = \frac{P_{amb}}{P_u} = \frac{\sum_{\substack{m,n=-\infty \\ m,n\neq 0}}^{\infty} \int_{-Bp/2}^{Bp/2} G_{2w}\left( f_{DC} + mPRF, \tau_R + \frac{n}{PRF} \right) \cdot \sigma^0 \left( f_{DC} + mPRF, \tau_R + \frac{n}{PRF} \right) df}{\int_{-Bp/2}^{Bp/2} G_{2w}(f,\tau) \cdot \sigma^0(f,\tau)\, df} \quad (5.44)$$

Unfortunately, (5.44) is not handy for spaceborne SAR imaging since it requires the knowledge of the azimuth-range antenna pattern, while most specifications of the antenna are given by their azimuth or range cuts separately. For this reason, to facilitate the computation of the ASR, it is possible to separate the ambiguities in azimuth and range, calculating them independently [2]. In the following sections the effects of azimuth and range ambiguities will be analysed to see their impact in the GeoSAR operation.

### 5.4.1 Range Ambiguity to Signal Ratio (RASR)

As it was previously introduced, range ambiguities are the result of echoes from preceding and succeeding pulses that arrive at the same time that desired return at the antenna. The Range Ambiguity to Signal Ratio (RASR) will be computed as the quotient between the total power received from these ambiguous echoes and the power from the desired target.

In Fig. 5.24, a simple diagram illustrates the origin of range ambiguities. In the figure, the zone of interest is identified as a yellow strip on the ground. The antenna illuminates this zone but the side lobes can receive echoes from further or nearer distances. The antenna pattern in range is plotted in blue in the figure. As it can be seen, the main beam points to the centre of the scene while the side lobes are illuminating undesired zones.

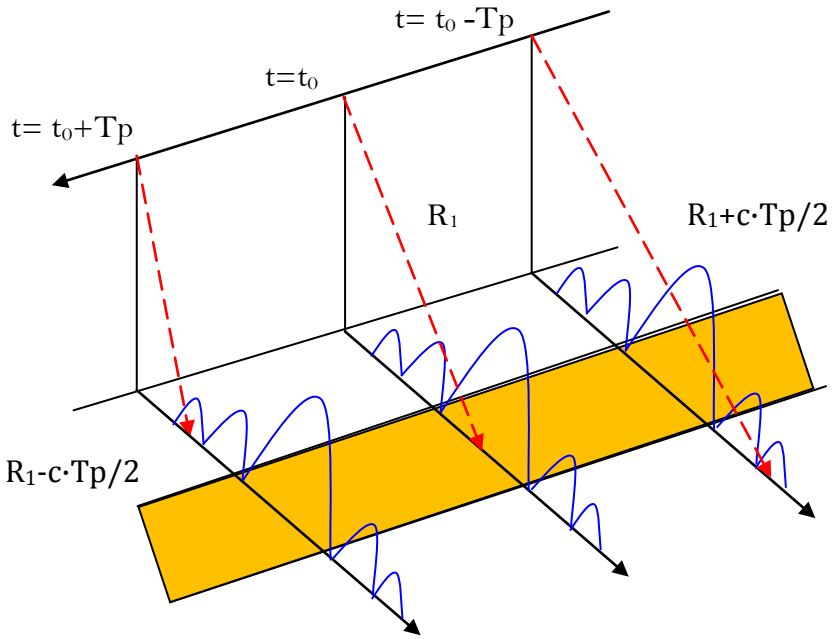


*Fig. 5.24 Origin of range ambiguities in SAR systems*

In Fig. 5.24, the desired pulse is send at $t_0$, so the echo will arrive to the antenna at $t_1 = t_0 + 2R_1/c$, where $R_1$ is the distance to the middle of the swath. The pulses that will cause higher ambiguous returns are sent at times $t_0 - T_p$ and $t_0 + T_p$, where $T_p$ is the inverse of the PRF (also known as Pulse Repetition Interval or PRI). The returns from the desired scene of these pulses, will arrive at $t_0 + 2R_1/c - T_p$ and $t_0 + 2R_1/c + T_p$, so these echoes would not affect to the desired signal. However, the radar is illuminating further

and nearer zones than the desired scene. So, for the previous emitted pulse, a return from a target placed at $R_2 = R_1 + cT_p/2$ will be received at:

$$t_2 = t_0 - T_P + \frac{2R_2}{c} = t_0 - T_P + \frac{2\left(R_1 + \frac{cT_p}{2}\right)}{c} = t_0 + \frac{2R_1}{c} \tag{5.45}$$

Consequently, the echo of this point will arrive at the same time than the desired pulse since $t_2 = t_1$ and it will be considered as an ambiguous return. With a similar reasoning, the ambiguous distances for succeeding pulses can be determined. Considering a target situated at distance $R_3 = R_1 - cT_p/2$ and knowing that the pulse will be sent at $t_0 + T_p$, in (5.46) is demonstrated that it will be an ambiguous zone.

$$t_3 = t_0 + T_P + \frac{2R_2}{c} = t_0 + T_P + \frac{2\left(R_1 - \frac{cT_p}{2}\right)}{c} = t_0 + \frac{2R_1}{c} \tag{5.46}$$

However, not only the adjacent pulses will cause ambiguous returns. It is necessary to consider previous and succeeding pulses to do a complete analysis of the range ambiguities. In order to obtain the location of the ambiguous zones of a point situated at $R_1$ equation (5.47) is used:

$$R_{amb} = R_1 \pm n\frac{cT_p}{2} \qquad n = \pm 1, \pm 2 \ldots n_h \tag{5.47}$$

where $n$ is an integer that represents the pulse number (0 for desired pulse, negative for succeeding pulses and positive for previous ones) and $n_h$ is the number of pulses considered in RASR computation. Theoretically, the number of pulses is large, but in practise when $n$ increases the distance increases as well and the antenna gain at such angles decreases considerably, so the received power will be insignificant for large values of $n$.

Once the ambiguous distances are determined, the RASR can be calculated from the radar equation (5.48), where the constant values will not have interest in the computation because they will be in the numerator and denominator of the ratio. So, finally, the required parameters to compute the range ambiguities will be the incidence angle and the backscattering coefficient of the illuminated surface, as well as the ambiguous distances of these pulses determined by (5.47). Also, the weighting of the antenna diagram in range will be necessary to compute the total RASR.

$$P_r = \frac{P_t G_t G_r \sigma^0 S \lambda^2}{(4\pi)^3 R^4 L} = \left(\frac{P_t G_t G_r \sigma^0 \lambda^2}{(4\pi)^3 R^4 L}\right)\left(R_0 \theta_{az}\right)\left(\frac{c\tau_0}{2\sin\theta_{in}}\right) = K\frac{G_t G_r \sigma^0}{R^3 \sin\theta_{in}} \tag{5.48}$$

Then, the RASR for each point can be determined by taking the power of all ambiguous returns from the previous and succeeding echoes, and the desired power. Taking the ratio between these powers the RASR will be:

$$RASR = 10\log_{10}\left(\frac{P_{amb}}{P_d}\right) \tag{5.49}$$

The desired power ($P_d$) received at the radar is obtained from (5.50) without considering the constant parameters which will be cancelled in (5.49). The total ambiguous power ($P_{amb}$) will be computed with (5.51).

$$P_d = \frac{\sigma^0(\theta_{in})G_tG_r}{R^3\sin(\theta_{in})} \tag{5.50}$$

$$P_{amb} = \sum_{\substack{n=-n_h \\ n\neq 0}}^{n_h} P_{amb}^{+} + \sum_{n=-n_h}^{n_h} P_{amb}^{-} = \sum_{\substack{n=-n_h \\ n\neq 0}}^{n_h} \frac{\sigma^0(\theta_{ian})G_{Tn}^{+}G_{Rn}^{+}}{R_{amb_n}{}^3\sin(\theta_{ian})} + \sum_{\substack{n=-n_h \\ n\neq 0}}^{n_h} \frac{\sigma^0(\theta_{ian})G_{Tn}^{-}G_{Rn}^{-}}{R_{amb_n}{}^3\sin(\theta_{ian})} \tag{5.51}$$

where $\theta_{in}$ is the incidence angle of the desired return while $\theta_{ian}$ is the incidence angle for the *n*th ambiguous pulse, $\sigma^0(\theta_{ian})$ is the backscattering coefficient at each incidence angle and $G_t, G_r$ are the antenna pattern in transmission and reception. Finally, the terms $P_{amb}^{+}$ and $P_{amb}^{-}$ stand for the total ambiguous power in the pointing direction and the opposite side considering a side-looking radar illumination.

As it has been commented, the PRF is one of the important elements on any SAR system implementation. In the previous section, we have seen that the PRF choice should avoid transmission and/or nadir interferences. However, the PRF has also to be selected thinking on the ambiguity level requirements. In the following examples it is shown how the PRF affects to the RASR. However, the level of range ambiguities is expected to be low due to the low PRF at which the GeoSAR system will usually work.

Let's take as a first example a GeoSAR system working at very-low PRF (7 Hz) and a desired scene at incidence angles from 49 to 54 degrees. As it can be seen in Fig. 5.25, only the zone at same incidence angle but at the opposite illumination direction will be ambiguous to the radar at those small PRFs. Then, considering an approximated *sinc* shape antenna pattern, this zone is more than 70 dB below the desired scene illumination. Consequently, the RASR level obtained for this configuration will be really good (acceptable values for RASR in a LEO SAR system are around the -20dB). In this example, as it is shown in Fig. 5.26, RASR better than -70dB is obtained.

It is difficult to obtain such results in a real system since the antenna pattern will not have the theoretical behaviour presented by the *sinc* function considered in this analysis but it is a good academic example to see the feasibility, regarding the range ambiguities, of a geosynchronous satellite for SAR applications.

To see the problems that higher PRF may cause to GeoSAR acquisition, a system working at a PRF of 100Hz will be considered as a second example. As it has been seen in section 5.3, such PRF will not be feasible for a GeoSAR configuration due to the nadir and transmission interferences. However, in this section, this PRF has been taken as an upper limit for GeoSAR operation in order to see the RASR level considering an extreme value

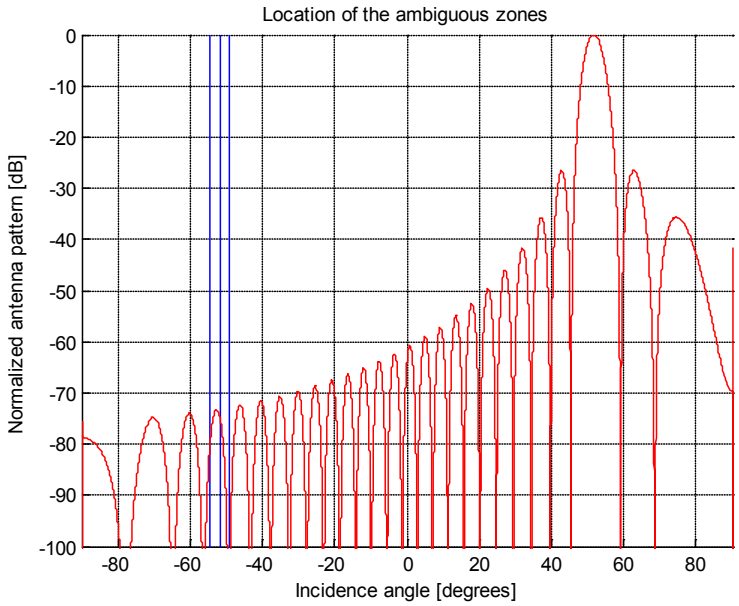


*Fig. 5.25 Range ambiguous zones for GeoSAR at very-low PRF of 7Hz*

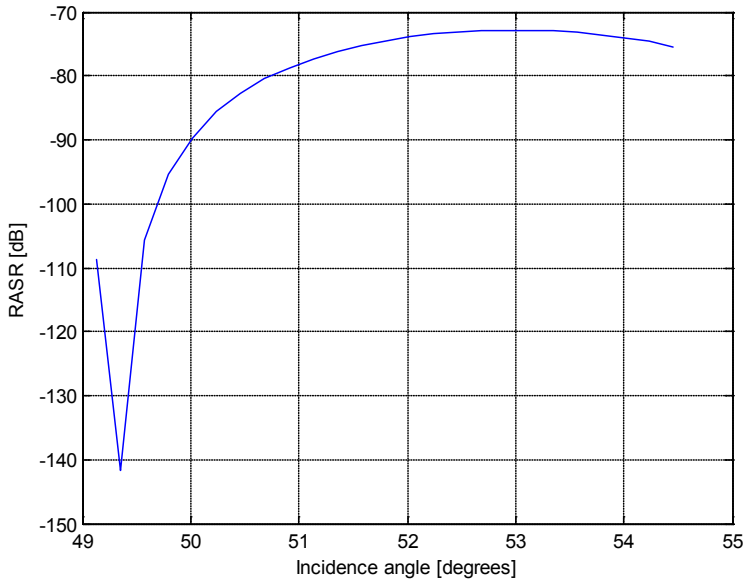


*Fig. 5.26 RASR for GeoSAR at 7Hz for incidence angles between 49 and 54 degrees*

of the PRF. The location of the ambiguous zones for this PRF is denser than in the previous case and, consequently, the level of RASR gets worse since more ambiguous zones have to be considered. The location of the ambiguous zones and the RASR levels obtained are presented in Fig. 5.27 and Fig. 5.28. In this case, the RASR levels are under the -30dB still really good for SAR application. Therefore, it has been verified that the range ambiguities will not be a problem for SAR acquisition since such systems usually works at very low PRF (under 50 Hz).

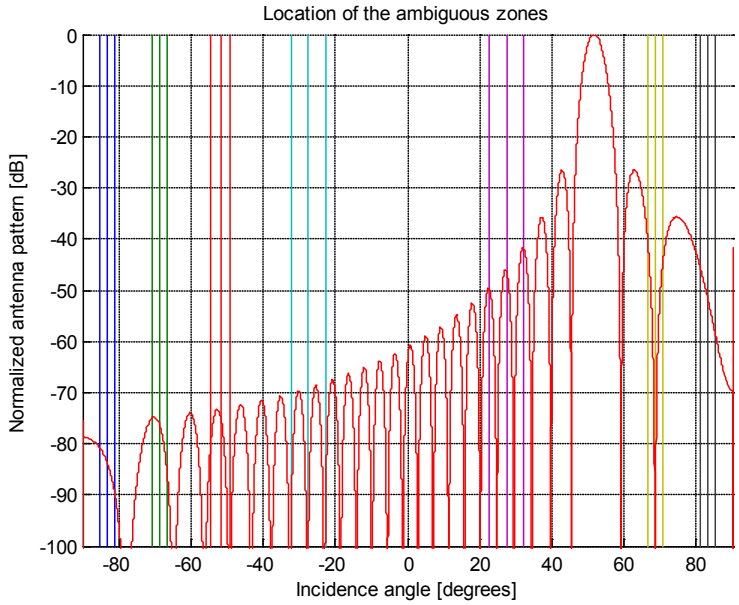


*Fig. 5.27 Range ambiguous zones for GeoSAR at high PRF of 100Hz*

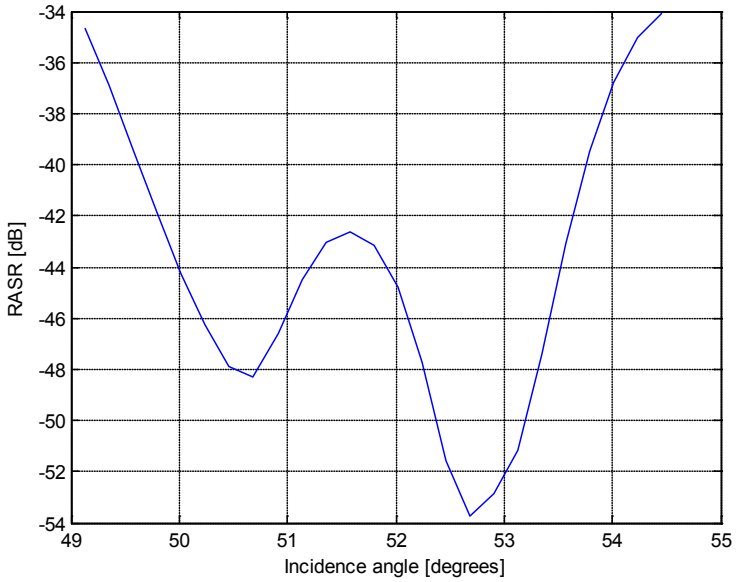


*Fig. 5.28 RASR for GeoSAR at 100Hz for incidence angles between 49 and 54 degrees*

### 5.4.2 Azimuth Ambiguities to Signal Ratio (AASR)

Azimuth ambiguities arise from the finite sampling of the azimuth antenna pattern each inverse of the PRF. It is easy to understand if the problem is defined in time domain. Every PRI seconds the radar sends a pulse to the scanned area which is scattered by the

ground surface and returns to the antenna. This produces that each point of the illuminated scene is seen by the radar as a collection of a discrete burst as shown in Fig. 5.29

In Fig. 5.29, the radar is flying left to right illuminating a point target. The satellite movement is continuous, but in the figure there are only drawn the positions every 1/PRF. In each of these points, the radar sends a finite duration pulse that illuminates the point with the corresponding weighting of the antenna diagram. For this reason, in the bottom of the picture, the azimuth antenna diagram sampled in time is shown as the target response since the radar only receives information about the target every 1/PRF. This temporal sampling will produce an aliasing on the frequency domain in the received Doppler spectrum of the target. As it is plotted in Fig. 5.29 and analytically demonstrated on the following lines, ambiguous replicas at multiples of the PRF appear in the frequency response of the target.

Once the origin of the azimuth ambiguities has been explained, they may be studied analytically in order to determine how these ambiguous zones of the Doppler spectrum affect to the radar operation. To calculate the contamination of the ambiguous signal to the desired return, it will be useful to work in frequency domain. In order to obtain the spectrum of the received signal, it is necessary to compute the Fourier transform of the sampled azimuth antenna pattern. First of all, the time evolution of the power received from a point target as the one on Fig. 5.29 can be expressed as:

$$P(\tau) = P_0 \sum_n G^2(\tau) \cdot \sigma^0(\tau) \cdot \delta\left(\tau \pm \frac{n}{PRF}\right) \tag{5.52}$$

where $P_0$ is the maximum power received in the centre of the antenna main beam, $G^2(\tau)$ is the two way azimuth antenna pattern and $\sum \delta(\tau \pm n/PRF)$ is an impulse train that simulates the sampling of the AAP. It is possible to approximate the returns as *Dirac's delta* function since the duration of the pulses is much shorter than the inter-pulse period. $\sigma^0(\tau)$ is the target reflectivity. From now on, in this analysis a uniform backscattering model for the targets in azimuth and range cuts will be assumed, so $\sigma^0(\tau)$ becomes constant and it will not have interest in the ratios computation. To calculate the Fourier Transform of equation (5.52), the Fourier Transform of the impulse train is necessary [15]:

$$F.T.\left\{\sum_n \delta\left(\tau \pm \frac{n}{PRF}\right)\right\} = \sum_k \delta(f \pm k \cdot PRF) \tag{5.53}$$

Then, from (5.53) the spectrum of the discrete target response in the frequency domain can be obtained as:

$$\begin{aligned} F.T.\{P(\tau)\} &= F.T.\left\{P_0 \sum_n G^2(\tau) \cdot \delta\left(\tau \pm \frac{n}{PRF}\right)\right\} = P_0 \sum_n F.T.\left\{G^2(\tau) \cdot \delta\left(\tau \pm \frac{n}{PRF}\right)\right\} = \\ &= P_0 \sum_n F.T.\{G^2(\tau)\} * F.T.\left\{\delta\left(\tau \pm \frac{n}{PRF}\right)\right\} = P_0' G^2(f) * \sum_n \delta(f + n \cdot PRF) = \\ &= P_0' \sum_n G^2(f + n \cdot PRF) \end{aligned} \tag{5.54}$$

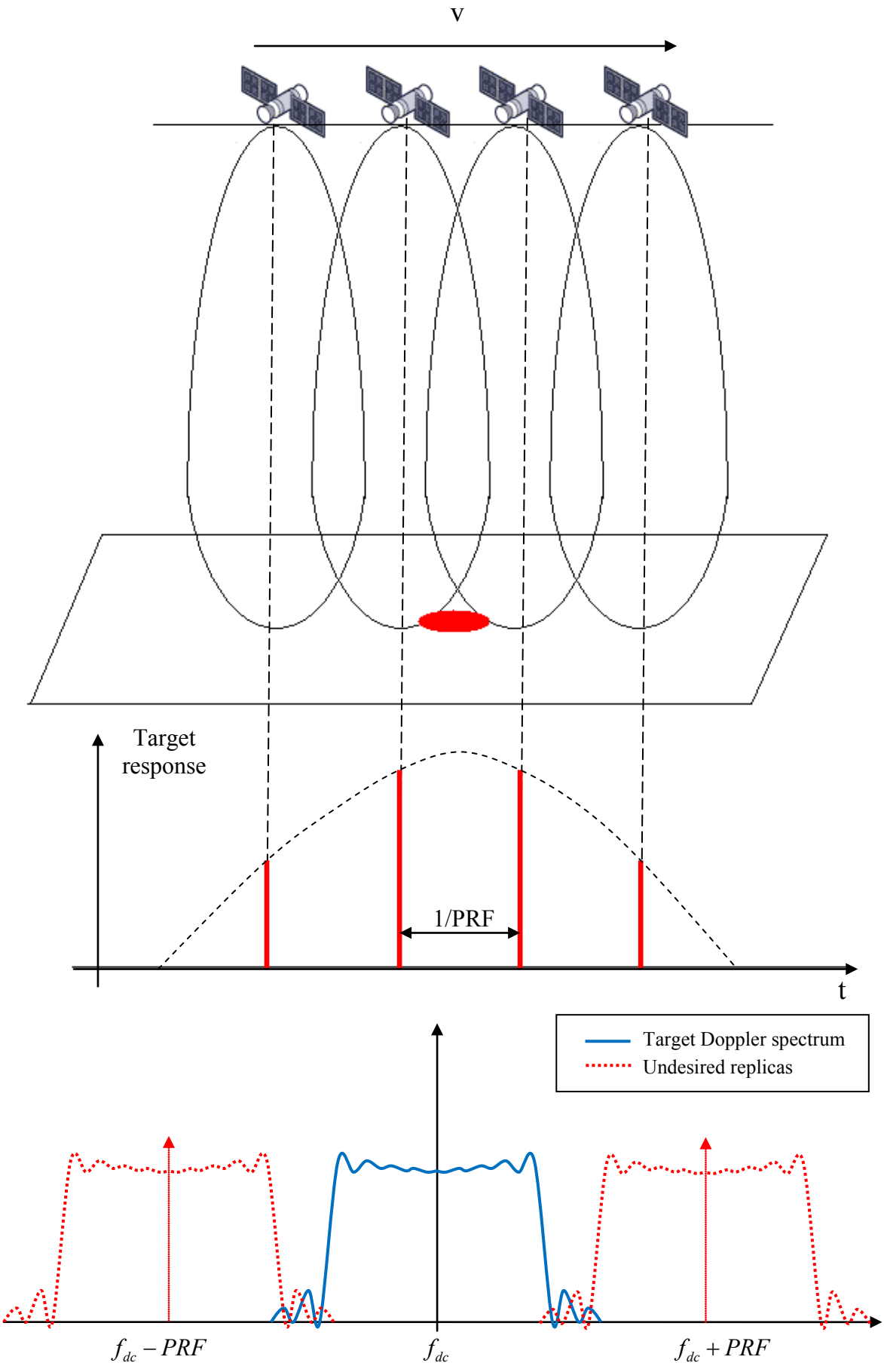


*Fig. 5.29 AAP quantization due to discrete pulse emission. Azimuth ambiguities origin*

Finally, to get the spectrum of the received signal the AAP must be defined in function of the Doppler frequency. The one-to-one relationship between azimuth time and Doppler frequency can be obtained for a linear SAR easily as:

$$f_d = \frac{2v_e{}^2\tau}{\lambda R_0} \tag{5.55}$$

However, for more complex situations, this approximation would not be accurate enough since the linearity of the trajectory is completely lost. Taking the simple cases of the GeoSAR acquisition (linear trajectories at approximately constant velocity), the shape of the azimuth spectrum of the signal will be the same than the two-way power antenna pattern in the time domain given the linear relation between azimuth slow time and Doppler frequency shown in (5.55). It is important to remember that a uniform backscattering model is used. If not, the spectrum should be calculated as the convolution between the two-way azimuth antenna pattern and the backscattering model considered. So, the azimuth antenna pattern can be written in terms of the Doppler frequency (using a uniform aperture approximation) as:

$$G^2\left(f_d\right) = G_0 \cdot \mathrm{sinc}^4\left(\frac{Lf_d}{2v_e}\right) \tag{5.56}$$

Once the spectrum of the received signal is defined, the azimuth ambiguities can be computed. The azimuth ambiguity to signal ratio (AASR) is the relation between the summation of the ambiguous zones of the spectrum in the Doppler bandwidth processed divided by the desired power.

The desired integrated power in the receiver can be expressed as in (5.57), where $B_p$ is the Doppler processing bandwidth, $W_{ai}(f)$ is the processing window in the receiver and $G_{2az}$ is the azimuth two-way antenna pattern in the Doppler frequency domain.

$$P_d = \int_{-Bp/2}^{Bp/2} W^2{}_{ai}\left(f_d\right)\frac{G_{2az}\left(f_d\right)}{G_{2azMAX}}df_d \tag{5.57}$$

On the other hand, the ambiguous signal that interferes in the desired Doppler bandwidth can be obtained as:

$$P_{amb} = \sum_{m\neq 0}\int_{-Bp/2}^{Bp/2} W^2{}_{ai}\left(f_d\right)\frac{G_{2az}\left(f_d + mPRF\right)}{G_{2azMAX}}df_d \tag{5.58}$$

Finally, using (5.57) and (5.58) the AASR is calculated as the ratio between them:

$$AASR = 10\log_{10}\left(\frac{P_{amb}}{P_d}\right) = 10\log_{10}\left(\frac{\sum_{m\neq 0}\int_{-Bp/2}^{Bp/2} W^2{}_{ai}\left(f_d\right)\frac{G_{2az}\left(f_d + mPRF\right)}{G_{2azMAX}}df_d}{\int_{-Bp/2}^{Bp/2} W^2{}_{ai}\left(f_d\right)\frac{G_{2az}\left(f_d\right)}{G_{2azMAX}}df_d}\right) \tag{5.59}$$

This is the theoretical way to compute the AASR. Fortunately, the number of critical ambiguities, represented by index *m*, is not infinite because the AAP decays to negligible values when the Doppler frequency increases sufficiently. In practise, we will analyse the ambiguities for a finite number of ambiguities, which is a reasonable approximation to the exact result.

The AASR is extremely related to the Doppler bandwidth processed and the shape of the azimuth antenna pattern. In the GeoSAR case, this bandwidth will be much lower than the PRF. Therefore, the replicas in the spectrum will be separated enough to have a reasonable level of the AASR that will not mask or deteriorate the final image. Since the huge number of possible configurations that the geosynchronous satellites offers to perform the synthetic aperture, one simple case will be analysed to see the expected level of azimuth ambiguities for a GeoSAR system.

Let's take a perfect geosynchronous orbit with small perturbations in the eccentricity. As it has been demonstrated in the first example of section 5.1, a satellite track over the Equator is obtained. For an eccentricity of 0.0004, the maximum length of the synthetic aperture achieved was 67.4 Km in 12 hours. These values would give a mean relative velocity of the platform with respect the rotating Earth's surface of about 1.5 m/s. On the other side, a scene of 200 Km in azimuth placed at 37000 Km from the satellite will be considered. With those parameters an antenna length of 7.5 meters will be necessary (taking the azimuth angle of the antenna as $0.8 \cdot \lambda / L$). Then, considering the azimuth antenna pattern in time domain given by the equation (5.56), a pattern as the one shown in Fig. 5.30 is obtained.

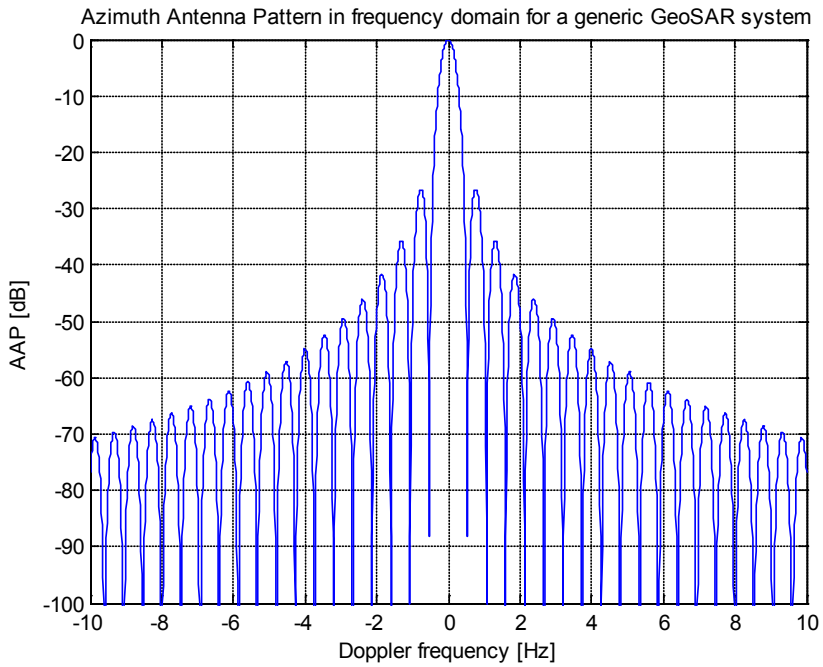


*Fig. 5.30 AAP in frequency domain considering the typical parameters of a GeoSAR system*

As it can be seen, the processing Doppler bandwidth for a GeoSAR system will be really small due to the low relative motion between the satellite and the scene and the long distances where the satellite is orbiting. Although the small PRFs considered in the GeoSAR systems (less than 50 Hz), the level of RASR will be really good since, as it can be seen in Fig. 5.30, for Doppler shifts greater than 1 Hz, the pattern has felt more than 30dB.

So, considering a processing bandwidth of 0.4 Hz and working at a PRF of 5 Hz, the AASR obtained is shown in Fig. 5.31. In this case, the AASR is under the -55dB which is a nice result for azimuth ambiguities.

If the PRF is reduced and an extremely low value of 1 Hz is considered (in this case lower values will not be feasible in order to fulfil the Nyquist criteria of minimum PRF of twice the processing bandwidth). The results obtained with this small PRF are given in Fig. 5.32. In this case, the level of AASR is worse than in the previous example as it was expected. However, it is still under the -20dB which can be considered an acceptable of ambiguity for a SAR system.

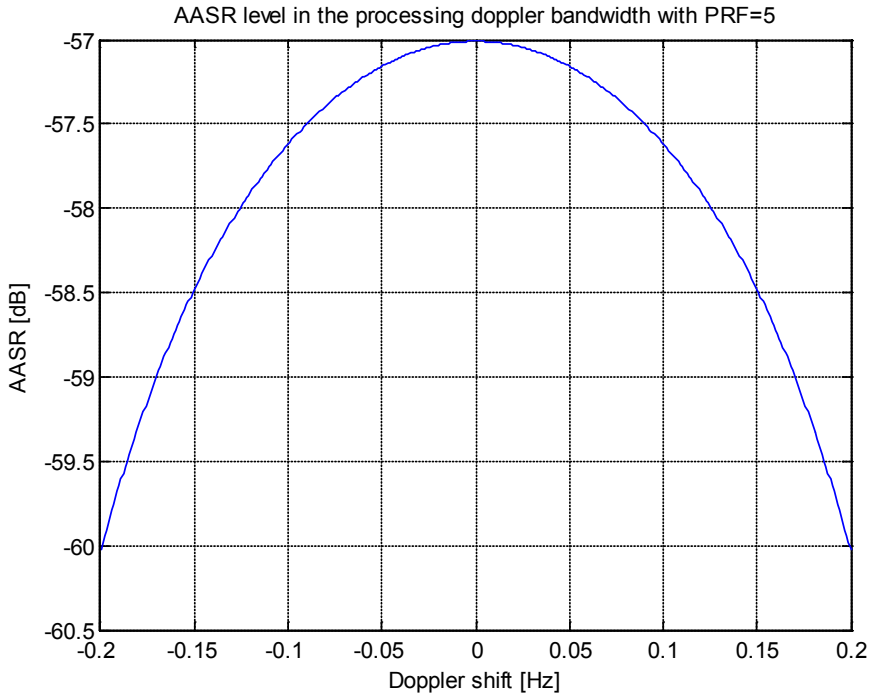


*Fig. 5.31 AASR for a particular GeoSAR acquisition at PRF=5 Hz. Levels under the -50dB are obtained with this configuration*

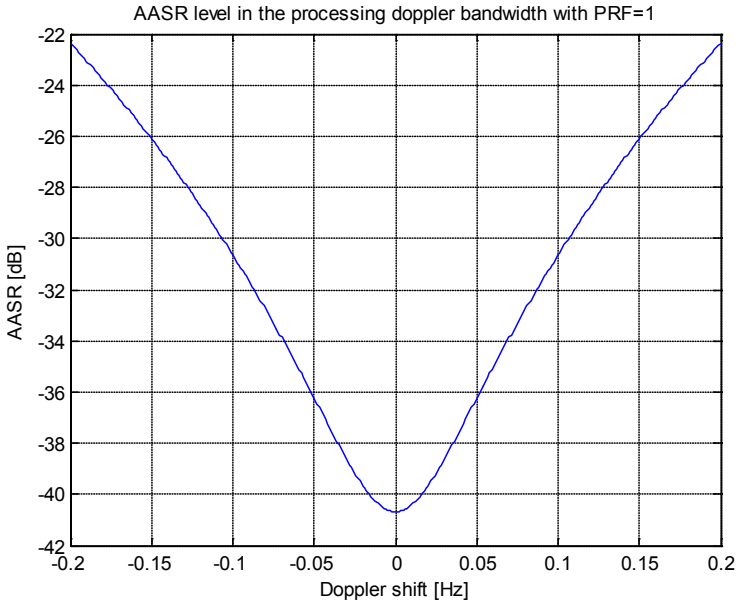


*Fig. 5.32 AASR for a GeoSAR configuration considering an extreme low PRF value of 1Hz. Worse results are obtained but they are still under the -20dB which is acceptable in SAR acquisition*

As it has been seen, the small Doppler bandwidth considered in the acquisition due to the slow satellite relative motion makes that even the low PRFs considered in the GeoSAR acquisition, the level of AASR will be low and will not cause any problem or artefacts in the SAR images. Once again, the results shown in the previous example have been obtained using a nice *sinc* shape antenna pattern. In a real situation, these results could be a bit worse, but anyway, the expected AASR levels will be in the similar levels.

# Chapter 6 Preliminary Doppler Analysis

In this section, the Doppler history of an scene placed over the Earth's surface will be analysed in function of the satellite orbit ephemerides and timing parameters of the acquisition. The Doppler bandwidth of the imaged scene will be essential to determine the minimum PRF of the system in order to satisfy the Nyquist criteria. The Doppler centroid evolution, Doppler bandwidth and the methodology used to process the received signal will be studied in this section.

## 6.1 The Doppler Effect importance in SAR acquisition

The Doppler Effect is a phenomenon that modifies the apparent received frequency when transmitter and receiver are moving one with respect to the other. It is not the purpose of this report to give a complete analysis and derivation of the precedence of the Doppler, but the basic formulas which affect to the SAR acquisition will be given in this section.

The Doppler shift appreciated at any system with the transmitter and/or the receiver in motion can be computed as:

$$f_d = -\frac{2}{\lambda}\frac{\partial R}{\partial t} \tag{6.1}$$

where $\partial R/\partial t$ is the derivative of the slant range between the satellite an the targets in function of the time. This term is equivalent to the radial velocity towards the line of sight direction. In the common LEO SAR systems with linear satellite path, the Doppler history of the different targets follows a linear behaviour, starting from positive values, decreasing until it reaches zero Doppler shift when the target position is perpendicular to the satellite velocity and, then, increasing negatively until the target goes out of the antenna processing beam. However, the non-linear motion characteristic of the GeoSAR systems makes difficult to predict the Doppler evolution and it is not possible to give a simple formulation for this phenomenon.

Anyway, the Doppler history of targets, and more concretely the Doppler bandwidth, will be determinant to the SAR performance in terms of azimuth resolution. The azimuth resolution can be related to the Doppler bandwidth of the acquired signal in a LEO satellite as:

$$\rho_{az} = \frac{v_{sat}}{B_d} \tag{6.2}$$

In the following section, the Doppler bandwidth for a GeoSAR system is studied and compared with the one obtained from a LEO SAR. As it will be explained, the Doppler bandwidth is related to the orbital ephemerides of the satellite since they will govern the relative motion between the scene and the satellite.

## 6.2 Doppler history in a GeoSAR system

In a GeoSAR system, the Doppler history of the targets will be quite different from the one obtained by a linear LEO SAR acquisition. The non-constant radius of the orbit will add a Doppler component to the common along track motion of the LEO satellites. This frequency shift produced by the radius changes will not be of our interest in the SAR processing since it is a common shift for all the targets in the scene and, consequently, it can not be used to discriminate the different targets on the azimuth direction. It only adds a non-constant Doppler centroid to the raw data acquisition. So, the Doppler bandwidth in the antenna beam from the different targets of the desired scene will be the one used to process the received signal.

In Fig. 6.1, the Doppler history of 100 by 100 Km scene placed over Barcelona and illuminated by a geosynchronous satellite at 10ºW with an eccentricity of 0.0004 and inclination of 0.046 degrees is presented. As it can be observed, the Doppler bandwidth is really high if the whole motion of the satellite is considered. In the example of the Fig. 6.1, a bandwidth of 165Hz is obtained if no Doppler centroid compensation is considered. Such Doppler bandwidth would require a minimum PRF above the 300Hz to fulfil the Nyquist criteria. However, as it has been presented in sections 5.3 and 5.4, high PRF (over 150Hz) will produce small imaging free nadir eclipses windows and the level of ambiguities will rise up to undesirable levels.

Fortunately, this Doppler bandwidth is not strictly required in the SAR acquisition. The Doppler shift behaviour, presented in Fig. 6.1, is mainly governed by the satellite orbital radius variation. If the Doppler history is zoomed in, as it is plotted in Fig. 6.1, a range of frequencies can be appreciated at each time. The useful Doppler bandwidth to be processed in the receiver is the one marked by the green arrow of the Fig. 6.1. Therefore, the common part of the Doppler must be compensated in such a way that only the relative Doppler between the targets in the scene would be considered.

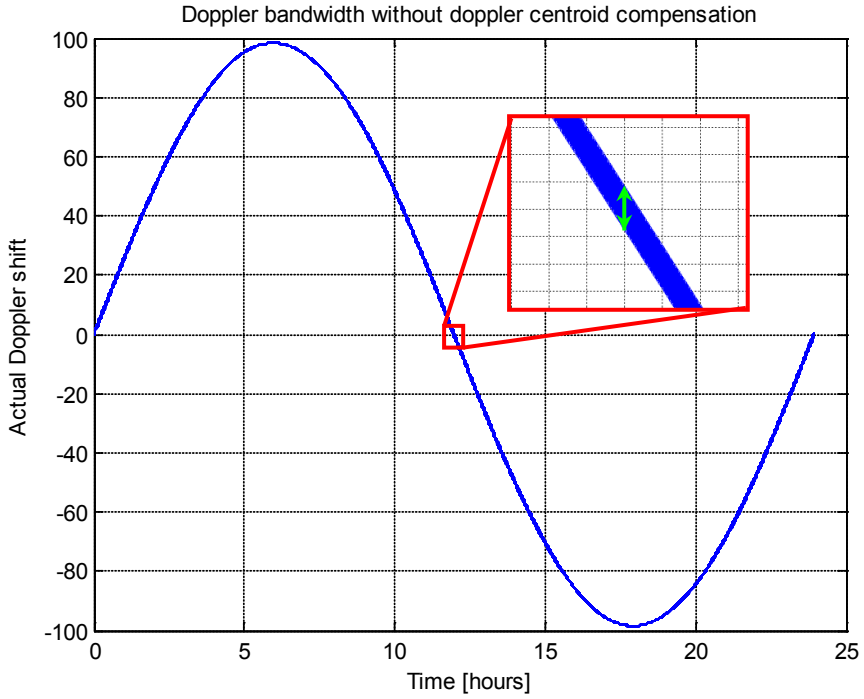


*Fig. 6.1 Doppler history of targets from a scene of 100 by 100 Km*

The Doppler shift behaviour will strongly depend on the GeoSAR configuration (monostatic or bistatic) and the orbital parameters of the satellite/s. So, it is not easy to find a closed formula to easily compute the associated bandwidth to a GeoSAR acquisition as in LEO satellite. However, some approximations can be done in order to find an equation for very concrete GeoSAR configurations.

Let us consider a simpler case with a monostatic GeoSAR configuration with a single satellite placed at 2.11ºE. The orbital plane of the satellite is determined by an eccentricity

of 0.0004 and no inclination. The satellite will work at 12GHz. A scene at the same meridian is considered and at a latitude of 41ºN (a place around Barcelona). In this case, as it has been deeply explained in section 5.1, the satellite track will describe a straight trajectory over the Equatorial line. The situation is schematically represented in Fig. 6.2.

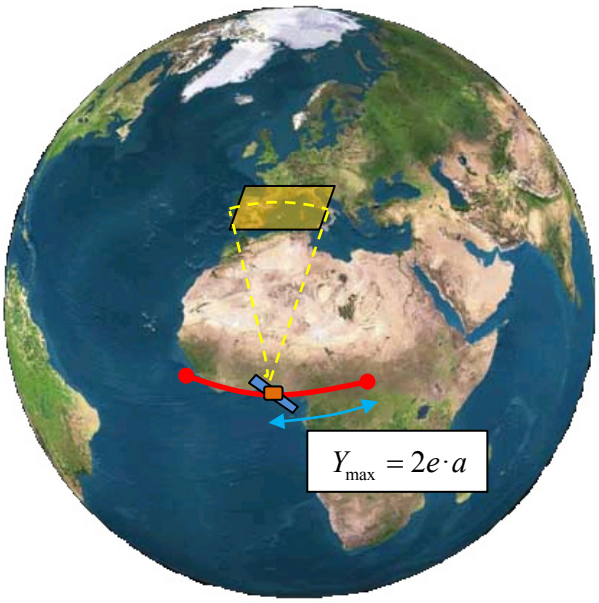


*Fig. 6.2 Doppler bandwidth computation for a slightly eccentric orbit*

As it has been analytically computed in section 5.2, the synthetic aperture of the satellite with respect to the target can be obtained as in (5.29). So, the maximum left-right displacement of the satellite will be obtained as the half of the achieved synthetic aperture length:

$$Y_{\max} = 2e \cdot a \sin\left(\Omega_E \frac{T_i}{2}\right) \tag{6.3}$$

Being $e$ the orbit eccentricity, $a$ the semi-major axis of the orbit ellipse, $\Omega_E$ the Earth's rotation angular velocity and $T_i$ the integration time. From this maximum along track motion, the maximum Doppler bandwidth received from the scene can be computed as:

$$B_d = 2\Omega_E \frac{Y_{\max}}{\lambda} = 4\Omega_E \frac{e \cdot a}{\lambda} \sin\left(\Omega_E \frac{T_i}{2}\right) \tag{6.4}$$

If the previous formula is particularized for the orbital and signal parameters previously commented and for an integration time of 4 hours, a Doppler bandwidth of 98.63Hz is obtained. If this result is compared with the simulated results using this configuration, they are quite consistent since the simulated Doppler bandwidth which is around 97.31Hz.

So, this approximation is valid for time intervals where the Doppler history presents a quasi-linear behaviour. Therefore, looking at Fig. 6.1, (6.4) would be correct around the

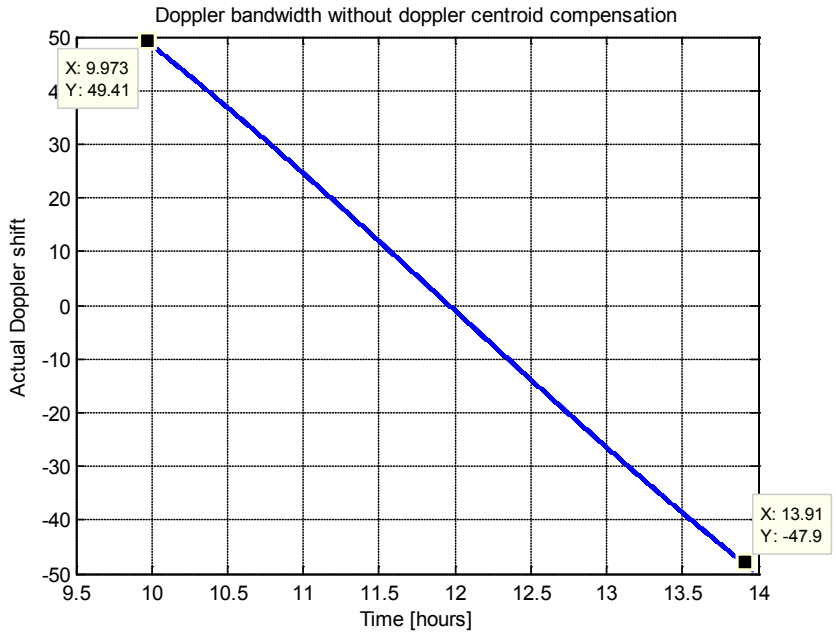


*Fig. 6.3 Doppler bandwidth considering 4 hours of integration time*

time interval from hour 9 to 15. On the other hand, it would not have any sense at intervals with maximum Doppler shift, around hours 6 or 18. However, it is only valid for this particular configuration. More complex cases should be studied concretely by simulation in order to obtain the actual Doppler bandwidth. In the next section, the Doppler bandwidth compensated with the Doppler centroid for each emitted pulse is analysed. The compensated Doppler bandwidth will be the one used in reception to process the raw data from the scene.

## *6.3 Doppler centroid track and compensation*

In any SAR system, the Doppler shift is essential to distinguish two targets at the same range whose echoes arrive to the receiver at the same time. However, the Doppler bandwidth computed in the previous section was not useful in SAR processing since it takes into account common Doppler shifts that affect in the same way to all the targets in the scene.

Therefore, only the relative Doppler shifts between all the points of the scene have to be considered. From this relative shifts, the useful Doppler bandwidth will be obtained. In order to get the desired Doppler bandwidth from the actual one, the received signal has to be compensated by the Doppler shift of the central point of the scene (or anyone else) in order to get the relative Doppler from this point. This Doppler centroid tracking and compensation will give as a result a lower Doppler bandwidth to be processed which will require a smaller PRF to accomplish Nyquist.

Let's see how affects the Doppler centroid compensation into the received Doppler Bandwidth of the example presented in the previous section (target at 41ºN 2.11ºE and

satellite at 0ºN 2.11ºE). For each emitted pulse, the position and radial velocity of the satellite with respect to the central point of the scene have been computed in order to track the Doppler centroid. This Doppler centroid has been directly subtracted from the previous computed Doppler and the results presented in Fig. 6.4 have been obtained. As it can be seen, the Doppler bandwidth of the scene relative to the central point is smaller (around 0.5 Hz). It means that even PRF around 1 Hz can be considered in the acquisition, which is desirable to reduce the ambiguity level and avoid transmission interferences or nadir eclipses.

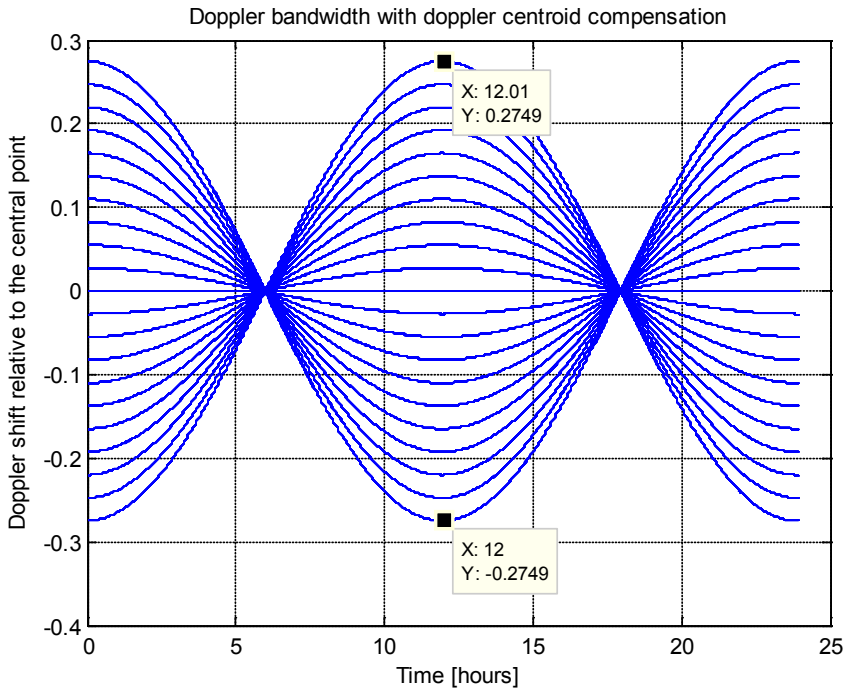


*Fig. 6.4 Doppler bandwidth compensated with the Doppler of the central point (scene of 100x100 Km)*

Therefore, the bandwidth after the Doppler centroid compensation will be the one that will affect to the image resolution. So, for a GeoSAR acquisition with no linear trajectory, the Doppler centroid history must be taken into account in the reconstruction algorithms in order to get precise results as it will be seen in Chapter 8.

# Chapter 7 Power link budget: Signal to Noise requirements

The large distances where the geosynchronous satellites are orbiting make the received echo power one of the critical issues on the GeoSAR acquisition. The path loss, working at ranges around 37,000 Km, will be tens of dBs larger than in the typical LEO SAR systems. Such deterioration of the received power only can be compensated by increasing the integration time or worsening the ground resolution for distributed targets if moderate transmitted powers and medium-sized antennas, as in a LEO SAR system, are considered. Therefore, in this section the Signal to Noise Ratio (SNR) for different GeoSAR configurations will be analysed and the acquisition parameters will be adjusted to reach a reasonable SNR levels after SAR processing.

## *7.1 Link budget analysis: Signal to Noise Ratio and SAR processing*

First of all, a brief summary with the Signal to Noise considerations is presented in order to clarify all the parameters of the final SNR equation. The idea is to obtain the SNR of a radar system which uses pulse compression and synthetic aperture techniques in the acquisition. So, as a first step, the signal to noise ratio for a single pulse transmitted by the radar is given by the well-known radar equation [2]:

$$SNR_1 = \frac{P_t G_t A_r \sigma}{(4\pi)^2 R_t^2 R_r^2 k T_0 B_P F_n} \frac{1}{L_T} \tag{7.1}$$

where $P_t$ is the radar transmitted power, $G_t$ is the transmitter antenna gain, $A_r$ is the effective area of the receiver antenna, $\sigma$ the surface or point target radar cross section (RCS), $R$ the satellite to target slant range. The term $kT_0B_PF_n$ accounts for the noise power at the output of the receiver, being $k$ the Boltzamann constant ($1.38 \cdot 10^{-23} J/K$), $T_0$ the ambient temperature (290 K), $B_P$ the processing bandwidth and $F_n$ the noise figure of the receiver chain. $L_T$ accounts for all the losses in the system and 2-way link (transmitter, receiver, atmospheric losses, etc).

Equation (7.1) can be rearranged by taking the expression of the effective area of an antenna ( $A_r = G_r \lambda^2 / 4\pi$ ) and considering the RCS of a distributed target as $\sigma = \sigma_0 \cdot \rho_{az} \cdot \rho_{gr}$ where $\sigma_0$ is the surface reflectivity of the terrain and $\rho_{az} \cdot \rho_{gr}$ the pixel size on ground determined by the azimuth and ground range resolutions. Then, the signal to noise ratio at the input of the receiver from a resolution cell is obtained as:

$$SNR_1 = \frac{P_t G_t G_r \sigma_0 \rho_{az} \rho_{gr} \lambda^2}{(4\pi)^3 R_t^2 R_r^2 L_T k T_0 B_P F_n} \tag{7.2}$$

The SNR obtained for a single pulse in a GeoSAR case would be really poor and it could be compensated by using huge transmitted power. However, only moderate power is available in satellite platforms. Thus, the range pulse compression and the integration of the several pulses to perform the synthetic aperture will improve that level considering low or medium transmitted powers.

The pulse compression SNR improvement is given by the ratio between the transmitted pulse duration ( $\tau_0$ ) and the length of the compressed pulse ( $\Delta\tau$ ). On the other hand, the number of pulses integrated during the synthetic aperture formation is obtained multiplying the pulse repetition frequency (PRF) by the integration time ( $T_i$ ). In principle, the integration time is not limited by the synthetic aperture length as in the LEO SAR case. The constant line of sight between the satellite, at nearly fixed position, and the targets enables the possibility to increase the integration time as much as the system requires for getting the required SNR. However, very long integration times are not desirable since the coherence loss of the terrain can degrade the final SNR. Besides, long integration times will decrease the frequency of captured images as well. Then, the improvement factor due to the SAR processing will be:

$$\Delta P = \frac{\tau_0}{\Delta\tau} \cdot PRF \cdot T_i \tag{7.3}$$

So, the SNR after SAR processing with the improvement factor computed in (7.3) is computed as:

$$SNR_0 = SNR_1 \cdot \Delta P = \frac{P_t G_t G_r \sigma_0 \rho_{az} \rho_{gr} \lambda^2}{(4\pi)^3 R_t^2 R_r^2 L_T k T_0 B_P F_n} \cdot \frac{\tau_0}{\Delta\tau} \cdot PRF \cdot T_i \tag{7.4}$$

In the design of a radar system, the bandwidth $B_P$ is chosen in order to be the inverse of $\Delta\tau$. Furthermore, the product of the pulse duration by the PRF is known as the duty cycle (DC). Then, the SNR will be:

$$SNR_0 = SNR_1 \cdot \Delta P = \frac{P_t G_t G_r \sigma_0 \rho_{az} \rho_{gr} \lambda^2}{(4\pi)^3 R_t^2 R_r^2 L_T k T_0 F_n} \cdot DC \cdot T_i \tag{7.5}$$

As it can be seen in equation (7.5), once the radar, antenna and geometry parameters are chosen, a trade-off between the desired resolution and the achieved SNR must be considered. If the SNR obtained is too low, the resolution can be degraded to win some extra dB. On the other hand, if the SNR is over the minimum levels, some dBs can be scarified in order to improve the image resolution. Anyway, the relation between SNR after SAR processing and the pixel area will be fixed by the system parameters:

$$\frac{SNR_0}{\rho_{az}\rho_{gr}} = \frac{P_t G_t G_r \sigma_0 \lambda^2}{(4\pi)^3 R_t^2 R_r^2 L_T k T_0 F_n} \cdot DC \cdot T_i \tag{7.6}$$

In the following sections, different GeoSAR configurations are analysed and the SNR levels expected are computed. First of all, the monostatic GeoSAR case re-using the telecommunication satellite emitted signal will be considered. After that, the monostatic and bistatic approaches for an ad-hoc geosynchronous mission power budget will be presented. All the budget results are given for a distributed target (Earth's surface) and only in the telecommunications satellite compatible monostatic configuration case the point targets with high expected RCS (as parabolic antennas whose analysis is given in section 2.2) since their feasibility on the other cases has not been analysed yet. The high directivities of such antennas and alignment to the broadcasting satellites make them interesting for the monostatic case.

## *7.2 Telecommunication compatible GeoSAR power budget*

As it was presented in section 2.3, it is possible to have a receiver on board of a telecommunications satellite tuned at the same frequency of one of the transmitters collecting the echoes of the satellite transmitted signal in a monostatic configuration. In this case, the telecommunications antenna is used for transmitting and receiving as in all monostatic configurations. In such configuration, the orbital, antenna and transmitted signal parameters are fixed by the telecommunication operator and can not be modified to improve the SNR or any other SAR feature. Therefore, to reach an acceptable level of SNR, only the parameters related to SAR acquisition (duty cycle, integration time and pixel area) can be adjusted.

Let's take, as an example, the HISPASAT-1D parameters to image the Western Europe (scene centred at Barcelona: 2.11ºE, 41.23ºN). The satellite where the receiver has to be mounted must be selected accordingly with the Earth's zone of interest since constant line of sight must be assured to perform the integration during several hours. For targets placed in Europe (longitudes from 10º West to 40º East), HISPASAT-1D is a good candidate since it is placed at a longitude of 30º West. Furthermore, HISPASAT-1D has one of the beams pointing and covering part of Europe which is the zone of interest in this example (Fig. 7.1). The Equivalent Isotropic Radiated Power (EIRP= $P_t G_t$ ) over Barcelona is 54dBW as shows Fig. 7.1.

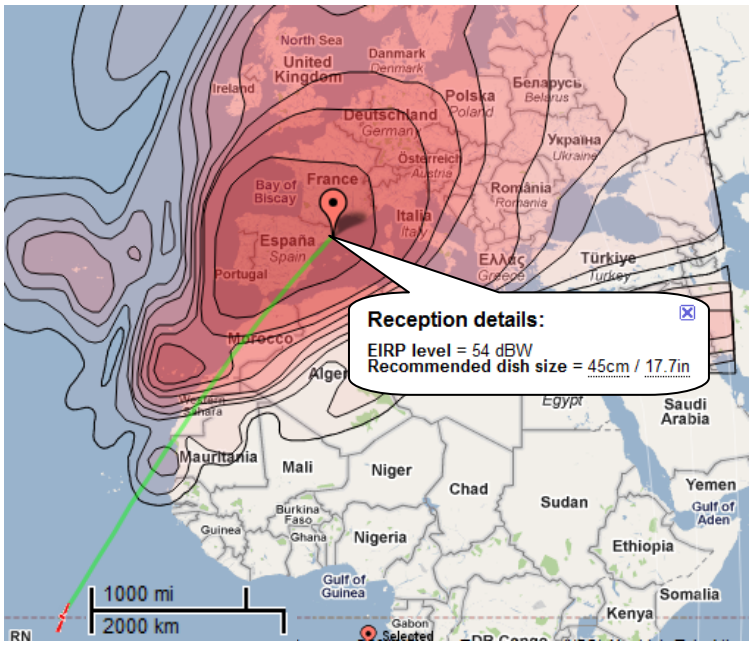


*Fig. 7.1 HISPASAT-1D footprint over Europe. EIRP level at Barcelona of 54dBW*

From the footprint coverage presented in Fig. 7.1, an estimation of the antenna parameters of the satellite can be calculated. Considering a main beam extension at -3dB of 1000 x 1000 Km approximately, an slant range to Barcelona of 38422Km, a frequency of 12GHz, the approximated size of the transmitter dish antenna can be obtained as:

$$\Delta R = 0.88\frac{\lambda}{\phi}R \rightarrow \phi = 0.88\frac{\lambda}{\Delta R}R \tag{7.7}$$

where $\Delta R$ is the ground coverage, $\lambda$ the working wavelength, $\phi$ the transmitter dish diameter and $R$ the slant range to the target. (7.7) would be only valid for a uniform illumination of the antenna which is not the case presented, where beamforming in transmission is used in order to get the desired footprint. However, (7.7) has been considered as a good approximation to start with and obtain the antenna gain necessary to compute the SNR. Using the parameters above, a diameter of 0.85 meters is obtained. From the diameter, the effective area of the antenna is easy to obtain as follows:

$$A_{eff} = A_{geo} \cdot \eta_{eff} = \pi \cdot \left(\frac{\phi}{2}\right)^2 \cdot \eta_{eff} \tag{7.8}$$

Where an efficiency of the antenna ( $\eta_{eff}$ ) of 0.85 has been considered. With these values, the effective area of the antenna is equal to 0.476 $m^2$. Finally, the antenna gain can be calculated from the effective area as:

$$G_t = A_{eff}\frac{4\pi}{\lambda^2} = 0.476\cdot\frac{4\pi}{\left(3\cdot10^8/12\cdot10^9\right)^2} = 39.8dB \tag{7.9}$$

The geometrical parameters of the satellite-target link and the SNR computation are summarized in Table 7.1 and Table 7.2, respectively. As it can be seen, illuminating a zone around Barcelona, a slant range of 38422 Km is obtained. On the other hand, the incidence angle of this point is about 58º which will be important in order to obtain the backscattering coefficient of the terrain, always given as a function of the incidence angle (in Table 7.2, a $\sigma_0$ of -10dB has been considered as an example for rough terrain at such incidence angles).

| **SYSTEM & GEOMETRY PARAMETERS** | | | |
|---|---|---|---|
| **Satellite** | | | |
| Orbit Period | $T$ | 24 | hours |
| Satellite latitude | $\varphi_{sat}$ | 0 | deg |
| Satellite longitude | $\lambda_{sat}$ | -30 | deg |
| SAT height over earth | $h_{sat}$ | 35786 | Km |
| Orbit radius | $r_{sat}$ | 42164.2 | Km |
| | | | |
| **Target** | | | |
| Local Earth's radius | $R_{earth}$ | 6368.8 | Km |
| Target Latitude | $\varphi_T$ | 41.23 | deg |
| Target Longitude | $\lambda_T$ | 2.11 | deg |
| | | | |
| **Satellite-Target Link** | | | |
| Sat-Target: Range | $R$ | 38422 | Km |
| Azimuth angle | $\theta_{az}$ | 223.6 | deg |
| Elevation angle | $\theta_{el}$ | 32.2 | deg |
| Look angle | $\theta_{look}$ | 7.3 | deg |
| Incidence angle | $\theta_{in}$ | 57.8 | deg |

*Table 7.1 Satellite target link geometric parameters*

From Table 7.2, an SNR of -123.6dB is obtained for one pulse considering the return of a single pixel (area of $\rho_{az}\times\rho_{gr}$ ). Similar results would be obtained with the parabolic antennas as a reflectors since RCS values around 20dBsm were obtained at this frequency (see section 2.2). This SNR is not enough to get a minimum image quality (at least 10dB of SNR should be reached). So, in this GeoSAR configuration, the improvement factor given by equation (7.3) is vital for the correct performance of the SAR system. So, the pulse compression improvement factor ( $\tau_0/\Delta\tau$ ) offers an SNR gain of 54.7dB considering a pulse duration of 0.05 sec and a bandwidth of 5.9MHz to reach the desired ground range resolution of 30 meters. The other factor that will improve the SNR after

processing is the number of integrated pulses. In this example, 12 hours of integration time at 10 Hz have been considered obtaining a SNR increase of 56.4dB.

| SNR COMPUTATION PARAMETERS | | | | | |
|---|---|---|---|---|---|
| **Parameter** | **Symbol** | **Value** | **SNR impact** | **SNR budget** | **Units** |
| Transmitted power | $P_t$ | 14 dBW | EIRP | +54 | dBW |
| Gain trans. | $G_t$ | 40 dB | | | |
| Gain rec. | $G_r$ | 40 dB | - | +40 | dB |
| Slant range | $R_t^2, R_r^2$ | 38421994.8 m | $\frac{\lambda^2}{(4\pi)^3 R^4}$ | -368.4 | $dBsm^{-1}$ |
| Wavelength | $\lambda$ | 0.0249827 m | | | |
| Pixel area | $\rho_{az}\rho_{gr}$ | 30m x 30m | RCS | +19.5 | dBsm |
| Backscattering | $\sigma_0$ | -10 dB | | | |
| System losses | $L_T$ | 3 dB | - | -3 | dB |
| $kT_0$ | - | $4 \cdot 10^{-21}$ J | Noise power | +134.3 | dB |
| Noise factor | $F_n$ | 2 dB | | | |
| Signal Bandwidth | $B$ | 5.9 MHz | | | |
| **SNR single pulse (per res. cell)** | | | $SNR_1$ | -123.6 | dB |
| Pulse duration | $\tau_i$ | 0,05 sec | Pulse compression $(\tau_i / \tau_0)$ | 54.7 | dB |
| Compress pulse duration | $\tau_0 = 1/B$ | 170 nsec | | | |
| PRF | - | 10 Hz | Integrated pulses $(PRF \cdot T_i)$ | 56.4 | dB |
| Integration time | $T_i$ | 43200 sec | | | |
| **SNR after SAR processing** | | | $SNR_0$ | -12.5 | dB |
| **Noise Equivalent Sigma Zero** | | | NESZ | 2.5 | dB |

*Table 7.2 SNR computation for the monostatic case re-using the signal of HISPASAT-1D*

However, even after the SAR processing, a final SNR of only -12.5dB can be achieved with this configuration which is still far away from the minimum desired SNR for image exploitation. Therefore, some of the input parameters of the acquisition have to be changed. It is necessary to keep in mind that the transmission parameters in this case are fixed, since the idea is to re-use the signal emitted by the telecommunication satellite and it can not be modified on our own way.

On the other hand, the integration time of 12 hours considered in this example is also a maximum value since it has to be taken into account that most of the surface is not still and the coherence of the scene after several hours may change producing a defocusing of our final image. Regarding the PRF, as it has been analysed in 5.3 and 5.4, higher values may be detrimental to the interferences and/or ambiguities. Furthermore, the duty cycle in a monostatic case is limited by the time division in transmission and reception. So, it neither can be increased arbitrary since in previous example it was already 50%.

Therefore, in this case, the only parameter that it can be adjusted to increase the final SNR is the pixel area of our image. This will only improve the SNR in case of considering distributed target not the parabolic antennas which will not be appropriate for acquisition with such satellites as HISPASAT-1D. As it has been previously commented, a one to one relation between geometric resolution and SNR is determined by (7.6). In the previous case, the ratio between SNR and resolution will be fixed by the following equation:

$$SNR_0(dB) - 10\log\left(\rho_{az}\rho_{gr}\right) = -42dB \tag{7.10}$$

Then, considering the relation given in (7.10), the minimum resolution cell necessary to get a SNR of 10dB can be obtained as:

$$\rho_{az}\rho_{gr} = 10^{(SNR_{0\min}+42dB)/10} = 158489m^2 \tag{7.11}$$

This gives an azimuth and ground range resolution around 400m considering a square pixel. As it can be seen, the resolution should be degraded too much in this kind of system in order to get high or medium resolution SAR images. However, this configuration is really attracting due to the low cost of mounting a SAR receiver in a telecommunication satellites. The solution to the SNR problems shown in the previous analysis could be in the next generation of high rate broadband satellites [16][17][18].

Recently, Eutelsat has launched KA-SAT which is the first multi-beam satellite to operate in ka-band. This satellite will provide broadband in Europe, the Mediterranean Basin and parts of the Middle East. The satellite is configured to work with 80 spotbeams. An scheme of the KA-SAT coverage is shown in Fig. 7.2. Each cell, covers an area of approximately 250 Km in diameter.

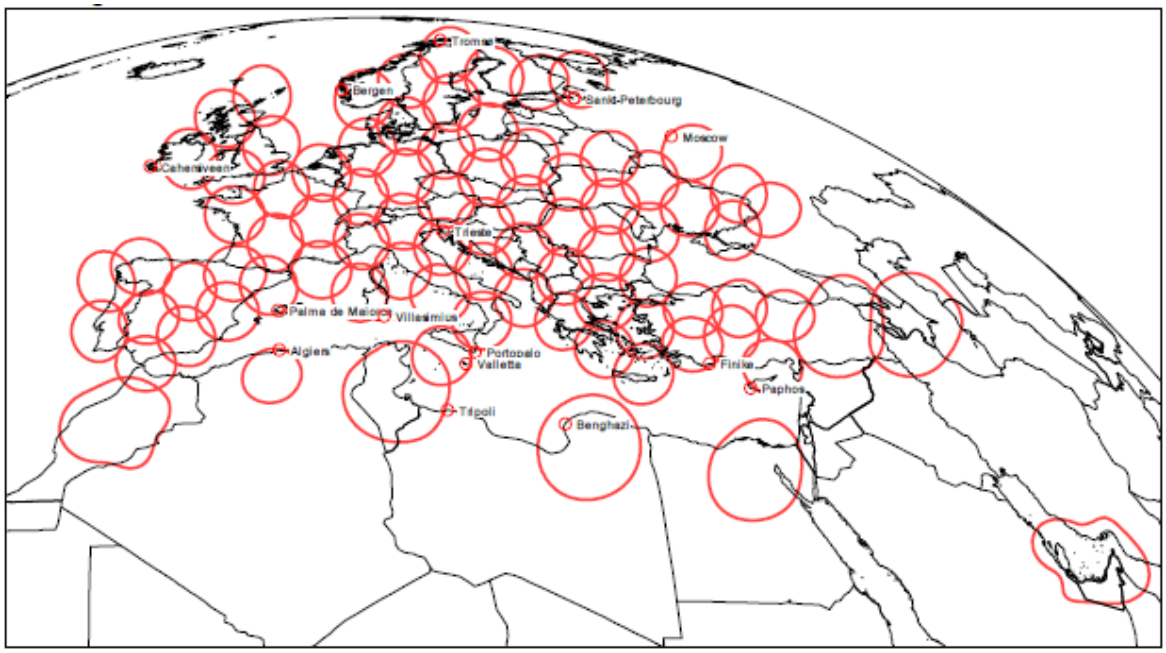


*Fig. 7.2 KA-SAT spotbeams over Europe. EIRP level at Barcelona around 70dBW*

From the cell diameter, the antenna size can be computed. In the case of KA-SAT, the specification for a cell diameter of 250Km gives a diameter of the effective aperture of 3.2 meters. Then, the effective area of the reflector will be in this case:

$$A_{eff_{KA-SAT}} = \pi \cdot \left( \frac{\phi_{eff}}{2} \right)^2 = 8.04 m^2 \tag{7.12}$$

which results in an antenna gain of:

$$G_t = A_{eff} \frac{4\pi}{\lambda^2} = 8.04 \cdot \frac{4\pi}{\left(3 \cdot 10^8 / 12 \cdot 10^9\right)^2} = 52.01 dB \tag{7.13}$$

The Travelling Waves Tubes (TWT) give a transmitted power of 140W for two beams. Considering 2dB of transmission losses, the transmitted power per beam will be around 16.45dBW. This gives an EIRP of 68.46dB. So, the values of Table 7.2 have been re-computed using the new parameters of KA-SAT.

| **SNR COMPUTATION PARAMETERS** | | | | | |
|---|---|---|---|---|---|
| **Parameter** | **Symbol** | **Value** | **SNR impact** | **SNR budget** | **Units** |
| Transmitted power | $P_t$ | 16.45 dBW | EIRP | +68.45 | dBW |
| Gain trans. | $G_t$ | 52.01 dB | | | |
| Gain rec. | $G_r$ | 52.01 dB | - | +52.01 | dB |
| Slant range | $R_t^2, R_r^2$ | 38421994.8 m | $\frac{\lambda^2}{(4\pi)^3 R^4}$ | -368.4 | $dBsm^{-1}$ |
| Wavelength | $\lambda$ | 0.0249827 m | | | |
| Pixel area | $\rho_{az}\rho_{gr}$ | 30m x 30m | RCS | +19.5 | dBsm |
| Backscattering | $\sigma_0$ | -10 dB | | | |
| System losses | $L_T$ | 3 dB | - | -3 | dB |
| $kT_0$ | - | $4 \cdot 10^{-21}$ J | Noise power | +134.3 | dB |
| Noise factor | $F_n$ | 2 dB | | | |
| Signal Bandwidth | $B$ | 5.9 MHz | | | |
| **SNR single pulse (per res. cell)** | | | $SNR_1$ | -97.14 | dB |
| Pulse duration | $\tau_i$ | 0,05 sec | Pulse compression ($\tau_i / \tau_0$) | 54.7 | dB |
| Compress pulse duration | $\tau_0 = 1/B$ | 170 nsec | | | |
| PRF | - | 10 Hz | Integrated pulses ($PRF \cdot T_i$) | 56.4 | dB |
| Integration time | $T_i$ | 43200 sec | | | |
| **SNR after SAR processing** | | | $SNR_0$ | 13.96 | dB |
| **Noise Equivalent Sigma Zero** | | | NESZ | -23.96 | dB |

*Table 7.3 SNR computation for the monostatic case re-using the signal of KA-SAT*

The new power link budget is presented in Table 7.3. In this case, the higher EIRP and antenna gain give a final SNR of almost 14dB which is considered good for acquisition. This configuration will be also valid for the parabolic antennas. However, the SNR value computed in Table 7.3 is obtained taking an integration time of 12 hours which, as it has been commented, may be too long depending on the scene temporal evolution and coherence. For this reason, the minimum integration time required to reach the threshold of 10dB of SNR can be obtained as:

$$T_{i\min} = 10^{(10\log Ti - 3.96dB)/10} = 4.8\,hours \tag{7.14}$$

So, a medium resolution image of 30 by 30 meters pixel area can be obtained re-using the signal of the KA-SAT satellite with an integration time of 5 hours. Therefore, the feasibility of such satellite to perform SAR acquisitions has been demonstrated in terms of the SNR for both, the distributed and point targets examples.

Similarly, a bistatic configuration could be considered. In this case, the telecommunications satellite could still be used as a transmitter but the reception chain would not be put in the same payload but in another satellite. Such bistatic configuration would make possible to tune the receiving system as the user desires giving an extra degree of freedom. So, the receiving antenna parameters, timing and scene coverage could be adjusted in the bistatic system while in the monostatic case these parameters were fixed by the telecommunications satellite configuration. Furthermore, using a bistatic configuration, the duty cycle of the system can be increased up to the 100% since it is not necessary to share the time between transmission and reception due to the separation of the transmitter and the receiver avoiding the transmission interferences.

So, taking the values of the KA-SAT SNR obtained in Table 7.3, but considering a pulse length of 0.1 seconds (the inverse of the PRF to reach the DC of 100%) and scene coverage of 130Km (an smaller spot inside one of the spotbeams of the KA-SAT). To reach such small spot in reception, the receiving antenna mounted on the platform should have a diameter of:

$$\Delta R = 0.88\frac{\lambda}{\phi}R \rightarrow \phi = 0.88\frac{0.025}{150Km}\cdot 38422Km = 5.64m \tag{7.15}$$

The gain in reception obtained with this antenna is computed as in (7.8) and (7.9), obtaining a value of 57dB. The new SNR values obtained with all the new parameters and considering the integration time computed in (7.14) are presented in Table 7.4. In this case, an SNR of 17.92 is obtained thanks to the higher gain in reception and the extra 3dB obtained using a DC of 100% instead of 50%. Regarding the slant range from the target to the receiving satellite, it can be considered similar to the transmission path. So, the same value has been taken in this example.

As in the previous cases, to improve the spatial resolution of the scene the SNR would be degraded. So, as it is computed in (7.16) a resolution of 12 by 12 meters can be achieved to assure the minimum acceptable SNR level of 10 dB. Therefore, with such bistatic configuration, a better resolution image of 12 by 12 meters pixel area can be obtained each 4.8 hours.

$$10\log\left(\rho_{az}\rho_{gr}\right) = 29.5dB - 7.92dB \rightarrow \rho_{az}\rho_{gr} = 10^{(29.5dB-7.92dB)/10} = 144m^2$$

$$\rho_{az} \times \rho_{gr} = 12 \times 12\, m \tag{7.16}$$

| SNR COMPUTATION PARAMETERS | | | | | |
|---|---|---|---|---|---|
| **Parameter** | **Symbol** | **Value** | **SNR impact** | **SNR budgtet** | **Units** |
| Transmitted power | $P_t$ | 16.45 dBW | EIRP | +68.45 | dBW |
| Gain trans. | $G_t$ | 52.01 dB | | | |
| Gain rec. | $G_r$ | 57.00 dB | - | +57.00 | dB |
| Slant range | $R_t^2, R_r^2$ | 38421994,8 m | $\frac{\lambda^2}{(4\pi)^3 R^4}$ | -368.4 | $dBsm^{-1}$ |
| Wavelength | $\lambda$ | 0,0249827 m | | | |
| Pixel area | $\rho_{az}\rho_{gr}$ | 30m x 30m | RCS | +19.5 | dBsm |
| Backscattering | $\sigma_0$ | -10 dB | | | |
| System losses | $L_T$ | 3 dB | - | -3 | dB |
| $kT_0$ | - | $4 \cdot 10^{-21}$ J | Noise power | +134.3 | dB |
| Noise factor | $F_n$ | 2 dB | | | |
| Signal Bandwidth | $B$ | 5.9 MHz | | | |
| **SNR single pulse (per res. cell)** | | | $SNR_1$ | -92.15 | dB |
| Pulse duration | $\tau_i$ | 0,1 sec | Pulse compression ($\tau_i / \tau_0$) | 57.7 | dB |
| Compress pulse duration | $\tau_0 = 1/B$ | 170 nsec | | | |
| PRF | - | 10 Hz | Integrated pulses ($PRF \cdot T_i$) | 52.37 | dB |
| Integration time | $T_i$ | 4.8 · 3600 sec | | | |
| **SNR after SAR processing** | | | $SNR_0$ | 17.92 | dB |
| **Noise Equivalent Sigma Zero** | | | NESZ | -27.92 | dB |

*Table 7.4 SNR computation for the bistatic case re-using the signal of KA-SAT with a scene coverage of 150Km*

As it has been seen in this section, the bistatic configuration re-using the signal of satellites like KA-SAT offers better results in terms of SNR making possible to obtain better resolution images than the monostatic case. On the other hand, the monostatic configuration would be easier and cheaper to implement. So, the better alternative must be chosen in each case depending on the final user interest and acquisition requirements.

After the power link budget analysis of a system conceived by re-using the transmitted signal of a telecommunications satellite, in the following section the SNR analysis for an ad-hoc geosynchronous SAR mission is considered. As it will be seen, such systems will offer more design flexibility but, as a drawback, the costs will rise with respect to the

telecommunications compatible GeoSAR example since all the design of the transmission and reception chain must be considered.

## *7.3 Ad-hoc GeoSAR mission power budget*

In this section, the power link budget for a SAR dedicated geosynchronous satellite will be presented. Obviously, the number of possibilities in this case is infinite depending on the user's requirements since the design is done from zero and takes into account the final needs of each acquisition. For this reason, in this section only one example taking standard power and timing values of a possible GeoSAR mission will be considered.

As an example, a monostatic GeoSAR system with a 15% of duty cycle will be considered. The transmitted peak power has to be chosen according the output power offered by the current technology of TWT. In this example, a transmitted power of 2400W will be considered (33.8 dBW). As it can be seen, this power level is much higher than the ones considered in the budgets on Table 7.2, Table 7.3 and Table 7.4, where the transmitted power was constrained by the satellite parameters since higher powers were not necessary for telecommunications broadcasting purposes.

The other main difference is the transmission and reception antenna gains. If the purpose of the acquisition is to image a concrete region, spot beam antennas with high directivities can be used. The telecommunications satellite antennas, usually broadcast antennas for high number of users in extensive areas, have low directivities which also penalize the final SNR obtained. In this example, an antenna gain of 55dB will be considered. Such antenna working at 12GHz will cover an area of an approximated diameter of:

$$G_t = A_{eff}\frac{4\pi}{\lambda^2} \rightarrow A_{eff} = 10^{55dB/10}\frac{0.025^2}{4\pi} = 15.72m^2 \tag{7.17}$$

$$A_{eff} = \pi\cdot\left(\frac{\phi_{eff}}{2}\right)^2 \rightarrow \phi_{eff} = 2\sqrt{\frac{A_{eff}}{\pi}} = 4.47m \tag{7.18}$$

$$\Delta R = 0.88\frac{\lambda}{\phi_{eff}}R = 0.88\frac{0.025m}{4.47m}\cdot 38422Km = 189Km \tag{7.19}$$

*A high resolution image of 10 by 10 meters is considered for this example. The noise and losses parameters are the same than in previous examples but changing the bandwidth to reach the 10 meters of ground range resolution. The most relevant SNR computation parameters are summarized in*
Table 7.5. In this case, the SNR will not be a problem due to the higher transmitted powers. Therefore, such systems offer more flexibility in the design, since the integration time and/or geometric resolution can be modified without problems on the final SNR.

This configuration can be the most suitable for another interesting application of the GeoSAR systems. Since the level of SNR is high enough, it is possible to get nearly continuous monitoring of the atmospheric proprieties. So, medium resolution images each 20 minutes could be periodically acquired in order to track the Atmospheric Phase Screen

| SNR COMPUTATION PARAMETERS | | | | | |
|---|---|---|---|---|---|
| **Parameter** | **Symbol** | **Value** | **SNR impact** | **SNR budget** | **Units** |
| Transmitted power | $P_t$ | 33.8 dBW | EIRP | +88.8 | dBW |
| Gain trans. | $G_t$ | 55.0 dB | | | |
| Gain rec. | $G_r$ | 55.0 dB | - | +55.00 | dB |
| Slant range | $R_t^2, R_r^2$ | 38421994.8 m | $\frac{\lambda^2}{(4\pi)^3 R^4}$ | -368.4 | $dBsm^{-1}$ |
| Wavelength | $\lambda$ | 0.0249827 m | | | |
| Pixel area | $\rho_{az}\rho_{gr}$ | 10m x 10m | RCS | +10.0 | dBsm |
| Backscattering | $\sigma_0$ | -10 dB | | | |
| System losses | $L_T$ | 3 dB | - | -3 | dB |
| $kT_0$ | - | $4 \cdot 10^{-21}$ J | Noise power | +129.5 | dB |
| Noise factor | $F_n$ | 2 dB | | | |
| Signal Bandwidth | $B$ | 17.7 MHz | | | |
| **SNR single pulse (per res. cell)** | | | $SNR_1$ | -88.1 | dB |
| Pulse duration | $\tau_i$ | 0,015 sec | Pulse compression ($\tau_i / \tau_0$) | 54.24 | dB |
| Compress pulse duration | $\tau_0 = 1/B$ | 56.5 nsec | | | |
| PRF | - | 10 Hz | Integrated pulses ($PRF \cdot T_i$) | 52.38 | dB |
| Integration time | $T_i$ | 4.8 · 3600 sec | | | |
| **SNR after SAR processing** | | | $SNR_0$ | 18.52 | dB |
| **Noise Equivalent Sigma Zero** | | | NESZ | -28.52 | dB |

*Table 7.5 SNR computation for a monosatic ad-hoc GeoSAR mission with an scene coverage of 190Km with a resolution cell of 10 by 10 meters.*

(APS) [19]—[22], an artefact that affects to GPS systems and other radar products which cause some aberrations in the phase of the received signal. Obtaining a continuous monitoring of the APS behaviour for a global zone of the Earth (which is possible with a geosynchronous satellite but not with a LEO), it could be compensated in the acquired data of other systems and avoid the problems derived from this random phenomenon. The SNR numbers referring the Atmospheric Phase Screening (APS) track are presented in Table 7.6. In this case, the antenna gain is lower (40dB) to cover a larger area (1062Km diameter). The integration time, as it was commented previously, has been set to 20 minutes. In this case, the resolution can be degraded (500 by 500 meters) since a high resolution image is not necessary to characterize the general behaviour of the APS. A final SNR of 10.90dB is obtained. So, the feasibility of this system to monitor the APS of a large scene of 1000Km diameter every 20 minutes with a resolution of 500 by 500 meters has been checked.

Finally, in the next section, the SNR analysis for a bistatic configuration with a receiver on ground will be considered.

| SNR COMPUTATION PARAMETERS | | | | | |
|---|---|---|---|---|---|
| **Parameter** | **Symbol** | **Value** | **SNR impact** | **SNR budget** | **Units** |
| Transmitted power | $P_t$ | 33.8 dBW | EIRP | +73.8 | dBW |
| Gain trans. | $G_t$ | 40.0 dB | | | |
| Gain rec. | $G_r$ | 40.0 dB | - | +40.00 | dB |
| Slant range | $R_t^2, R_r^2$ | 38421994.8 m | $\frac{\lambda^2}{(4\pi)^3 R^4}$ | -368.4 | $dBsm^{-1}$ |
| Wavelength | $\lambda$ | 0.0249827 m | | | |
| Pixel area | $\rho_{az}\rho_{gr}$ | 500m x 500m | RCS | +43.97 | dBsm |
| Backscattering | $\sigma_0$ | -10 dB | | | |
| System losses | $L_T$ | 3 dB | - | -3 | dB |
| $kT_0$ | - | $4 \cdot 10^{-21}$ J | Noise power | +146.54 | dB |
| Noise factor | $F_n$ | 2 dB | | | |
| Signal Bandwidth | $B$ | 0.35 MHz | | | |
| **SNR single pulse (per res. cell)** | | | $SNR_1$ | -67.09 | dB |
| Pulse duration | $\tau_i$ | 0,015 sec | Pulse compression $(\tau_i / \tau_0)$ | 37.20 | dB |
| Compress pulse duration | $\tau_0 = 1/B$ | 56.5 nsec | | | |
| PRF | - | 10 Hz | Integrated pulses $(PRF \cdot T_i)$ | 40.79 | dB |
| Integration time | $T_i$ | 20 · 60 sec | | | |
| **SNR after SAR processing** | | | $SNR_0$ | 10.90 | dB |
| **Noise Equivalent Sigma Zero** | | | NESZ | -20.90 | dB |

*Table 7.6 SNR computation for a monosatic ad-hoc GeoSAR mission for APS tracking.*

## *7.4 Bistatic configuration with ground receiver station power budget*

In this last power budget computation, a bistatic system with an on ground receiver will be considered. This system will also re-use the signal of a telecommunications satellite. The main difference will be that the location of the receiver on the earth's surface will avoid the return signal path of thousands of kilometres, giving higher SNR than the previous cases. This is an interesting example for academic purposes since it can be built with low-cost materials and mounted near a place of interest to get constant monitoring of a local zone. Interesting applications of those systems could be the determination of surface deformation, building subsidence in cities, local natural disaster monitoring (floods, earthquakes, landslides), etc.

In this example, the signal from the HISPASAT-1D will be used as a transmitted signal while the receiver will be mounted in a place near the Collserola Tower pointing to Barcelona which will be our target. In this case, the range from the transmitter to the target

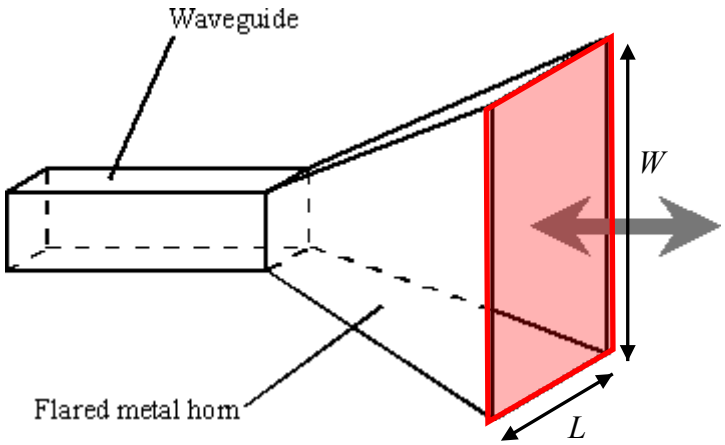


*Fig. 7.3 Horn antenna used as a receiver station on the bistatic on ground receiver configuration*

and the one from the target to the receiver will be different. A horn receiving antenna, as the one presented in Fig. 7.3 has been considered in this example. Such antennas are not as directive as the receiving antennas considered in the previous cases and the gain will be determined by the size of the antenna and the emitting red surface of Fig. 7.3. If a scene of 1Km x 1Km is considered, the size of the horn antenna can be approximately computed as:

$$\Delta R_1 = 0.88\frac{\lambda}{L}R_{T-rec} \rightarrow L = 0.88\frac{0.025}{1Km}\cdot 2.03\,Km = 4.48cm \tag{7.20}$$

$$\Delta R_2 = 0.88\frac{\lambda}{W}R_{T-rec} \rightarrow W = 0.88\frac{0.025}{1Km}\cdot 2.03\,Km = 4.48cm \tag{7.21}$$

$$S = L\cdot W = 20.03\,cm^2 \tag{7.22}$$

and from the antenna effective illuminated surface, the gain is obtained:

$$G = 4\pi\frac{S}{\lambda^2} = 16.05\,dB \tag{7.23}$$

So, considering the transmission parameters of HISPASAT-1D from Table 7.2 and the receiving antenna calculations presented above, the SNR results and the power link budget are given in Table 7.8. The geometrical transmission and reception link parameters are summarized in Table 7.7.

In this case, the short distance between the target and the receiver makes possible to get a high resolution image of 5 by 5 meters pixel size each 30 minutes with a final SNR of 22.68 dB. The duty cycle in this example has been set up to 100% (possible due to the bistatic configuration). As it can be seen, the SNR does not represent a problem using this

configuration and even shorter integration times could be used to get high-resolution images for scenes or phenomena with rapid temporal evolution.

| SYSTEM & GEOMETRY PARAMETERS | | | |
|---|---|---|---|
| **Transmitting Satellite** | | | |
| Orbit Period | $T$ | 24 | hours |
| Satellite latitude | $\varphi_{sat}$ | 0 | deg |
| Satellite longitude | $\lambda_{sat}$ | -30 | deg |
| SAT height over earth | $h_{sat}$ | 35786 | Km |
| Orbit radius | $r_{sat}$ | 42164.2 | Km |
| | | | |
| **Target** | | | |
| Local Earth's radius | $R_{earth}$ | 6368.8 | Km |
| Target height | $h_T$ | 111 | m |
| Target Latitude | $\varphi_T$ | 41.4 | deg |
| Target Longitude | $\lambda_T$ | 2.13 | deg |
| | | | |
| **Satellite-Target Link** | | | |
| Sat-Target: Range | $R$ | 38435 | Km |
| Azimuth angle | $\theta_{az}$ | 226.48 | deg |
| Elevation angle | $\theta_{el}$ | 32.09 | deg |
| Look angle | $\theta_{look}$ | 7.35 | deg |
| Incidence angle | $\theta_{in}$ | 57.91 | deg |
| | | | |
| **On ground receiver** | | | |
| Local Earth's radius | $R_{earth}$ | 6368.8 | Km |
| Height | $h_r$ | 460 | m |
| Target Latitude | $\varphi_T$ | 41.41 | deg |
| Target Longitude | $\lambda_T$ | 2.11 | deg |
| | | | |
| **Target-Receiver Link** | | | |
| Sat-Target: Range | $R$ | 2.03 | Km |
| Azimuth angle | $\theta_{az}$ | 213.7 | deg |
| Elevation angle | $\theta_{el}$ | 9.89 | deg |
| Look angle | $\theta_{look}$ | 88.04 | deg |
| Incidence angle | $\theta_{in}$ | 80.11 | deg |

*Table 7.7 Satellite target link geometric parameters*

| SNR COMPUTATION PARAMETERS | | | | | |
|---|---|---|---|---|---|
| **Parameter** | **Symbol** | **Value** | **SNR impact** | **SNR budget** | **Units** |
| Transmitted power | $P_t$ | 14 dBW | EIRP | +54 | dBW |
| Gain trans. | $G_t$ | 40 dB | | | |
| Gain rec. | $G_r$ | 16.05 dB | - | +16.05 | dB |
| Slant range transmission | $R_t$ | 38434,5 Km | $\frac{\lambda^2}{(4\pi)^3 R_t^2 R_r^2}$ | -282.88 | $dBsm^{-1}$ |
| Slant Range reception | $R_r$ | 2034.2 m | | | |
| Wavelength | $\lambda$ | 0.0249827 m | | | |
| Pixel area | $\rho_{az}\rho_{gr}$ | 5m x 5m | RCS | +3.98 | dBsm |
| Backscattering | $\sigma_0$ | -10 dB | | | |
| System losses | $L_T$ | 3 dB | - | -3 | dB |
| $kT_0$ | - | $4 \cdot 10^{-21}$ J | Noise power | +126.48 | dB |
| Noise factor | $F_n$ | 2 dB | | | |
| Signal Bandwidth | $B$ | 35.41 MHz | | | |
| **SNR single pulse (per res. cell)** | | | $SNR_1$ | -85.36 | dB |
| Pulse duration | $\tau_i$ | 0,1 sec | Pulse compression ($\tau_i / \tau_0$) | 65.49 | dB |
| Compress pulse duration | $\tau_0 = 1/B$ | 28.25 nsec | | | |
| PRF | - | 10 Hz | Integrated pulses ($PRF \cdot T_i$) | 42.55 | dB |
| Integration time | $T_i$ | 30 · 60 sec | | | |
| **SNR after SAR processing** | | | $SNR_0$ | 22.68 | dB |
| **Noise Equivalent Sigma Zero** | | | NESZ | -32.68 | dB |

*Table 7.8 SNR computation for the bistatic case re-using the signal of HISPASAT-1D with the on ground receiver*

# Chapter 8 GeoSAR Image Reconstruction

A very important part of any SAR system is the image reconstruction. The raw data collected from a scene must be correctly processed in order to give a helpful final product to the user. Several algorithms to process the raw data are used in SAR nowadays but not all of them will be appropriate for GeoSAR systems since the linear trajectory approximations that some of them consider. In this section, the basic SAR concepts on reconstruction will be shortly explained and the most suitable algorithm for the GeoSAR processing, the Time Domain Back-Projection (TDBP), will be presented. After that, the results obtained with this algorithm for different situations in a simulated GeoSAR system will be presented and the image characteristics analysed.

## 8.1 GeoSAR system model

First of all, the geometrical model used in a SAR system is presented to clarify the basic concepts on acquisition and processing. Consider an scene with several point targets with different reflectivities $\sigma_n$. Each point target is placed at an arbitrary position $(x_n, y_n)$ in the scene. The coordinate system is defined such as the *x* axis corresponds to the range or cross-track domain, while the *y* axis to the azimuth or along track domain. Let's assume a satellite with the antenna radar placed at (0, *u*) which illuminates the scene with a signal $p(t_r)$. In this case, the measured echo will be:

$$s_r(t_r, u) = \sum_n \sigma_n p\left[ t_r - \frac{2\sqrt{x_n^2 + (y_n - u)^2}}{c} \right] \tag{8.1}$$

The summation on (8.1) accounts for the different targets on the scene while

$$\frac{2\sqrt{x_n^2 + (y_n^2 - u)}}{c}$$

is the 2 way delay associated to each target on the scene considering the satellite position (0,*u*) at it transmission event. This example, presented in Fig. 8.1, is valid for a rectilinear satellite path but it is not the general situation for a GeoSAR system where several trajectories can be obtained playing with the geosynchronous satellite orbital ephemerides.

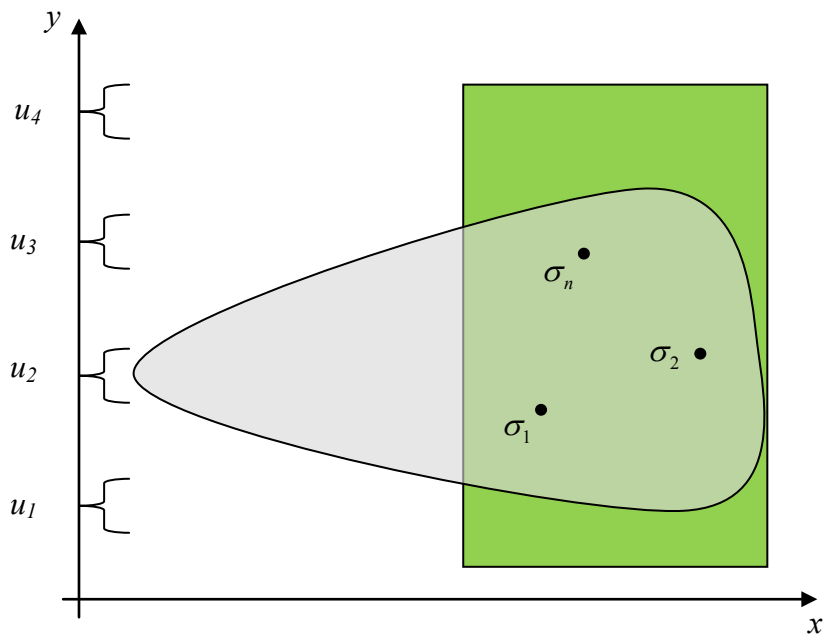


*Fig. 8.1 SAR system model for a linear satellite trajectory*

Then, considering an arbitrary trajectory as in Fig. 8.2, the satellite motion must be defined in a 3D coordinate system. The reference system considered in the GeoSAR

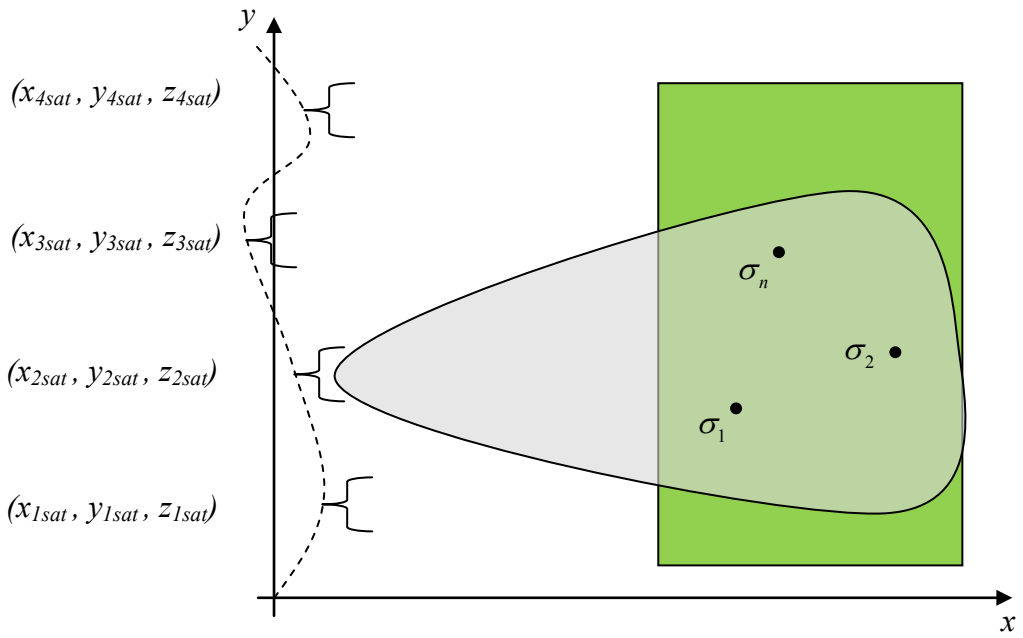


*Fig. 8.2 SAR system model for a non-linear satellite trajectory*

simulations is an Earth centred rotating coordinate system. In this way, the ($x_{sat}$, $y_{sat}$, $z_{sat}$) coordinates of the satellite can be obtained from the satellite longitude and latitude histories computed in (4.19) and (4.21) as:

$$x_{sat}(t_a) = r(t_a)\sin\left(90^o - \varphi_{sat}(t_a)\right)\cos\left(\lambda_{sat}(t_a)\right) \tag{8.2}$$

$$y_{sat}(t_a) = r(t_a)\sin\left(90^o - \varphi_{sat}(t_a)\right)\sin\left(\lambda_{sat}(t_a)\right) \tag{8.3}$$

$$z_{sat}(t_a) = r(t_a)\cos\left(90^o - \varphi_{sat}(t_a)\right) \tag{8.4}$$

where $r(t_a)$ is the temporal evolution of the orbital radius computed in (3.1) while $\varphi_{sat}(t_a)$ and $\lambda_{sat}(t_a)$ stands for the satellite latitude and longitude variations. A similar procedure has been used to determine the target locations in this new coordinate system. The position of the targets considering the Earth's centred rotating coordinated system is fixed if the target is not moving. So, from the target latitude, longitude and height over the earth reference ellipsoid, the target coordinates will be obtained as:

$$x_{tar_n} = \left(R_{earth}\left(\varphi_{tar_n}\right) + h_{tar_n}\right)\sin\left(90^o - \varphi_{tar_n}\right)\cos\left(\lambda_{tar_n}\right) \tag{8.5}$$

$$y_{tar_n} = \left(R_{earth}\left(\varphi_{tar_n}\right) + h_{tar_n}\right)\sin\left(90^o - \varphi_{tar_n}\right)\sin\left(\lambda_{tar_n}\right) \tag{8.6}$$

$$z_{tar_n} = \left(R_{earth}\left(\varphi_{tar_n}\right) + h_{tar_n}\right)\cos\left(90^o - \varphi_{tar_n}\right) \tag{8.7}$$

In this case, $R_{earth}\left(\varphi_{tar_n}\right)$ is the Earth's radius at the target's latitude. In this study, the WGS84 model [11] has been used to reproduce the Earth's geometry. $h_{tar_n}$ corresponds to the target height over the reference ellipsoid and the coordinates of the target are defined by $\varphi_{tar_n}$ and $\lambda_{tar_n}$ for the latitude and longitude respectively.

Then, considering the new geometry of the problem, the received signal in the radar can be modelled as follows:

$$s_r\left(t_r,t_a\right)=\sum_n \sigma_n p\left[t_r-\frac{2\sqrt{\left(x_{tar_n}-x_{sat}\left(t_a\right)\right)^2+\left(y_{tar_n}-y_{sat}\left(t_a\right)\right)^2+\left(z_{tar_n}-z_{sat}\left(t_a\right)\right)^2}}{c}\right] \quad (8.8)$$

Typically in SAR, the $t_r$ domain is known as *fast time or range domain* since it models the signal delay which will travel at the speed of light. On the other hand, the variable $t_a$ accounts for the satellite position at the different transmission events which has a slower evolution. Hence, it is known as the *slow time or azimuth domain.* Every PRI (Pulse Repetition Interval), the satellite transmits a pulse to the scene. For this reason, the slow time domain must be sampled each PRI second to model the transmission behaviour.

## *8.2 Digital reconstruction via Time Domain BackProjection (TDBP)*

The raw data obtained from a SAR system must be processed in order to obtain a focused image from the two dimensions matrix $\left(t_r,t_a\right)$ presented in the previous section. The Time Domain BackProjection (TDBP) algorithm is one of the most versatile SAR processing tools since does not consider any approximation and can be used for any system geometry and acquisition parameters. It makes this algorithm suitable for the GeoSAR case considered in this report.

The first step to reconstruct the image by TDBP is to perform a matched filtering in the fast time domain of the raw data. The fast time matched filter used in this case is a conjugated and reversed replica of the transmitted signal [23]. So, the fast-time matched-filtered SAR matrix will be obtained as:

$$s_M\left(t_r,t_a\right)=s_r\left(t_r,t_a\right)*p^*\left(-t_r\right) \quad (8.9)$$

In (8.9), a convolution in the fast time domain is performed for each received echo. So, considering the integration of several pulses all along the synthetic aperture formation, the pixel brightness for each target of the scene is computed as:

$$f\left(x_i,y_i\right)=\int_{x_{sat},y_{sat},z_{sat}} s_M\left(\frac{2\sqrt{\left(x_{tar_n}-x_{sat}\left(t_a\right)\right)^2+\left(y_{tar_n}-y_{sat}\left(t_a\right)\right)^2+\left(z_{tar_n}-z_{sat}\left(t_a\right)\right)^2}}{c},t_a\right)dt_a \quad (8.10)$$

where the fast time matched filtered response position corresponding to the 2 way delay from the satellite position at each slow time and the target position ($x_i$, $y_i$) is integrated for the whole synthetic aperture formation. The previous equation can be re-written as:

$$f(x_i, y_i) = \int_{x_{sat}, y_{sat}, z_{sat}} s_M\left(t_{ij}(t_a), t_a\right) dt_a \tag{8.11}$$

The backprojection SAR reconstruction algorithm add coherently the data of the fast-time bins that corresponds to the location of each scene point at each received pulse for all the synthetic aperture locations determined by the slow time. So, a reconstruction grid over the scene must be defined and the corresponding echoes from each point located in the fast time matched raw data matrix and added to retrieve the total power that comes from each scene position.

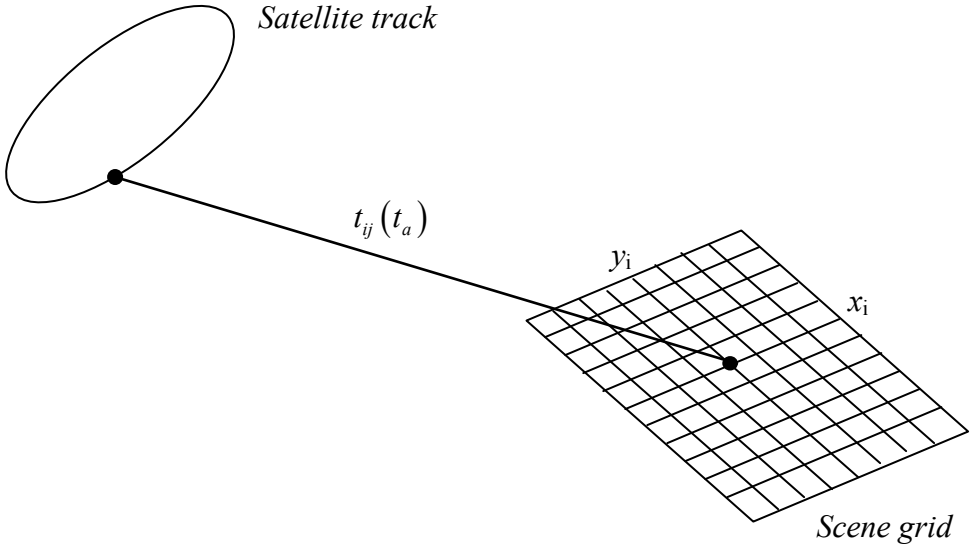


*Fig. 8.3 Backprojection algorithm geometric scheme*

The situation is presented schematically in Fig. 8.3. For each position of the scene grid, the two way delay must be computed for each satellite position at each slow time transmission event. Once the delay is computed for each slow time, the corresponding samples of the raw data matrix range compressed must be added coherently. If a bright target is placed in the position ($x_i$, $y_i$), the echoes from different slow times will give a strong power since all they will have high amplitude and the phases will be added constructively. On the other hand, if no target is placed in the computed grid position, the different samples of the raw data matrix will be added destructively giving a residual low power for that position of the scene grid.

This procedure must be repeated for each scene point to obtain the final reconstructed image. The scene grid must be sampled enough to properly focus the image (much more sampled than the ground range and azimuth resolution) to avoid wrong target positioning. It may be also necessary to interpolate the range compressed raw data matrix in the fast time domain in order to get the sufficient samples and more accurate results.

The complete algorithm is schematically summarized in Fig. 8.4. As it has been explained, the received data is range compressed and the sample corresponding to the delay from each transmitted pulse is integrated for all the position of the synthetic aperture.

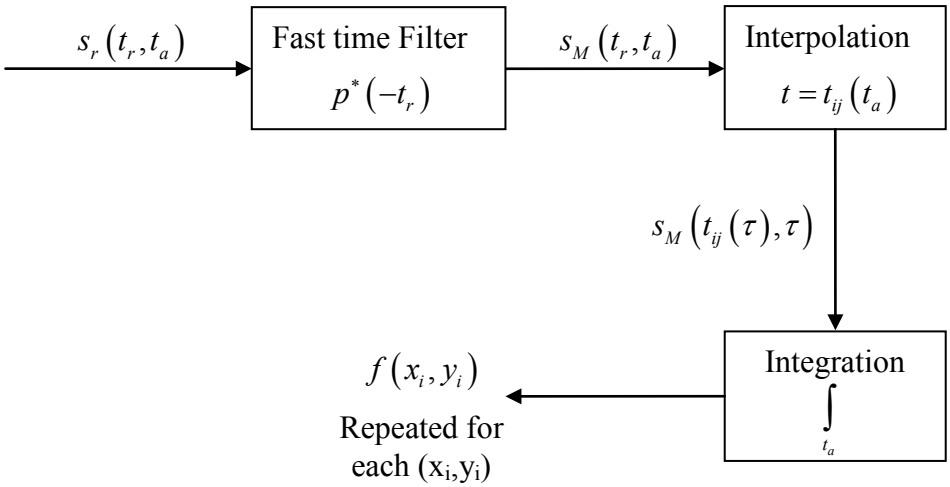


*Fig. 8.4 Backprojection algorithm performance scheme*

This algorithm, interesting for its versatility, has as a major drawback the computational cost. For large areas, the procedure must be repeated for all the points of the scene which can take long times. Several articles propose some strategies to decrease this time [24][25]. However, for our purpose to process GeoSAR images with long integration time and medium resolution it will not be a problem by now. In a future study, these algorithms should be analysed and applied to see their impact in the processing time.

## *8.3 Backprojection focusing for GeoSAR configurations*

In this section, several examples of backprojection focusing for different GeoSAR configurations are presented. The main performance of the algorithm used to process the GeoSAR raw data is similar to the one presented on the previous section with slight modifications to compensate the Doppler centroid of the acquisition (as explained in section 6.3). All the results on this section have been computed with the MATLAB GeoSAR simulator tool and the analysis is presented step by step from the orbit computation passing through the simulated raw data generation and the reconstruction of the final image.

First of all, a simple case will be analysed to determine the correct performance of the Time Domain Backprojection algorithm to focus the raw data generated by a GeoSAR system. Let's consider a scene placed over Barcelona (41.23ºN, 2.11ºE) of extension 1 by 1 Km with a single target in the central position. The scene is illuminated by a satellite placed at the same longitude with an orbit eccentricity of 0.0004 and no inclination of the orbital plane. Then, the first step performed by the simulator is the satellite orbital analysis and the satellite path computation. As a result, a 3D plot and the cuts from different views are given to the user to identify the satellite motion and the scene and target locations. In

Fig. 8.5, the results obtained with the parameters above are presented in the 3D plot. The red square is a zoom in for the satellite motion while in green the zoom in for the scene location is presented. As it can be seen, in the middle of the scene, a red dot shows the location of the target. The satellite track in Fig. 8.5 shows the satellite motion used in the synthetic aperture formation during the integration time, marked with a green line. In this example, an integration time of 12 hours has been considered.

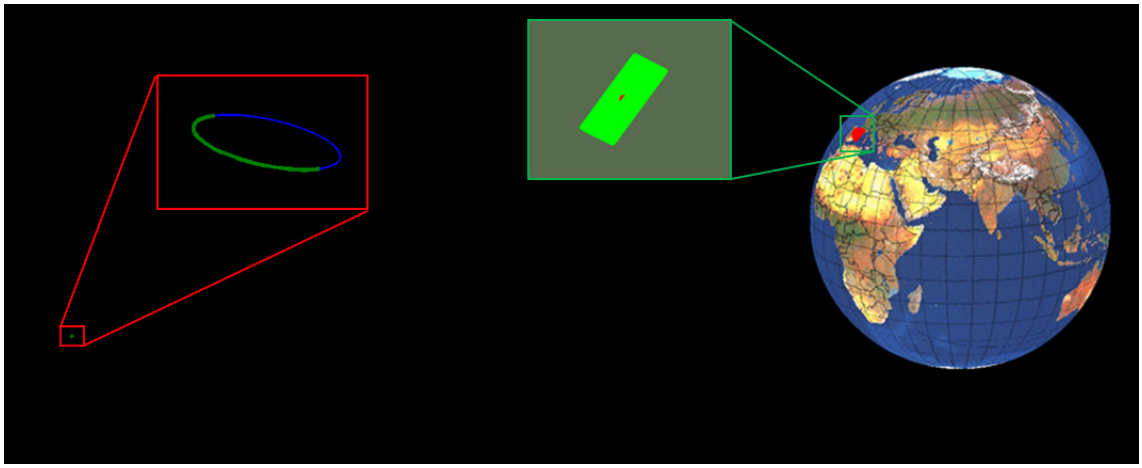

*Fig. 8.5 3D view of satellite path (eccentricity of 0.0004 and no inclination) and scene location (41.23ºN, 2.11ºE)*

Similarly, in Fig. 8.6, the different cuts of the satellite-scene geometry are shown. In Fig. 8.6 b), the non-constant radius of the orbit due to the eccentricity can be appreciated. On the other hand, in Fig. 8.6 c), the left-right motion or along track relative movement of the satellite with respect to the scene can be seen. It is the true motion that will affect to the azimuth resolution of the system and is the one that must be accounted in the synthetic aperture formation.

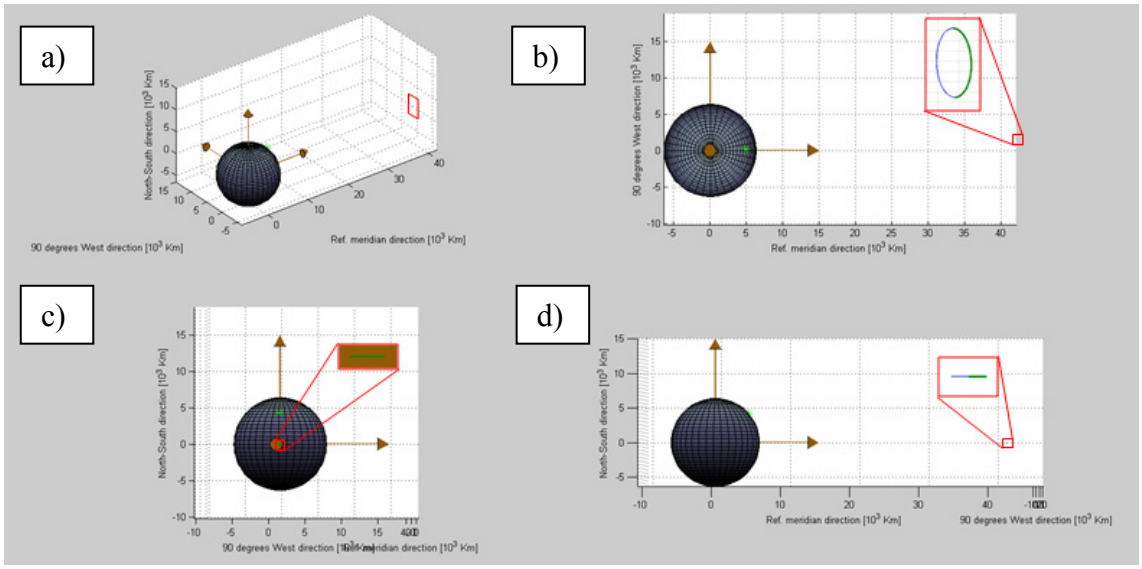


*Fig. 8.6 a) 3D orbital representation. b) Top view representation (reference meridian-90º West cut). c) Satellite nadir plane (North-90ºWest cut). d) Side view (North-Reference meridian cut).*

Once the satellite track and scene location have been defined, the program gives the opportunity to compute some SAR features such as the 2D or 3D diamond diagram presented in section 5.3, the Doppler history and Doppler centroid estimation as discussed in Chapter 6, determine the line of sight between the satellite and the scene (more important for a LEO orbit than in a GeoSAR system where a permanent line of sight is assumed), the ground track computation, etc. All these features and the results provided for the GeoSAR simulator tool are shown in each corresponding part of this report. In this section, only the relevant results to the SAR acquisition and image focusing will be presented and discussed.

So, the next step in GeoSAR acquisition simulation is the generation of synthetic raw data which will be processed with the backprojection algorithm. In order to simulate the raw data, a chirp has been chosen as a transmitted signal. An acquisition in Ku-band at 12 GHz with a frequency bandwidth of 3MHz has been considered. The chirp duration has been set up to 15 microseconds. A sampling frequency of 7.5MHz has been selected to fulfil the Nyquist criteria according to the signal bandwidth. The timing and bandwidth parameters of the transmitted signal have been chosen similar than in a typical LEO SAR acquisition to contrast both systems. In a real situation, the signal length should be increased to half the PRI in order to increase the transmitted pulse energy and, consequently, the received SNR. However, at the current status of the GeoSAR simulator it is not taken into account since the noise has not already been introduced in the simulations. These parameters have been chosen in order to avoid MATLAB out of memory problems which arise from the long integration times considered.

The transmitted signal and its Fourier transform are presented in Fig. 8.7 and Fig. 8.8, respectively. The chirp properties, 15 microseconds length and 3MHz bandwidth can be seen on those representations. Furthermore, the sampling frequency considered in this example is large enough since there is not aliasing in the Fourier transform presented in Fig. 8.8.

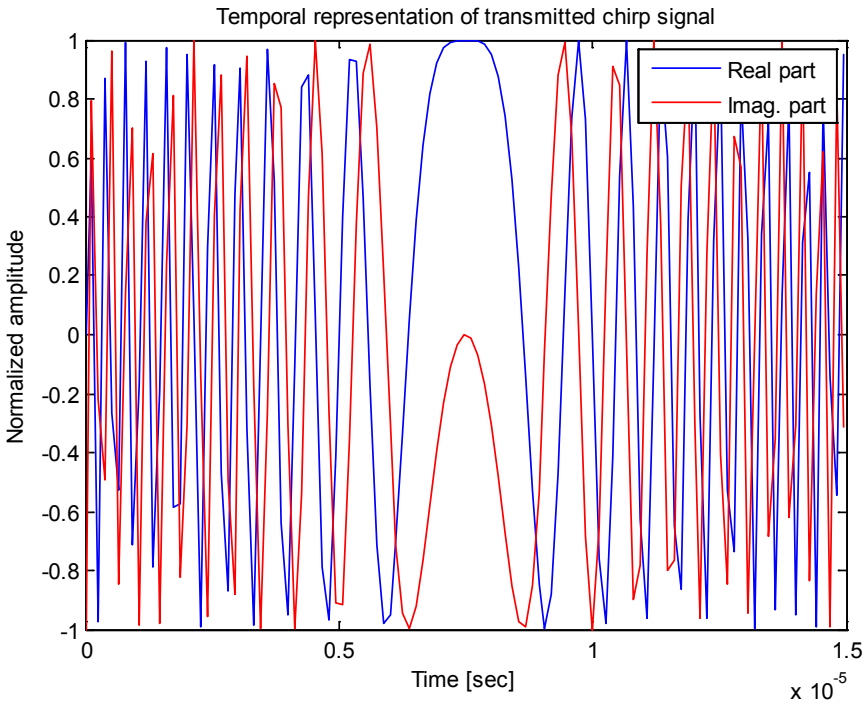


*Fig. 8.7 Temporal evolution of the transmitted chirp signal of 15 microseconds length*

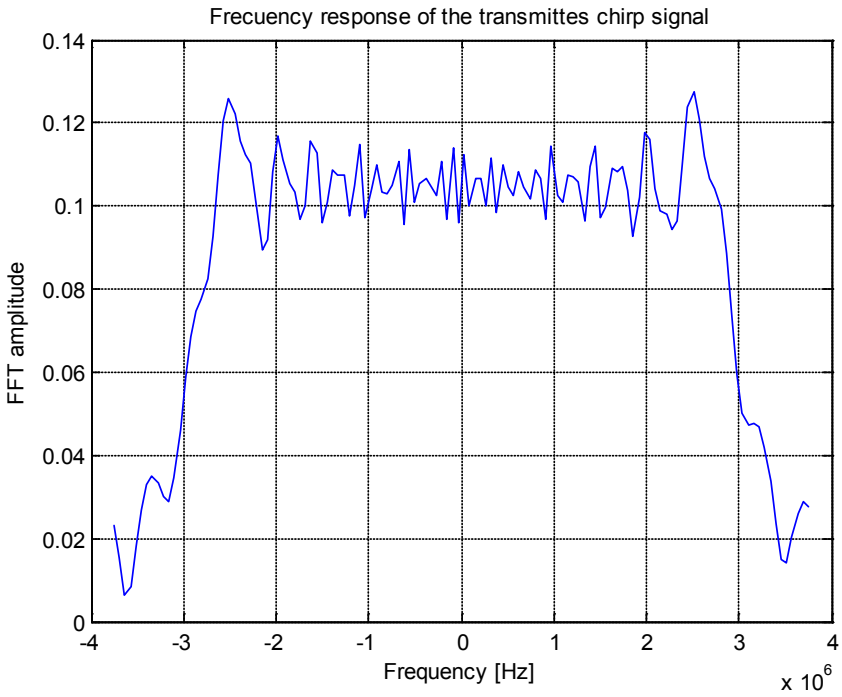


*Fig. 8.8 FFT of the transmitted chirp signal with frequency bandwidth of 3MHz*

Then, considering the transmitted chirp signal presented above and the 12 hours of acquisition time on Fig. 8.5, the raw data matrix obtained is presented in Fig. 8.9. The behaviour of the raw data matrix for a monostatic GeoSAR system is quite different to the one obtained from a point target in a typical LEO SAR given in Fig. 8.10. In the LEO acquisition, the quasi-constant range from the satellite to the scene makes that the final raw data matrix has a square shape since the fast time delay is nearly constant for all the pulses.

On the other hand, the fast time delay in a GeoSAR acquisition, where the orbital radius is not constant due to the orbit eccentricity, is constantly changing and produces the effect shown in Fig. 8.9. In this example, the satellite is firstly at a closer position and starts going further until the hour 12, when it is in the apogee of the orbit (furthest point of the satellite from the Earth) and the time delay is maxim. From this point, the satellite starts to approach until it would reach the perigee (the closest point to the Earth) which is not plot in Fig. 8.9.

In the case of a single point target, the normalized amplitude of the received raw data is equal to one when signal is received from the target since no influence of the antenna diagram is considered. Regarding the phase history, in the case of LEO SAR, a kind of hyperbolas can be appreciated in the phase plot of Fig. 8.10. However, for GeoSAR acquisition, the non constant radius introduces an extra phase component that changes the previous behaviour, making difficult to observe that on Fig. 8.9.

This is the kind of raw data matrices that our backprojection algorithm will have to deal with to reconstruct the GeoSAR image. But, as it has been previously explained in 6.3, a Doppler centroid track and compensation must be performed before the reconstruction.

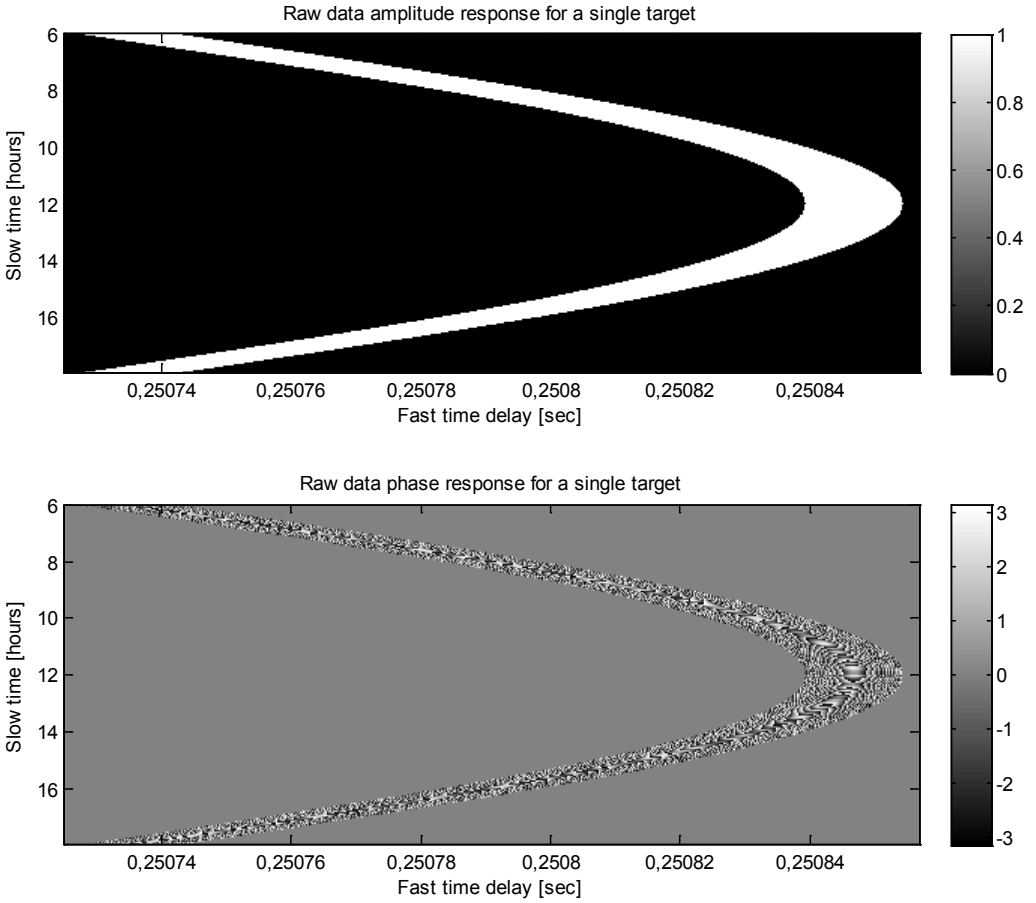


*Fig. 8.9 Simulated raw data from a point target in the central point of the scene*

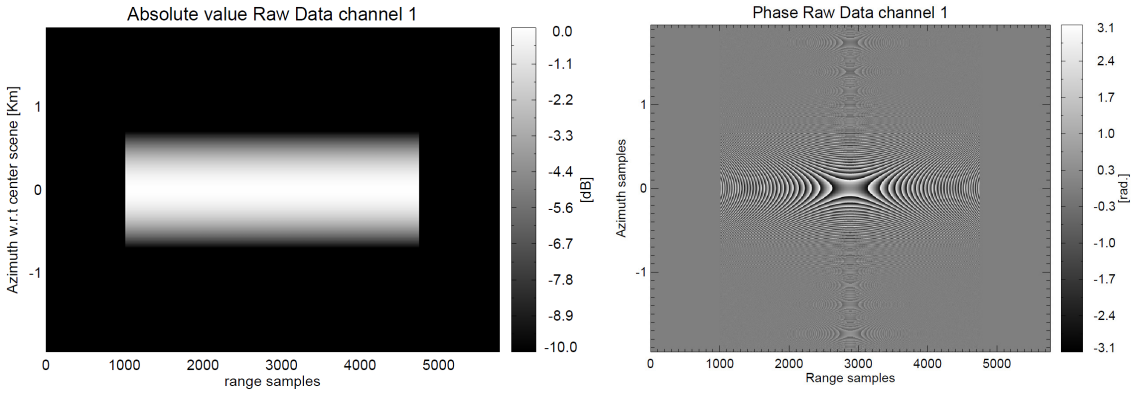


*Fig. 8.10 Typical raw data behaviour for a point target acquisition in LEO SAR*

The Doppler reference of the image can be set at any point even out of the scene. However, choosing the central point of the scene, the relative Doppler shifts of the other points will be smaller than in other cases, resulting in a lower Doppler bandwidth after compensation. Then, work with smaller Doppler bandwidth of the total scene makes possible to use lower PRF to correctly sample the scene. Therefore, the raw data matrix after compensation by the Doppler received from the central point is shown in Fig. 8.11.

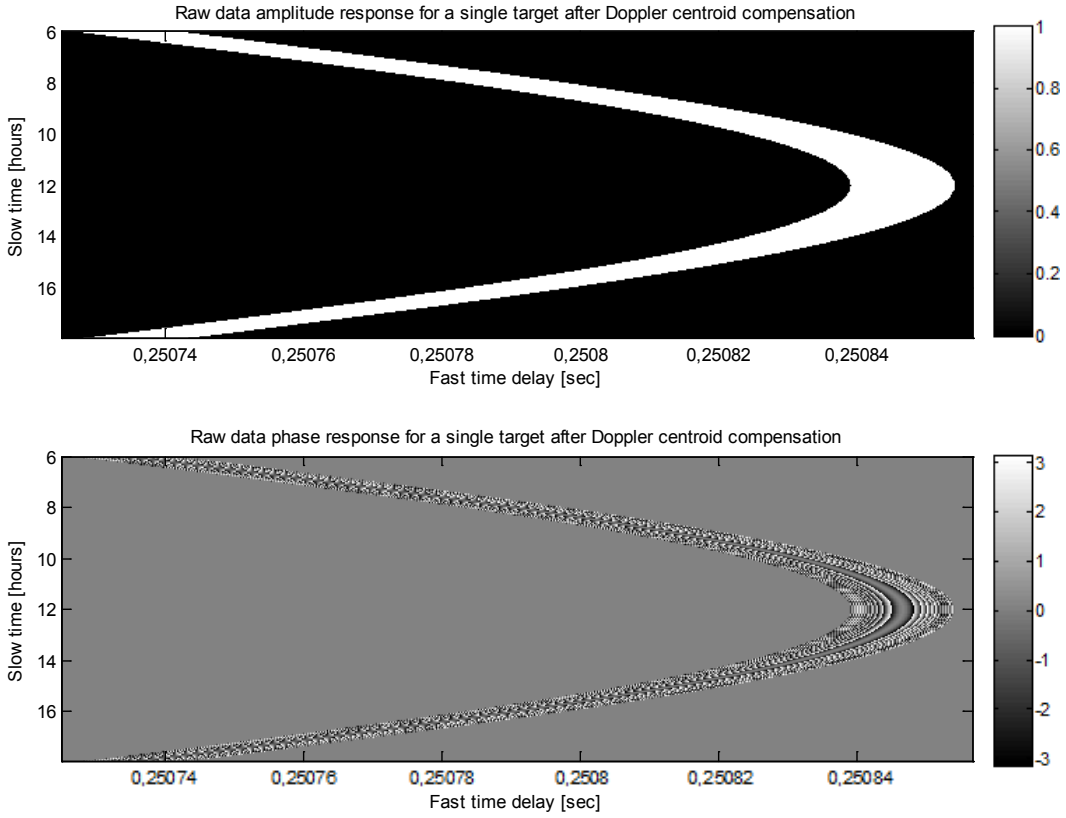


*Fig. 8.11 Simulated raw data from a point target in the central point of the scene after Doppler centroid compesation*

As it was expected, the amplitude of the raw data matrix after Doppler centroid compensation does not suffer any modification since only a phase shift have been introduced to compensate the Doppler centroid of the scene. On the other hand, the phase history of the raw data after compensation is quite different.

In the example presented, where the target and the Doppler reference are the same point, the phase of the raw data after compensation must be the same that the phase of the chirp. This is shown in Fig. 8.12, where the transmitted chirp phase and the received phase for a single row of the raw data matrix are compared. As it can be seen, the received pulse is a delayed replica of the original transmitted chirp.

Then, the focusing via Time Domain Backprojection can now be performed from the Doppler compensated raw data matrix.

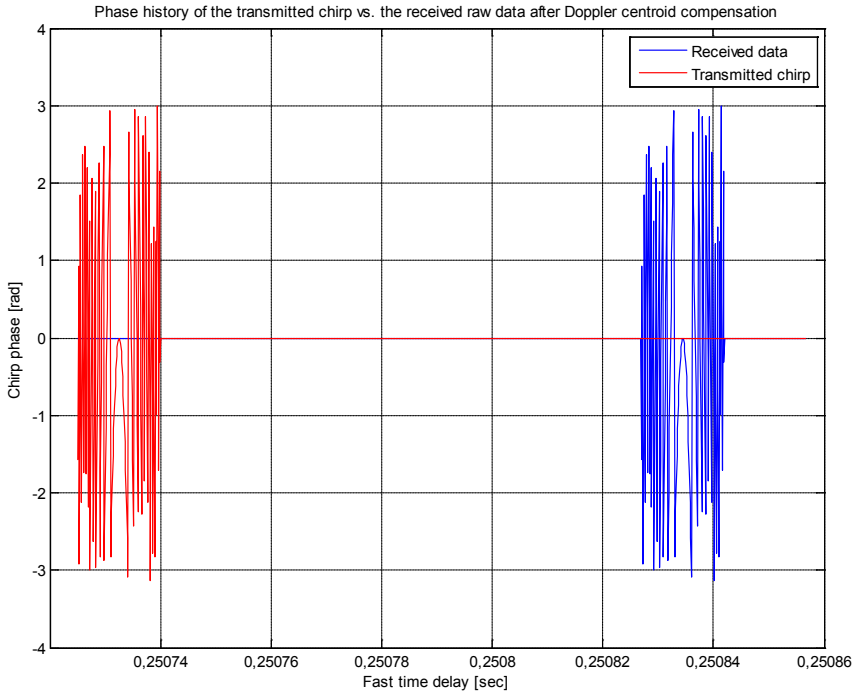


*Fig. 8.12 Transmitted chirp phase and received raw data phase after Doppler centroid compensation*

The backprojection algorithm used to focus the GeoSAR raw data is basically the one presented in section 8.2. First of all, the range match filtering must be performed. The convolution of the range matched-filter is implemented by computing the FFT of the raw data matrix in the fast time domain and the same for the range match filter. The computed FFTs are multiplied and the IFFT is applied to the obtained result. Only the samples of the resultant IFFT corresponding to the complete overlap between the filter and the raw data are considered.

In Fig. 8.13, the range compressed raw data matrix of the previous example is shown. A cut for a fixed slow time at 14 hours is presented. From this cut, an approximated duration of the compressed pulse (computed as the zero to zero main beam width) of 390 nanoseconds is obtained. The inverse of the compressed pulse duration (2.6MHz) should be around the input signal bandwidth (3MHz). So, the results of the range compressed raw data are quite precise.

So, now, the backprojection focusing can be applied over the range compressed raw data matrix. First, a scene grid where the TDBP will be computed has to be defined. In this example, a grid step of 5 meters for range and azimuth direction has been chosen to sample the 1 by 1 Km scene. Then, for each grid point, the 2 way slant range from the satellite corresponding to each transmitted pulse is computed. From each row of the raw data matrix the column corresponding to the slant range previously computed is added coherently and considering the phase shift associated to the delay with all the returns from

that scene point. An interpolation 1:10 in the fast time domain has been implemented to get more precise results.

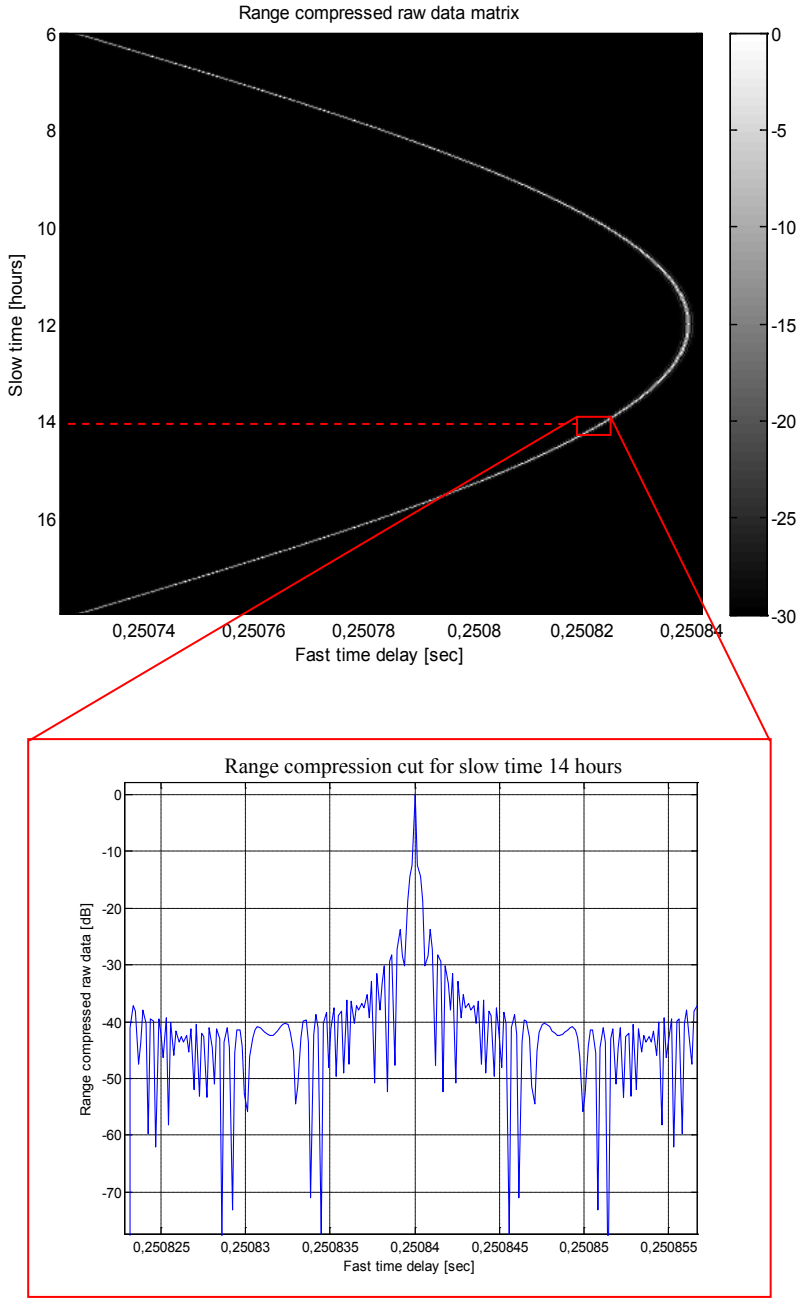


*Fig. 8.13 Range compression of the raw data matrix and cut for slow time of 14 hours.*

Once, the algorithm has been computed for all the points in the scene grid the focused image presented in Fig. 8.14 is obtained. As it can be seen, a bright point in the middle of the scene is found as it was expected.

The theoretical values for the azimuth and ground range resolutions computed with (5.24) and (5.36) are 6.85 meters and 60 meters, respectively. If these values are compared with the focused image, the ground range resolution looking at Fig. 8.14 is about 50 meters while the along-track resolution is around the 8 meters, close to the theoretical resolutions. In Fig. 8.15 a), the 3D point spread function is shown. Fig. 8.15 a) and b) show the azimuth and range cuts, respectively.

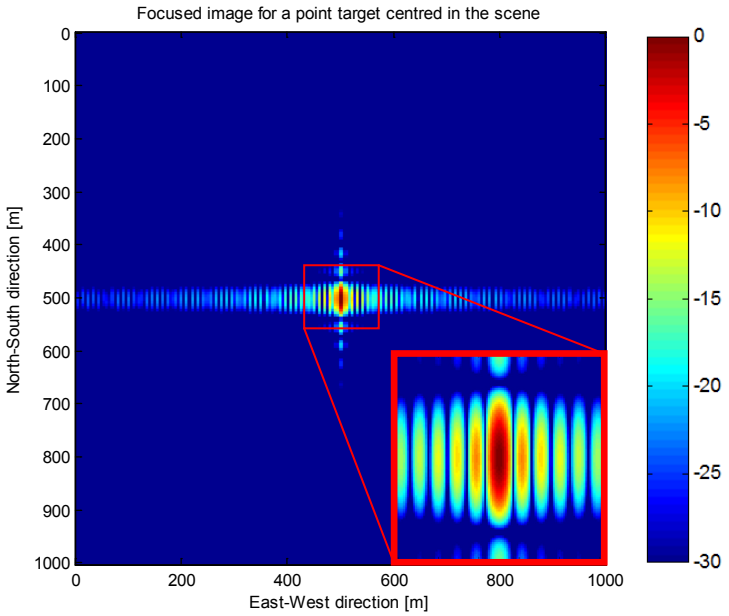


*Fig. 8.14 Focused image for the raw data from a single point target in the centre of the scene*

a)

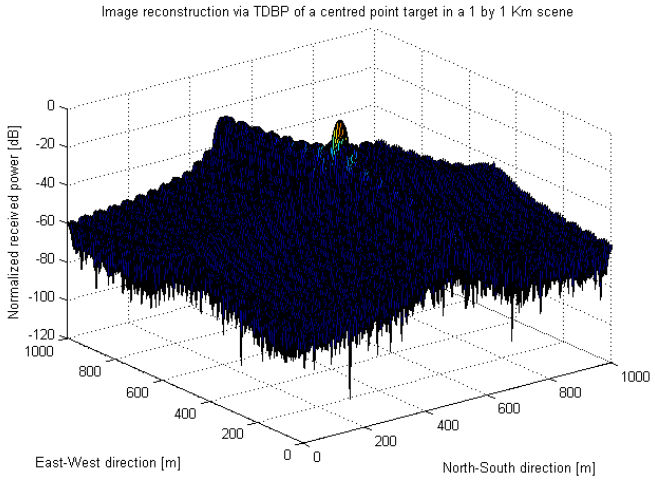


b)

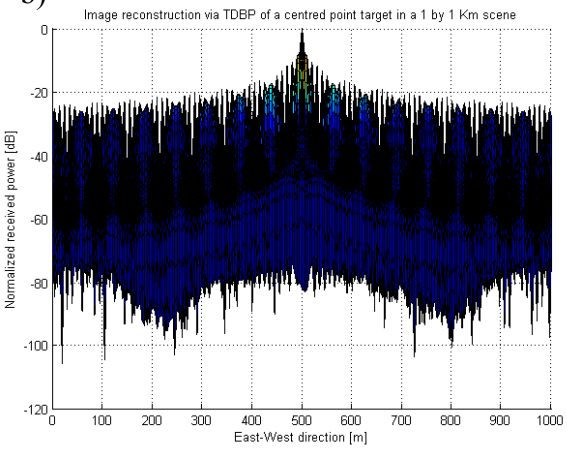


c)

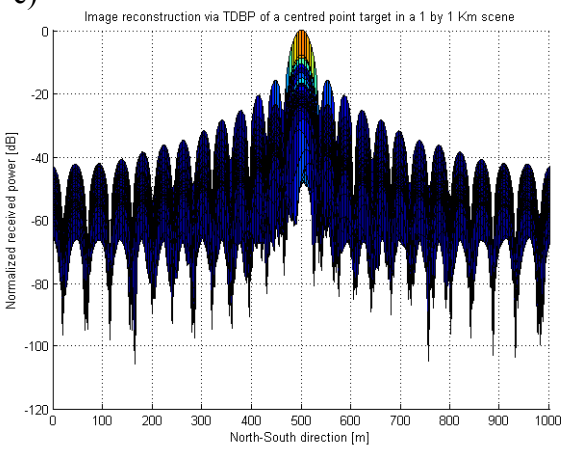


*Fig. 8.15 a) 3D representation of the point spread function, b) Target response azimuth cut and c) Target response range cut*

In SAR, a square pixel is typically used in the final reconstructed image. It means that the ground range and azimuth resolution are similar. To square the pixel, the azimuth resolution can be degraded by multi-look acquisition averaging several contiguous along track pixels. Similarly, the same can be done with the ground resolution if it is better than the azimuth one. On the other hand, more interesting with GeoSAR acquisition, the integration time can be reduced, shortening the length of the synthetic aperture and, consequently, degrading the azimuth resolution obtaining a larger pixel area. This larger pixel will mean, at the end, better SNR in reception which is desirable in those low received power echo systems.

So, as an example, let's consider a lower integration time of 2 hours instead of 12 hours. In this case, the theoretical azimuth resolution computed with (5.24) gives a value around the 50 meters, similar to the ground range resolution obtained in the previous example. The simulated results are presented in Fig. 8.16. As it can be seen, a square pixel of 50 by 50 meters resolution at -6dB is obtained.

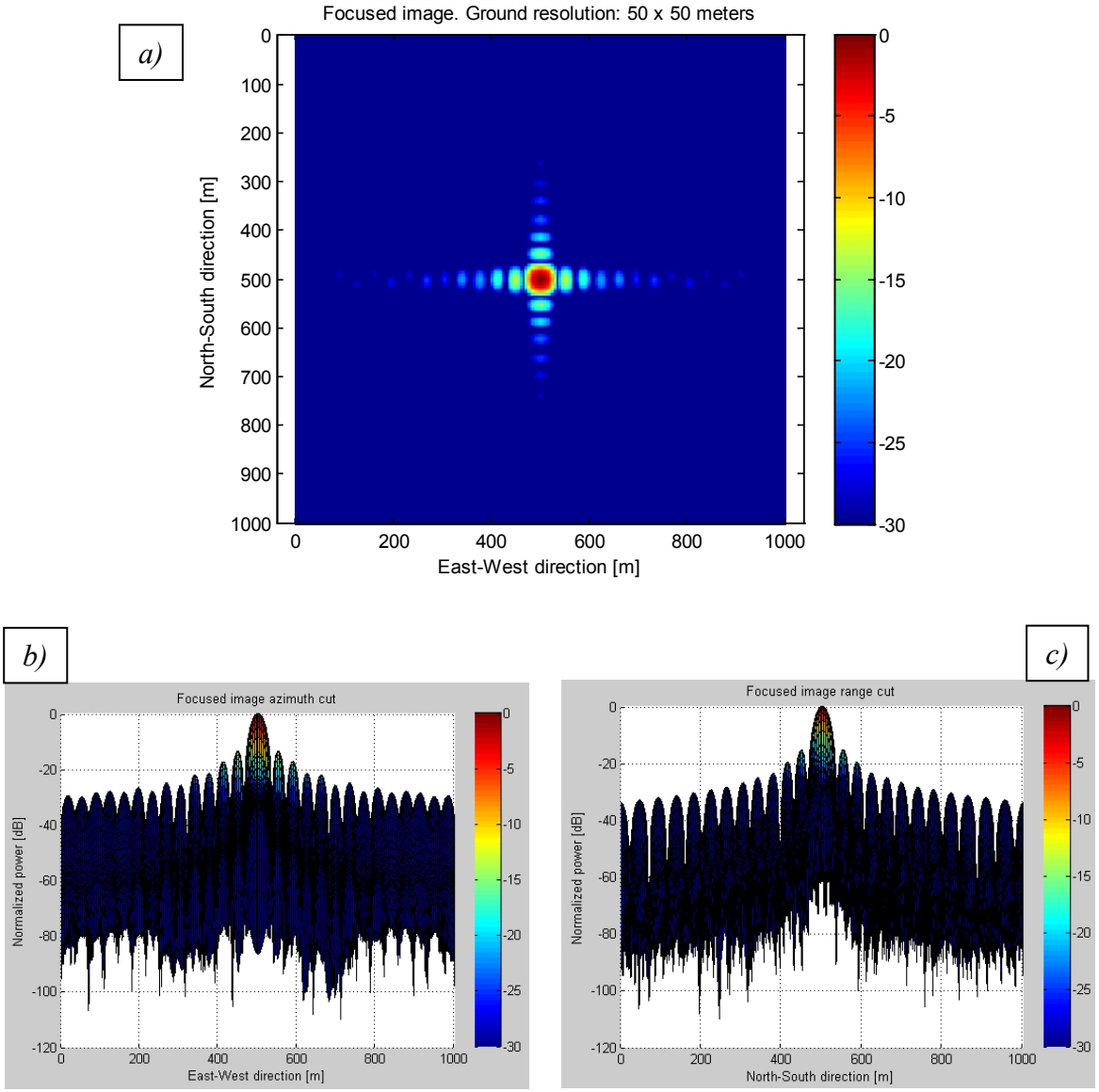


*Fig. 8.16 a) Focused image with squared pixel, b) Target response azimuth cut and c) Target response range cut*

Once the feasibility of the backprojection reconstruction for GeoSAR imagery has been checked, more complex scenes and/or systems can be simulated. In Fig. 8.17, an image from the previous example considering 10 point targets randomly placed at the scene has been properly reconstructed. The 10 point targets can be distinguished since their separation is larger than the SAR resolution of the considered configuration.

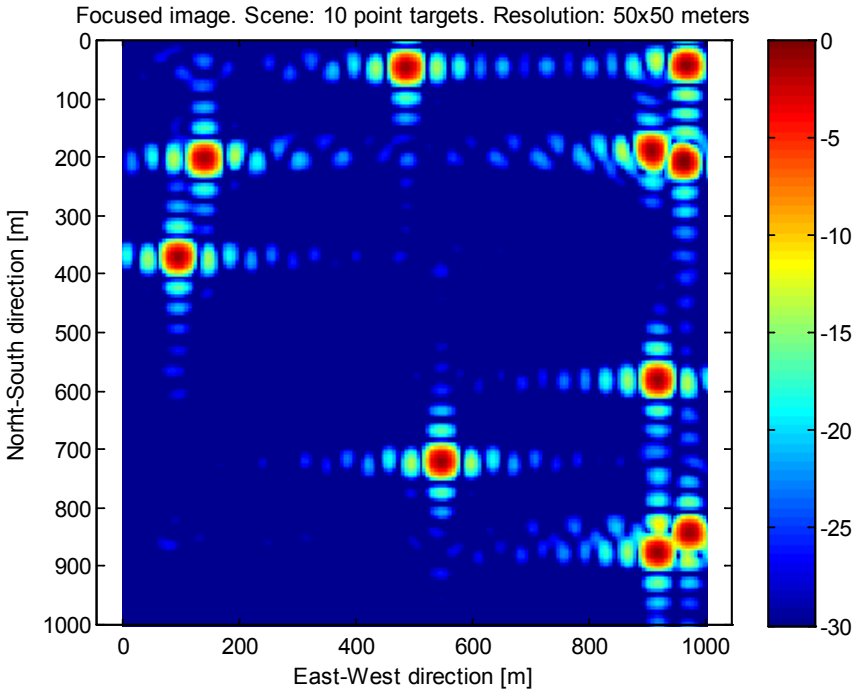


*Fig. 8.17 Focused 50 by 50 meters resolution image for 10 point targets scene*

Therefore, it has been stated that the reconstruction for a monostatic system from a geosynchronous configuration is possible via time domain backprojection algorithm. However, all along this document, bistatic configurations have also been presented. So, let's consider first a bistatic system made up with 2 geosynchronous satellites orbiting at different celestial cells but both in line of sight with the scene. The transmitter satellite will be placed at 3º West with 0.0004 eccentricity and no inclination of the orbital plane. On the other hand, the receiver is at 7º East with the same eccentricity but an inclination of 0.03º, in this example. The scene is still the one considered in the previous examples (1 by 1 Km centred at 41.23ºN, 2.11ºE) with 10 point targets placed randomly distributed.

After 2 hours of integration time, the raw data received from this pair of satellites is shown in Fig. 8.18. The final focused image is shown in Fig. 8.19. As it can be seen, the 10 targets can be observed and a pixel size of 45 x 45 meters is obtained, approximately.

So, the bistatic configuration with 2 geosynchronous satellites acquisition can be also focused with the backprojection algorithm. Finally, the bistatic approach but considering the receiver on ground will be analysed to determine the feasibility of the backprojection algorithm also in the reconstruction of this configuration.

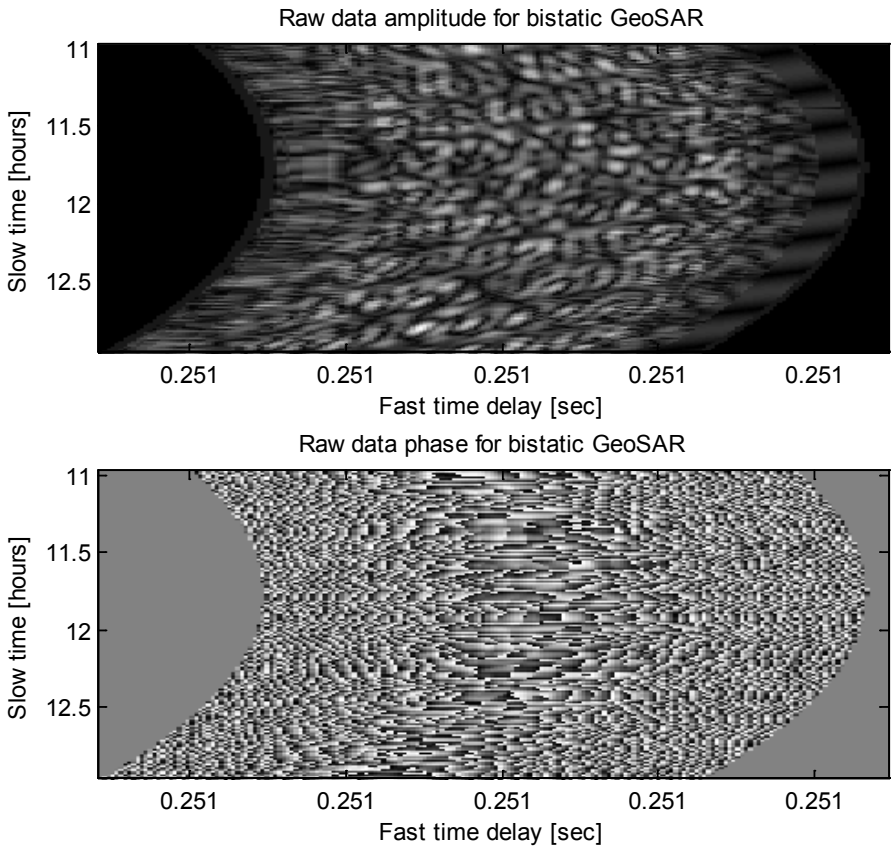


*Fig. 8.18 Raw data acquired with a bistatic GeoSAR configuration during 2 hours of integration time for 10 point targets.*

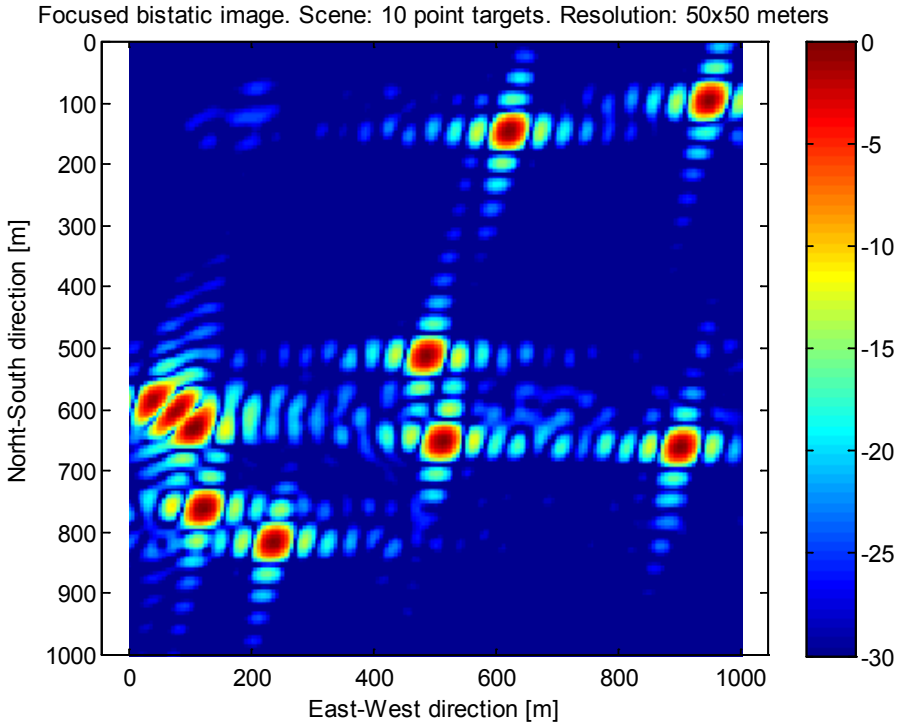


*Fig. 8.19 Focused image acquired with a bistatic GeoSAR configuration during 2 hours of integration time for 10 point targets*

In this last example, a transmitter placed at a geosynchronous satellite at 3ºW with eccentricity of 0.0004 and no inclination, as in the previous example, is considered. However, the receiver is placed at a fixed position on ground. This configuration with an on ground receiver has some advantages such as the higher level of SNR as it has been shown in section 7.4. In this example, the receiver has been placed at the Tower of Collserola, an strategic position to image the city of Barcelona. This tower is at 41.41ºN, 2.11ºE with a height of 460 meters. On the other hand, a zone of Barcelona with coordinates 41.13ºN, 2.12ºE and height of 111 meters has been considered.

The focused image obtained with this configuration is shown in Fig. 8.20. In this example, the signal bandwidth has to be increased from 3MHz to 10MHz in order to reach a similar ground range resolution than in the previous case. The ground range resolution was degraded due to the high incidence angles at which the target-receiver link is working. Regarding the integration time, 4 hours has been considered in this acquisition. The final image shows a nearly square pixel with a resolution around the 50 meters. So, the feasibility of the bistatic configuration with receiver on ground has been proved. However, the user has to be careful choosing the acquisition parameters to fulfil the final image requirement and also the orientation satellite-scene-receiver is also crucial for a correct image focusing.

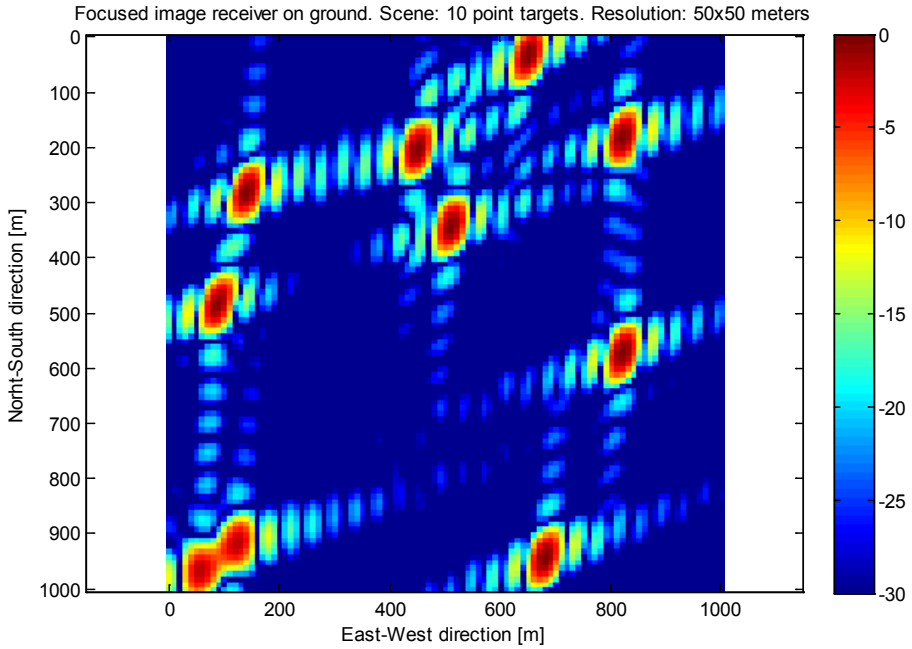


*Fig. 8.20 Focused image acquired with a bistatic GeoSAR configuration with receiver on ground.*

Consequently, the feasibility of the back-projection algorithm with Doppler centroid track and compensation has been checked for the different situations presented all along this report for the GeoSAR configuration. Despite the long computational times, the TDBP provides good results for the reconstruction of GeoSAR raw data. On the other hand, in future analysis, other algorithms such $\omega - k$ *[26]* will be considered to process and focus

GeoSAR images. The versatility of this other algorithm is expected to be appropriate for these systems as well. Furthermore, the computational cost is expected to be lower.

# CONCLUSIONS AND FUTURE WORK

A new GeoSAR configuration to obtain SAR images from geosynchronous satellites has been proposed and analysed in this project. The feasibility of such systems to perform SAR acquisition has been checked by a detailed analysis of the orbits of the geosynchronous satellites, not perfectly geostationary but with small perturbation in the eccentricity and/or inclination of the orbital plane. Such deviations are enough to generate the necessary relative motion between the satellite and the target in SAR acquisition. The features of the resultant synthetic aperture achieved depending on the mission parameters have been deeply studied obtaining satisfactory results to get SAR images from the geosynchronous satellites.

The special qualities of the acquisition from a geosynchronous orbital position give to the GeoSAR an important relevance in SAR context. So, it will be possible to have images from a particular zone of the Earth two or three times per day, more frequent than the typical revisit times of LEO missions of several days. This nearly continuous monitoring makes the GeoSAR acquisition really interesting for those applications that require constant information due to the fast evolution of the scene. As it has been commented in the report, natural disaster monitoring, Atmospheric Phase Screen tracking, terrain subsidence in unstable urban areas or continuous monitoring of active volcanic areas to predict future eruptions could be some of the applications of the GeoSAR missions.

However, some of the SAR features had to be checked previous the mission design to determine the feasibility of the system from a SAR radiometric point of view. So, the signal frequency properties of the received echo, the achievable geometric resolution, the SNR level after SAR processing, PRF selection or ambiguity analysis have been presented all along the document. The final results show the possibility to get a SAR image with acceptable levels of SNR by integrating the received pulses during several hours. Fortunately, it will not be a problem thanks to the nearly fixed position of the satellite which assures constant line of sight between the satellite and the scene.

Finally, the focusing of the simulated raw data from a geosynchronous satellite has been carried out via Time Domain Back-Projection algorithm. This processing technique does not require any linear approximation in the orbit given the highly non-linear satellite paths described by the geosynchronous satellites. The feasibility of the focusing considering three different situations (monostatic, bistatic and bistatic using on ground receiver configurations) has been demonstrated obtaining a perfect reconstruction of an non-noisy scene formed by several point targets. The final resolutions obtained were consistent with the theoretical results previously computed.

To sum up, the viability of geosynchronous satellite to get SAR images has been assessed. The analysis shows the possibility to get high or medium resolution images with medium SNR levels with 4-5 hours of integration time. However, the work is still not finished and several steps must be done to complete the analysis of the GeoSAR acquisition.

First of all, the so called $\omega$-$k$ reconstruction algorithm [26] should be considered on the focusing and the results obtained compared with the backprojection results. Although similar images are expected since the same raw data should be considered, the computation time may be reduced with this algorithm.

On the other hand, space segment design of the mission should be studied. The power requirements of the platform, downlink, hardware to mount in the satellite (block diagram) as well as orbital maintenance (combustible) should be considered in a satellite payload design.

Another point presented in this section and no further studied is the analysis of the TV parabolic antennas as reflectors of opportunity. In this report only a theoretical approach has been provided, but experimental observations and results could be carried out in order to corroborate these results. The theoretical study of the Atmospheric Phase Screening and the possibility to track its history with low resolution images each 10 or 20 minutes has to be carefully analysed as well. The GeoSAR possibilities on this field could offer an interesting method to compensate the APS from the GPS received signal, an artefact that nowadays is still producing errors on the GPS signal reception.

Furthermore, an experimental system based on the on ground receiver configuration could be considered. A hard investigation in this bistatic configuration considering the mission design, receiver payload, etc would be necessary to obtain the first results. The applications of those systems on local imaging for determined zones could make this configuration an interesting and cheap SAR tool. However, it will be necessary to find a way of tracking the satellite orbital position precisely in order to apply the backprojection algorithm correctly in reception.

Therefore, only a part of the GeoSAR mission analysis has been done until now. Several topics have to be checked and analysed yet. However, the novelty of this satellite configuration to get SAR images with unique characteristics makes the GeoSAR an interesting field of investigation for the next years on my Ph.D research.

# REFERENCES


[1] Elachi, C. '*Spaceborne SAR Remote Sensing: Applications and Techniques'* , Chapters 3-5.

[2] Curlander, J.C. and McDonough, R.N., *'Synthetic Aperture Radar: Systems and Signal Processing'*, Chapter 1: *Introduction to SAR*, New York, 1991.

[3] Skolnik, M. I. *'Radar Handbook'*, Chapter 21: *Synthetic Aperture Radar*, L.J. Cutrona, Sarcutron Inc.

[4] Tomiyasu, K. and Pacelli, J.L. *'Synthetic Aperture Radar Imaging from an Inclined Geosynchronous Orbit'*, IEEE Transactions on Geoscience and Remote Sensing vol. GE-21, No. 3, July 1983.

[5] Prati, C., Rocca, F., Giancola, D. and Monti, A. *'Passive Geosynchronous SAR System Reusing Backscattered Digital Audio Broadcasting Signals'*. IEEE Transactions on Geoscience and Remote Sensing, Vol. 36, No. 6, November 1998.

[6] Cazzani, L. *et al*, *'A Ground-Based Parasitic SAR Experiment'*, IEEE Transactions on Geoscience and Remote Sensing, Vol. 38, No. 5, September 2000.

[7] M. Bonomelli and F. Potra, *'Studio di un sistema SAR geostazionario passivo'*, Tesi Laurea Ing. Elett., Politec. Milano, Milano, Italy, 1994.

[8] D. Giancola and G. Quario, *'Studio di fattibilità di un sistema SAR geostazionario'*, Tesi Laurea Ing. Elett., Politec. Milano, Milano, Italy, 1995.

[9] S.N. Madsen et al, '*A Geosynchronous Synthetic Aperture Radar for Tectonic Mapping, Disaster Management and Measurements of Vegetation and Soil Moisture'*, Jet Propulsion Laboratory, Geoscience and Remote Sensing Symposium, 2001. IGARSS '01. IEEE 2001 International

[10] G. Maral and M. Bousquet, *'Satellite Communications Systems. Systems, Techniques and Technology'*, Wiley, Fourth Edition 2002.

[11] Technical report, *'WGS84 implementation manual'K,* prepared by EUROCONTROL and IfEN, Version 2.4, February 1998.

[12] M. Capderou, '*Satellites. Orbits and missions'*, Chapter 2.3 Orbital Elements pp. 51-55, 148-149, Springer, 2005

[13] J.B. Tatum, *'Physics topics. Celestial Mechanics'*, Chapter 3: Plane and Spherical Trigonometry, *Electronic Source*.

[14] Knott, Eugene F., Shaeffer, John F., Tuley, Michael T., *``Radar Cross Section (2nd Edition)'*, pp. 7-20, SciTech Publishing, 2004

[15] Bracewell, R., *'The Fourier Transform & Its Applications'*, McGraw-Hill electric and electronic engineering series, 3rd Edition.

[16] Hector Henech, Alessia Tomatis, Emmanuel Lance, Maria Kalama, *'Next Generation High Rate Broadband Satellites'*, Eutelsat.

[17] Dietmar Schmitt, Michael Harverson, *'Challenges in the implementation of Multi-Beam Payload Systems'*, ESA/ESTEC

[18] Giuliano Berreta, *'Ka Band Applications and Services from Dream to Reality: the KaSAT Program'*, Eutelsat Communications.

[19] Refice, A.; Bovenga, F.; Stramaglia, S.; Conte, D.; , *"Use of scaling information for stochastic atmospheric absolute phase screen retrieval*", Geoscience and Remote Sensing Symposium*, 2002. IGARSS '02. 2002 IEEE International* , vol.3, no., pp. 1729- 1731 vol.3, 24-28 June 2002

[20] Cuozzo, G.; di Bisceglie, M.; Fusco, A.; , *"The role of spatial interactions for prediction of the spectral structure of the atmospheric phase screen,"* Geoscience and Remote Sensing Symposium*, 2007. IGARSS 2007. IEEE International* , vol., no., pp.1287-1290, 23-28 July 2007

[21] Even, Markus; Schunert, Alexander; Schulz, Karsten; Soergel, Uwe; , *"Atmospheric phase screen-estimation for PSInSAR applied to TerraSAR-X high resolution spotlight-data,"* Geoscience and Remote Sensing Symposium (IGARSS), *2010 IEEE International* , vol., no., pp.2928-2931, 25-30 July 2010

[22] Iannini, L.; Monti Guarnieri, A.; , *"Atmospheric Phase Screen in Ground-Based Radar: Statistics and Compensation*," *Geoscience and Remote Sensing Letters, IEEE* , vol.PP, no.99, pp.536-540.

[23] Curlander, J.C. and McDonough, R.N., *'Synthetic Aperture Radar: Systems and Signal Processing'*, Chapter 3: *The matched filter and pulse compression*, New York, 1991.

[24] Yu Ding and David C. Munson, *'A Fast Back-Projection Algorithm for Bistatic SAR imaging'*, Science Laboratory and Department of Electrical and Computer Engineering University of Illinois.

[25] Shu Xiao, David C. Munson, Samit Basu and Yoram Bresler, *'An N2 log N Back-Projection Algorithm for SAR Image Formation'*.

[26] Cafforio, C.; Prati, C.; Rocca, F.; , *SAR data focusing using seismic migration techniques*, Aerospace and Electronic Systems, IEEE Transactions on , vol.27, no.2, pp.194-207, Mar 1991